A Numerical Study on the Unsteady Aerodynamic Characteristics of Thick Aerofoils with Wavy Leading Edges

Rafael Perez Torro, rpt1g12@soton.ac.uk

January 26, 2016

Abstract

Numerical simulations are performed over a Wavy Leading Edge (WLE) aerofoil using a NACA0021 section with a WLE wavelength of 11% and an WLE amplitude of 3% of the mean chord. The results obtained match the experimental data available in literature with better accuracy than previous publications. Nevertheless it is observed that, in contrast to what has been shown in previous literature the flow over a WLE is not periodic in every wavelength when the angle of attack is very high. Instead Laminar Separation Bubbles (LSB) appear at every second trough that eventually transition to turbulence and enables partial reattachment for a small percentage of the chord length. On the other troughs however, the flow suffers from laminar separation at the leading edge. It is also found out that the regions with the LSBs give an increased aerodynamic efficiency with respect the other trough sections of roughly 6% for the tested WLE parameters at angle of attack of 20°. Furthermore the WLE are able to debilitate the strength of the vortex shedding mechanism because of the heterogeneity that promote to the flow across the span.

Contents

List of Figures

List of Tables

Chapter 1

Introduction

1.1 Motivation

According to the Civil Aviation Authority (CAA) there were nearly three million aeroplane movements in 2012 in the United Kingdom [39]. This means nearly 8,000 flights per day in the UK. Supposing that the same amount of planes that depart from the UK destined to other countries equals the number of planes arriving UK from other countries the number of airport operations (take-off and landing) can be roughly approximated to 16,000 operations per day, only in UK airports.

Every time an aeroplane either takes off or lands leaves a turbulent wake behind. This wake is mostly composed by the trailing vortices produced by the aeroplane wings. This phenomenon is more pronounced because of the high-lift devices used during take-off/landing. Rarely the wake produced by an aircraft can produce structural damages on the aircraft encountering the wake. However it is more likely the vortices induce rolling moments which can exceed the rollcontrol authority of the encountering aircraft. Additionally the induced velocities could increase the effective angle of attack (AoA) beyond the stall angle and thus causing a failure in the operation.

Due to the high number of take-off/landing operations the air in the runways surroundings can be highly disrupted, and operations might be postponed until ambient air has settled down. In fact the United States Federal Aviation Administration (FAA) dedicates in its Aeronautical Information Manual (AIM) a whole chapter to Wake Turbulence [5, Chapter 7, section 3].

A wing's wake is manly composed by two kinds of vortices: tip vortices and trailing vortices. The air below the pressure surface has more pressure than the air flowing above the suction surface of the aerofoil. This promotes the appearance of vortical structures formed by the air trying to go from high-pressure zones to low-pressure zones. When this happens at the tip of the wings the vortices are known as tip-vortices and when it is at the trailing edge are called trailing vortices.

The strength of this vortices increases when the AoA of the device is increased because the pressure differences are also increased. At very high angles of attack the trailing vortices are also consequence of the velocity gradients present at the trailing edge. The flow coming from the suction surface at this high AoA conditions tends to be separated near the trailing edge which provokes a velocity deficit. Then when the flow coming from the pressure surface joins the flow coming form the suction surface a shear layer is created which produces the vortex shedding.

On top of this, wings do usually operate in a Re number within the turbulent regime, and hence their boundary layer eventually transitions to a turbulent boundary layer. The wake left by this kind of boundary layer is very rich in smaller coherent structures arising from turbulence which add up to the already mentioned bigger structures, i.e. tip and trailing vortices.

When more than one element is taken into account, i.e. tandem configurations, or rotor blades, the interaction between the first element wake and the second element can completely alter the whole system efficiency. For example, in multi-element wings or blades, where one element is followed by a second one or more, the second element can be very beneficial to the first element performance, and even increase the efficiency of the whole system albeit deteriorating the second element's actual performance. However this is just the case for some configurations where a certain relative position between the element has been found to be beneficial. For many other cases the interaction between elements might be detrimental.

Additionally because the main objective of multi-element arrangements is to maintain the lift at high angles of attack to produce higher C_{Lmax} the conditions where these arrangements tend to be used favour the appearance of tip and trailing vortices. So it seems clear that the wake of a multi-element wing is more likely to have vortical structures than that of a single element. And because most of the applications of multi-element wing arrangements are related with wake interaction, e.g. high-lift devices used during take-of and landing or rotor blades, there exist the necessity of finding a solution that can be reliable even when non-clean upstream conditions are faced.

Fortunately, turns out that in the last decade researchers have found that the aerodynamic characteristics of sinusoidal leading edge wings have some properties that may overcome the problem above posed. These investigations have in great manner been inspired by the shape of the flippers of the Humpback whale. This whale is able to perform very agile movements despite its size, typically between 12 and 14 meters long. Its manoeuvrability is usually attributed to the protuberances that can be found in the leading edge whale's flippers [8]. Researches agree that the introduction of sinusoidal leading edges tend to increase the lift produced at post-stall angles of attack compared to a straight leading edge aerofoil. Additionally there are also studied that prove that the Wavy Leading Edges (WLEs) also are very useful in reducing the sound produced by an aerofoil that is facing a turbulent gust [32]. Because sound production is directly related to pressure fluctuations on the aerofoil surface it is also presumable that WLEs may also reduce the lift fluctuations and hence result in a more stable device behaviour when trailing a turbulent wake.

Despite the WLEs have been studied in several experiments, both numerical ([7, 32, 41, 54, 56, 57]) and experimental ([4, 11, 18, 34, 35, 38]), the number of studies performed by high accurate computational methods is not so large. Therefore the nature of the beneficial aerodynamic characteristics of such leading edge modifications it is still unclear. Debate arises between researchers who claim that the leading edge protuberances act as a sort of vortex generators increasing the momentum exchange in the boundary layer, and those who claim that the protuberances can be considered as small delta wings that increase the lift in post stall regime by creating vortices that carry low pressure to the suction surface. Additionally there exists the believe that the WLEs may act as spanwise flow fences which when applied to finite wings, block the separation that arises at the tip of the wings.

In addition the author could not find any references in the literature to WLEs applied to double element arrangements. The characteristics of single element WLEs aerofoils seem to be ideal for their use in the after element of a tandem pair of aerofoils. Its capacity to maintain lift at high angles of attack will be showed in the literature review. On top of that some studies have shown the resistance of WLEs to highly turbulent gusts [32]. Thus, in this study the influence of a WLEs in the second element of a tandem arrangement will be study as well as the possible applications that would benefit of such arrangement if results show promising.

In the sections that follows the objectives of this project are outlined and a brief description of the chapters is presented.

1.2 Objectives

The main objectives have been already mentioned in the motivations that drive this project. Nonetheless a list of all major and minor objectives that are aimed to be accomplished in this project is shown here. These are:

1. To investigate the effect of upstream trailing vortices on a tandem configuration with WLEs on the second element.
2. To explain where the aerodynamic benefits of WLEs come from and shed some light on the controversy between the "vortex generator effect" and the "delta wing effect".
3. To investigate different combinations of WLEs parameters for different aerofoils' relative positions.
4. To be able to adapt a prior High-Order accuracy single element "in-house" CFD Fortran code to a tandem aerofoil arrangement.

1.3 Outline

A little bit of orientation work is done here for the ease of the reader. A literature review of past related works is done in Chapter 2. This includes journal papers about numerical and experimental studies related to sinusoidal leading edges, tandem-like investigations and Optimised High-Order Compact Finite Difference development review. On Chapter 3 the numerical instruments that form the CFD method used in this study are described in detail. Chapter 4 contains verification and validation studies. On Chapter 5, results for simulations of a WLE aerofoil are investigated and compared to previous literature. Finally Chapter 6 contains conclusions, remarks, and future work to be done.

Chapter 2

Literature Review

2.1 Wavy Leading Edges Review

Improving the stall characteristics in aerofoils has been a major field of study in the past. Both active and passive methods ranging from geometry modifications of trailing and leading edges, use of multi-element aerofoils, suction and blowing mechanisms, Gurney Flaps, etc. have been used. More recently a very peculiar whale, with very peculiar flippers has drawn attention of many researchers. This whale is known as the Humpback whale, very popular between Australian and American *"whale-watchers"*.

Fish and Battle [8] performed a very detailed study of the Humpback whale or *Megaptera novaeangliae*, a cetacean who owns the record of having the longest flipper among all cetaceans. But the uniqueness of this whale, and the reason why is mentioned here in this report is because of the peculiar presence of large protuberances or tubercles located at the leading edge of its flippers. It is well known by marine biologists that the Humpback whale has also a unique feeding behaviour which demands high manoeuvrability from the animal. The animal is capable, despite its big dimensions (the whale studied by Fish and Battle [8] was 9 meters long), to perform high velocity and sharp U-turns. For these manoeuvres the whale orientates its flippers at high angles of attack (AoA) while still maintaining the lift. For their study, a whale's left flipper was dissected. The cross sections of the flipper clearly resembled typical aerodynamic shapes. In particular Fish and Battle [8] stated that the Humpback whale studied had cross sections which were much alike to a NACA $63_4 - 021$ aerofoil. They found eleven tubercles along the entire flipper span. The distance between tubercles, i.e. *intertubercle distance*, found by the authors varied from the whale's shoulder to the tip following a stair shaped curve with linear intervals in between steps. The authors postulate that the tubercles of the Humpback whale act as a passive control device which improves the hydrodynamic capabilities of its flippers. They compare the tubercles with aircraft strakes, which are a type of vortex generators used to control the flow around aircraft and specially to modify the stall characteristics of their wings. Fish and Battle propose then that the tubercles generate streamwise vortices that exchange momentum within the boundary layer and thus re-energising it and finally delaying stall. It is mentioned that, as strakes, the tubercles may not increase the maximum lift of the flippers, but they help to maintain a certain level of lift while the whale is turning at high AoA. Their conclusions on this behalf are supported by some flow visualisation experiments conducted with a aerofoil model with similar leading edge geometry to those of the Humpback's flippers. On those experiments a vorticity production was showed, however the effect of these vortices being the reason for sustaining lift was unclear. Additionally Fish and Battle postulated that the tubercles create channels of high speed flow (compared to other span locations on the flipper). They base this hypothesis on the fact that no barnacles were found between tubercles. Barnacles are usually found on the upper leading edge of the whale's tubercles. However this barnacles are known to fail in attaching to the surface if higher velocities are achieved. Thus the lack of them in between tubercles supports the aforementioned hypothesis.

The study of Fish and Battle [8] sparked the curiosity of investigators who saw in the Humpback whale tubercles a very good passive control method to increase the lift at high AoA. Applications of this leading edge tubercles are suitable for any aerodynamic device that operates at high AoA or at near stall conditions such as high lift devices, turbine blades, etc.

2.1.1 Experimental Studies of Wavy Leading Edges

Fish, in collaboration with Miklosovic, Murray and Howle [34] performed wind tunnel studies at the United States Naval Academy under incompressible flow conditions (maximum Mach number was $M = 0.2$) over a NACA 0020 based finite span models of Humpback whale's flippers to investigate the effect of the leading edge protuberances on the aerodynamic behaviour of the flippers. Two models were constructed, one with tubercles and the other without, and measurements of lift and drag along with other parameters were taken. Because the size and shape of these tubercles change from one specimen to another, the authors decided to use a general model that could describe the flow features of the tubercles. Thus, for the scalloped model the tubercles followed a sinusoidal profile. Matching the descriptions of [8] the intertubercle distance and amplitude was reduced towards the tip of the model. The model, imitating the real flipper, had a semi-elliptical platform shape with a maximum chord of 16.19 cm and a span of 56.52 cm. The fact that the chord length varies along the span can be seen as a variation on the Reynolds number Re along the span. The (uncorrected) Reynolds number based on the free stream flow, the mean chord and the kinematic viscosity of the air used for the experiments ranged from 5.05×10^5 to 5.20×10^5 which is half of what expected for a typical Humpback whale manoeuvre. Nevertheless the authors tested the effect of the Reynolds number and proved that fro $Re > 4 \times 10^5$ the lift coefficient is insensitive to Re variations at moderate incidence angles.

The models were tested through a range of AoA from $\alpha = -2^\circ$ up to $\alpha = 20^\circ$ with increments of $\Delta\alpha = 0.5^\circ$ for which the three force components and the three momentum components were measured by a six-component force balance although only drag and lift were reported. The C_L of the smooth model shows a typical behaviour with a linear region and then a sudden drop at the stall angle $\alpha_{max} \approx 12^\circ$. In contrast in the scalloped model the stall happened at $\alpha_{max} \approx 16.3°$ (an increase of around 35%). But not only the stall angle is increased, Miklosovic et al. [34] found that the maximum value for the lift coefficient C_{Lmax} was also increased for the scalloped model from a value of 0.88 to 0.93 (nearly a 6% increase). At the same time the drag coefficient showed to be very similar for angles smaller than the smooth model stall angle. For angles beyond the smooth model stall angle the scalloped wing produces less drag in a very consistent way compared to the smooth one. This combination obviously results in a higher aerodynamic efficiency of the scalloped wing at most AoA. Similarly to what was stated by Fish [8], the authors postulate that the tubercles act as vortex generators that cause a momentum exchange that favours the attachment of the boundary layer to the lifting surface and ultimately increasing its stall angle. However this are only postulations and no prove that the tubercles act as vortex generators was given, i.e. only force measurements were performed. Without any flow visualisation or local velocity measurements an explanation to the effect of such interesting vortices was left unaddressed.

Johari et al. [18] also tried to investigate the effects of the leading edge protuberances typical of the humpback whale flipper by performing water tunnel experiments at the Naval Undersea Warfare Center in Newport. However the work of Johari et al. was limited to infinite wings where three-dimensional effects coming from tip vortices were avoided. The study was carried over a $63_4 - 021$ two-dimensional aerofoil for which lift, drag and pitching moments were measured at different AoA ($-6° \leq \alpha \leq 30°$) in a flow of $Re = 1.83 \times 10^5$. In the experiment different amplitudes and wavelengths for the protuberances where tested ranging from 2.5% to 12% and from 25% to 50% of the mean chord respectively. Flow visualisation was accomplished by means of tufts for the examination of the separation characteristics of the aerofoils. It was found that the protuberances modified the aerodynamic behaviour of the models beyond the already observed drag reduction past the baseline stall angle. The protuberances followed as in [34] a sinusoidal profile so the platform area of both the smooth and the undulated wings was equivalent.

In the paper the authors separate the effects of the Wavy Leading Edges (WLEs) amplitude from the wavelength effects. For the smallest wavelength tested the modified aerofoils' lift curve followed a linear trend along with the baseline (smooth) up to 8°. From there onwards the baseline's lift curve slightly decayed and finally stalls at an AoA of $\alpha \approx 21°$ with a maximum C_l of 1.13 at the stall angle. After stall the baseline dropped to a C_l of 0.57 for $22 < \alpha < 28$. As for the modified (WLEs) models it was find out that for this wavelength (0.25c where c is the mean chord) the model with smallest amplitude (0.025c) followed the baseline up to $\alpha = 17°$ where sudden stall happened. However the lift drop was significantly smaller ($C_l \approx 0.94$) to that of the baseline and after stall the modified model's lift curve slowly decayed until at $\alpha \approx 30°$ where the value was reduced to that of the baseline. The foil with medium amplitude (0.05c) followed a similar trend although the drop of C_l due to stall happens earlier at $\alpha \approx 14°$ then as with the small amplitude model, the lift softly decayed always remaining on top of the baseline lift curve for AoA greater than the baseline stall angle. The aerofoil with the biggest amplitude (0.12c) had its maximum C_l at $\alpha \approx 10°$, way before the baseline stall angle, with a value of $C_{lmax} \approx 0.85$. Despite reaching its maximum C_l before than the other models, there was no appreciable drop after this point and the lift curve followed a flat profile up to the maximum tested AoA. Although the C_{lmax} of the model of 0.12c amplitude is 28% less than the baseline, it remained 40% greater than the baseline post-stall C_l. Regarding the drag coefficient of the tested models, it seemed that bigger amplitudes tended to increase the drag although after the baseline stall all the curves collapsed. It is worth mentioning that the smallest and the medium amplitude foils remained very close to the baseline drag curve up to their respective stall angles where due to flow separation the drag suffered a sudden increase. This trends were also seen for the models with higher wavelength (0.5c). An interesting point was raised by the authors who compared the C_l slope values of the models and find out that in general the $dC_l/d\alpha$ decreases with the WLEs amplitude for both wavelengths. The direct consequence of the just mentioned lift and drag behaviours was that the aerodynamic efficiency(L/D) produced by the WLEs aerofoils was up to 50% greater than the baseline model in the post-stall regime. Comparisons between aerofoils with the same WLEs wavelength showed that there was very little differences in terms of aerodynamic coefficients. The effect of the wavelength can only be appreciated at the small and medium amplitudes where smaller wavelengths seem to have a slightly positive effect in the sense that in general allowed the aerofoils to reach higher C_{lmax} at higher as well stall angles. Regarding the drag coefficient, the wavelength also showed minor variations between different modified models although it seemed that shorter wavelengths had slightly smaller drag coefficients for all AoA. A helpful plot showing the 0.12c amplitude 0.25c wavelenght model's coefficients normalised by the baseline model values shows that in the pre-stall regime the baseline model was superior to the WLE model with up to 70% less drag and 20% more lift. However as soon as the baseline model stalls the modified model took over and achieved up to 50% increase in lift with almost no drag penalty.

In order to assess what are the flow features that make the WLEs aerofoils have different aerodynamic characteristics Johari et al. [18] performed flow visualisations of the flow using tufts located at the suction side of the models. In the paper photographs of the baseline (BL), the large wavelength for medium and large amplitudes (4M and 4L) and the small wavelength and medium amplitude (8M) models are shown at $\alpha = 12°, 18°$ and 24°. These AoA were selected since they represent the locations at which the large amplitude model separates from the baseline lift curve and the moments just before and after the baseline stalled respectively. At $\alpha = 12°$ the flow over the baseline was fully attached whereas for the other modified models signs of flow separation coming from the *"troughs"* in between *"peaks"* where the flow remained attached started showing. At $\alpha = 18°$ the baseline model already showed a separated region covering the second half of its chord length. At the same time the models with the largest wavelength showed separation over 3/4 of their chord length. However the model 8M with the smaller wavelength had a larger region of attached flow compared to the other two modified models although still smaller to that of the baseline. After baseline's stall, the flow over the baseline was obviously fully separated whilst on the modified models although the flow could be considered separated over most of the aerofoils surface, it remained attached at the peaks being the model with the larger amplitude (4L) the one with the largest attached region. From this, the authors concluded that the modified models are capable of maintaining the lift after stall due to the strips of attached flow over the peak sections. However in the pre-stall regime the protuberances turned out to be detrimental since the flow separation originated in the troughs caused earlier separation compared to the baseline flow.

Afraid of that the variation on the leading edge curvature radius was the reason of flow separation on the trough sections, Johari et al. tested a different model similar to the 8M where the curvature radius at the troughs remained equal to the baseline. Nevertheless the results showed that this had no major effect since very similar results were obtained and hence they concluded that the reason for the special flow features of the WLEs aerofoils are due to mainly the inclusion of the alternance between peaks and troughs and not due to the leading edge geometry. Quantitative details as well as flowfield mechanisms for the observed patterns were left unaddressed until future work.

Just three years after the here first mentioned paper, Miklosovic [35] published the results of a set of wind tunnel experiments the purpose of which was to determine whether the performance improvements found previously in WLEs semi-spanned wings resulted from enhancements to the sectional characteristics of wings with tubercles or, on the contrary were due to Reynolds number effects due to a tapered platform, or to other 3-D effects such as spanwise stall progression. In order to separate both effects, Miklosovic conducted experiments over a full-span (infinite) wing based on a NACA 0020 aerofoil at the US Naval Academy at $Re = 2.74 \times 10^5$ and 2.77×10^5 and free stream Mach number $M_\infty = 0.13$. Additional measurements similar to those in [34] are shown for the semispan model. The infinite wing results are in accordance to Johari et al. [18] in the sense that the undulated wings although showing a premature stall with lesser C_{lmax} they had a softer stall pattern that made them to be more effective past the clean (smooth) leading edge model's stall angle. On the other hand, while the baseline full-span model had a lift drop of 13% at $\alpha \approx 12°$, the finite scalloped-span model remain under positive $dC_l/d\alpha$ beyond that point and up to $\alpha \approx 17°$ increasing the C_{lmax} 4%. Moreover after stall the scalloped finite wing lift curve remained always over the baseline, and in terms of drag, the scallops only caused a drag increment for C_l values between 0.70 and 0.83. The flow surrounding a WLE aerofoil is by nature 3-Dimensional since the surface gradients provoke pressure gradients that induce vortical structures similarly to what happens in a "delta" wing due to the sweep angle. The authors nevertheless stated that this vortical flow is not comparable to that of vortex generators in the sense that vortex generators tend to both increase C_{lmax} and C_{dmin}, fact that does not happen at least in the infinite wing. On the other hand, the finite wing benefited from the addition of leading edge tubercles and enabled higher C_{lmax} and α_{stall} in comparison with the clean wing. Miklosovic postulated that the combination of tapered platform shape and wavy shape confines the separation to the wing tips, stopping it from causing stall at spanwise locations near to the wing root.

An other paper that reinforces the fact that the WLEs might act as spanwise flow fences is that of Ozen and Rockwell [38] who conducted Particle Image Velocimetry (PIV) over finite plate-wings with and without sinusoidal leading edges, both attached to a body of revolution on one of the wing tips. In contrast to all the previously mentioned studies, Ozen and Rockwell studied the effect of the WLEs on a wing undergoing a flapping motion. The experiments took place in a free-surface water channel at $Re = 1300$ which yielded to coherent streamwise vortices. The wavy models were tested with an amplitude of 0.098c and a wavelength of 0.246c where c represents the chord. The flapping motion is defined around the dihedral angle with a periodic sawtooth function that oscillates between 30° and −30°. The vorticity pictures located just after the leading edge of the models showed a very thin layer of negative vorticity for the baseline whereas for the WLE plate an ordered pattern of streamwise vorticity was shown. A little further in the downstream direction, at half the chord length, the baseline showed a well defined tip vortex as well as big (comparable to the tip vortex size) vorticity zones of both signs. The undulated model, although it still had the tip vortex, did not show evident signs of large-scale vortices in contrast to the straight leading edge plate. This was corroborated by the study of the normalised spanwise velocity which showed very little spanwise movements for the undulated model in comparison to the baseline, a side from the tip vortex present in both cases. The streamlines at this plane also showed evidence of highly three-dimensional flow on the baseline and just mild distortions for the sinusoidal leading edge plate.

From the above reviewed papers one might think that the predominant parameters of a WLE wing are the amplitude and the wavelength of the tubercles, however the following reviewed papers of Hansen et al. [11] and Guerreiro and Sousa [4] suggest the existence of at least two more.

Hansen et al. [11] conducted Hydrogen-Bubble visualisation and force measurements in a closed-return water tunnel and an open-return wind tunnel respectively at the University of Adelaide. Water tunnel flow visualisations at Reynolds numbers of $Re = 4370$ and 5250 over a NACA 0021 are shown in this paper. Streaklines from these experiments showed how streamwise vortices are created in the troughs between tubercles. These vortices add a spanwise component to the flow which makes the undulated aerofoils to have a highly three-dimensional flow in contrast to the straight leading edge baseline model. The images showed how decreasing the intertubercle separation, i.e. decreasing its wavelength, enhanced the interaction between vortices leading to an apparent increase in turbulence which at the same time may lead to a higher momentum exchange. Hansen [11] also discovered that models with the same tubercle sweep angle, this is with the same amplitude to wavelength ratio (A/λ), had similar vortical structures. The authors postulated that the wavelength may have a big impact on the momentum exchange in the boundary layer whereas the tubercle sweep angle may have more influence on the strength of the trough's vortices.

As aforementioned, force measurements where taken in a wind tunnel; however the Reynolds number of the experiment was $Re = 1.2 \times 10^5$. In the study, two different aerofoils were studied so the effect of the WLEs on different aerofoil geometries could be compared. The aerofoils selected for the study where: the NACA 0021 (the same used in the flow visualisation), and the NACA 65-021. The experiments were in great agreement with previous studies [18], however the results showed that the tubercles were more effective in the pre-stall regime for the NACA 65-021 than for the NACA 0021. It was suggested [11] that the improved performance on the NACA 65-021 over the NACA 0021 is due to the fact that the first mentioned aerofoil already has a softer stall and lower C_{lmax} compared to the second one. For the NACA 65-021 the position of maximum thickness is beyond the extent of the laminar boundary layer, and hence it has a greater region where the aerofoil can benefit from the momentum exchange that the WLEs add to the aerofoil's characteristics. As regards of the post-stall behaviour, both aerofoils showed improved characteristics when the sinusoidal leading edges were used. The authors similarly to what was previously done by Johari et al. [18] separated the effect of the tubercles amplitude from the wavelength when commenting their results. In terms of tubercle amplitude, larger tubercles lead to smoother stall with the penalty of reducing both the C_{lmax} and α_{stall}. On the other hand smaller tubercles achieved higher C_{lmax} values in comparison to larger tubercles while still having improved post-stall performance than the baseline model. However, no matter the amplitude of the tubercles, the modified models had always a stall angle smaller than the baseline ($\alpha_{stall}^{WLE} < \alpha_{stall}^{baseline}$) and consequently an associated drag increase on drag compared to the baseline. Nonetheless after the baseline stall angle the undulated aerofoils showed very similar if not less drag production.

Regarding the tubercles wavelength, Hansen et al. [11] stated that despite initial experiments showed that a reduction in the wavelength could be beneficial, later test pointed out that for a given amplitude, there exist a limit beyond further reductions in the intertubercle distance are no longer beneficial. Nonetheless, models with small wavelength not exceeding the mentioned limit exhibited improvements in C_{lmax} , α_{stall}, and drag, in comparison to longer wavelength models. This affirmations contrast with Johari [18] who concluded that the wavelength had a minimum impact.

But the most interesting outcome in the writer's opinion was that in the pre-stall regime, undulated aerofoils with the same A/λ, or tubercle sweep angle, had very much alike aerodynamic patterns; and for a given A/λ ratio the models with smaller wavelength (and amplitude) achieved the largest C_{lmax} , α_{stall} and lowest drag. All in all the authors recognise that although it is clear that the leading edge protuberances give rise to the formation of streamwise vortices, the reasons behind the flow alteration produced by the tubercles is not yet completely understood. They stated that it is unclear whether the streamwise vortices have a similar effect to the edge vortices existing in delta wings which increase the lifting capabilities of such wings, or on the contrary, they act as vortex generators increasing the momentum exchange in the boundary layer and ultimately delaying stall. Even so they claimed that the tubercles act in a very similar manner to vortex generators based on some calculations comparing the effective height of the tubercles with the effective device height of vortex generators. Those calculations yielded to similar results when comparing both effective shapes with a potential flow calculation of the boundary layer thickness. Moreover Hansen et al. [11] claimed that there exists several analogies between the WLEs and vortex generators. In first place both create a pair of counter-rotating vortices. Secondly, the device sweep angle (A/λ in WLEs) and device separation (wavelength in WLEs) play a major role on the device effectiveness. And last but non least, the tubercles seemed to be more effective in the post-stall regime, which means that they are more effective at high AoA (and hence higher values of effective height) as it happens with vortex generators.

In last place, the experiments conducted in the open-circuit wind tunnel of the Department of Mechanical Engineering at Instituto Superior Técnico by Guerreiro and Sousa [4] are reviewed. The researchers proved that a side from the parameters discussed above, the wing aspect ratio plays a big role on the flow characteristics and enhancement capabilities of WLEs wings. The experiments were done over a finite-wing with a section based on the NASA LS(1)-0417 aerofoil which presents a “predictable, docile stall behaviour” in authors words. Two sets of wings with aspect ratio of $AR = 1$ and $AR = 1.5$ were tested at two different flow conditions: $Re = 1.4 \times 10^5$ and $Re = 7 \times 10^4$. For the highest Reynolds number and $AR = 1$ under investigation the baseline model (without sinusoidal leading edges) did not stall for any of the tested AoA, consequently the undulated wings, which in past experiments showed their most at post-stall regime, did not exhibit notable differences, neither improvements or detriments. For $AR = 1.5$ the undulated models did stand out, in particular after the baseline stall angle. For this aspect ratio the baseline did stall with an abrupt drop in C_l at $\alpha = 17°$. The scalloped wings although they all stall before the baseline, as reported in many other papers mentioned before, they did it in a much smoother way. For both AR diverse combinations of tubercles' amplitude and wavelength showed the best performance on combinations of large amplitude and large wavelength which showed gains of 45% over the baseline with only 25% maximum loss. This contrasts with what reported in the experiments of Hansen [11].

For the low Reynolds number experiment ($Re = 7 \times 10^4$) both sets of wings were superior to the straight leading edge models. For $AR = 1$ there were no appreciable signs of traditional stall patterns in any of the models tested and the undulated wings had greater lift coefficient over the whole range of AoA tested, in special at low AoA. For $AR = 1.5$ it was again observed a more typical stall behaviour from the baseline model however, the sinusoidal models did not experience a remarkable reduction in either the C_{lmax} or the α_{stall} while still being much superior to the baseline in post-stall regime. In light of these results Guerreiro and Sousa [4] claimed that as well as the protuberances amplitude and wavelength, the aspect ratio of a 3-D wing plays a huge role in the effectiveness on the sinusoidal leading edge aerofoil lift performance. Furthermore, comparison of different runs at different Reynolds number but with the same model geometry showed that the sinusoidal leading edge lifting surfaces are less prone to performance deterioration due to Reynolds number effects.

More recently, Zhang et al. [59] conducted an experimental study using a closed circuit wind tunnel on WLE aerofoils based on the NACA $63_4 - 021$ at $Re = 2 \times 10^5$. The turbulence intensity at the test section was 0.2%, and the models had a chord and span of $c = 100mm$ and $s = 350mm$. The modified aerofoil studied was based on a sinusoidal leading edge with amplitude of $A = 0.12c$ and wavelength of $\lambda_{LE} = 0.25c$, the same as model 8L in Johari et al. [18]. The aerofoils were tested in a range of angles of attach between $\alpha = 0°$ and $\alpha = 90°$ were they both performed force measurements of lift, drag and momentum coefficients, as well as Particle Image Velocimetry (PIV) and surface-oil-flow visualisation too, since vorticity was only available for ω_x and ω_z.

Force measurements were almost identical to those of Johari et al. [18], and hence extensive analysis of those is not interesting here. Basically, they reinforce the idea that WLE improve the aerofoil's performance after stall of the baseline at the expense of worsening it before that point. Again, stall pattern is shown to be much softer for the modified aerofoil. At $\alpha = 18°$ PIV of ω_z as well as velocity profiles along the chord show that separation occurs earlier on both peak and trough sections compared to the baseline model, being the trough section the one with the separation point closest to the leading edge. Contours of streamwise vorticity ω_x show pairs of counter-rotating vortices created by the spanwise flow that tends to converge the streaklines to the troughs as it is shown by the oil-flow visualisation. In order to assess the flowfield in the characteristic region were lift remains constant after stall, the researchers investigated the spanwise vorticity contours for angles of attach of $\alpha = 12°$ and $\alpha = 23°$. By integration they obtained the circulation corresponding both peak and troughs and it turned out that circulation values remain also nearly constant with the variation of α. Nevertheless the circulation at the troughs was higher, almost double, that at the peaks, despite having a lesser portion of attached flow.

In combination with numerical experiments, Rostamzadeh et al. [44] performed surface pressure measurements over wavy aerofoils using the low-speed KC Wind Tunnel at the University of Adelaide at $Re = 1.2 \times 10^5$. Here just the experimental part is shown, and the analysis of their numerical study can be found in the next section The researchers added pressure taps at different sections of the WLE aerofoil as well as the baseline aerofoil, both based on a NACA 0021 aerofoil section. On the modified aerofoil the pressure measurements were performed on the peak, trough and middle sections. Pressure measurements show that the addition of the sinusoidal leading edge clearly alters the pressure distributions along the span. The trough sections have generally lower pressure, and only the baseline geometry produces more negative pressure before the baseline's stall point. After this, also the middle section shows more negative pressure over the suction side at $\alpha = 15°$, which is very close to the WLE model's stall point. Otherwise the trough section is the one that contributes the most to lift.

2.1.2 Numerical Studies of Wavy Leading Edges

In 2008, Pedro and Kobayashi [41], numerically replicated the experiments done by Miklosovic et al. [34]. The Reynolds number of the study was $Re = 5 \times 10^5$ and the simulations were carried out using the commercial software Fluent using a parallelised finite volume technique. Turbulence modelling was tackled using Detached Eddy Simulations (DES), a technique that uses Large Eddy Simulation (LES) outside the boundary layer and Reynolds Averaged Navier-Stokes (RANS) modelling inside the boundary layer using the Spalart-Allmaras turbulence model. The numerical method used was an implicit 2^{nd} Order accurate in both space and time. To simulate the flow in proximity of the surface wall the first cell laid between 30 and 100 wall units. In total the grids used 2.6 million elements. The simulation was ran for 5 mean flow residence time units with a time step of 0.0001sec. Values of lift and drag coefficient showed great agreement with the corresponding wind tunnel values measured by Miklosovic [34]. Comparisons of several flow field quantities were done for a AoA $\alpha = 15°$ where the biggest differences between the scalloped model and the baseline were found. Vorticity isosurfaces showed large streamwise vortices aligned with the tubercles. The researchers stated that these vortices act in a similar manner to vortex generators, i.e. re-energise the boundary layer by carrying high momentum close to the wall. To prove this isosurfaces of velocity magnitude squared (which is proportional to the fluid momentum) were plotted and it was observed that high momentum regions covered wider locations on the scalloped wing in comparison to the straight leading edge wing. After investigation of vortical structures, the authors investigated how separation happened in both wing geometries by means of surface streak lines of Wall-Shear Stress (WSS). Nonetheless, because of the spanwise chord variations consequence of the platform wing shape, two regions of moderate Reynolds number close to the wing root, and low Reynolds number region close to the wing tip, were considered separately. At a AoA of 12° both models showed similar flow patterns with trailing edge separation at the moderate Re zone and leading edge separation closer to the wing tip. Increasing the AoA from 12° to 18° caused the wing tip separation to progress towards the root in the baseline model. On the other hand the scalloped model did not suffer such degradation, and the flow patterns remained much similar to those given at $\alpha = 12°$. Pedro and Kobayashi [41] hence concluded that the WLEs prevent the separation to propagate from the tip to the root creating barriers associated with the large spanwise vortices. They compared this behaviour with wing fence devices which minimise three-dimensional flow features by adding physical barriers to the flow that travels perpendicular to the mean flow.

In relation to Pedro and Kobayashi [41] Yoon et al. [57] also investigated by means of Computational Fluid Dynamics the effect of sinusoidal protuberances on three-dimensional finite wings; however they performed a numerical study on rectangular finite wings instead. Those rectangular wings had sinusoidal leading edges covering different portions of the wing's span at a Reynolds number of $Re = 10^6$ which was double of that used in [41]. The models used were of constant tubercles wavelength and amplitude and the only difference between models was the percentage of the span covered by the undulations (waviness ratio they called). The baseline model, without any leading edge modifications, had a section based on the NACA 0020 aerofoil. A side from the baseline, five models with waviness ratios ranging from 0.2 to 1.0 were investigated. The numerical method involved solving the steady RANS equations with at $k - \omega$ SST turbulence model. The spacial order of accuracy of the computations was not mentioned though. The first cell of the grid near the wall surface laid under one wall unit and the total number of cells used was 2.3 million. Force coefficient reported that the baseline followed a linear progression in lift up to its stall angle of 20° where it produced the highest lift value. Models with undulated leading edges perform differently to the baseline, with the exception of the model with 0.2 waviness ratio, which was almost identical to the baseline. The other models with undulations stalled earlier than the baseline at $\alpha = 16°$ but, equally to what reported by the experiments of Miklosovic [34, 35], Johari [18] and Hansen [11], their stall characteristics were much more stabler than the straight leading edge model. Furthermore in the post-stall regime undulated models showed improved lift capabilities being the model with WLE covering the entire span the best of them with improvements of 10–15% in lift coefficient.

Surface pressure contours were analysed for three different AoA of 16,20 and 32°. Those angles represented the stall angle of the wavy models, the stall angle of the baseline model and a post-stall regime angle respectively. At $\alpha = 16°$ the baseline showed a two-dimensional distribution away from the wing tip vortex typical of attached flow conditions. This was even present in the models with modifications in the leading edge with the exception of the model with waviness ratio of 0.6 which showed a disrupted distribution. Having this model different distribution was not a surprise since it was the first to stall even earlier than the other modified models at $\alpha < 16°$. The other wavy models although having a similar pressure distribution to the baseline in the last three quarters of their chord length, presented a patterned distribution in the leading edge area. At this chord location, the troughs between tubercles were associated with low pressure zones while the peaks were associated with higher pressures. As the AoA is increased up to 20° the flow in the inboard of the baseline begun to deviate from its two-dimensional pattern with pressure gradients in the spanwise direction in the second half of its chord. The same could be said about the models with waviness ratios of 0.2 and 0.4. However as the waviness ratio grew from 0.6 to 1.0 a new zone of started to develop at the first quarter of the span just after the wing tip vortex influence zone finished. At that region large pressure coefficient gradients in the span direction were limited to the leading edge where the sinusoidal shape makes them unavoidable, but form then onwards are almost non-existent. Further increase in the AoA ($\alpha = 32\,\mathrm{deg}$) finished with any sign of flow coherence for the baseline model where the flow was supposed to be fully detached. Similarly the scalloped models also lack of flow coherence although there appeared low pressure zones just after the protuberances with increasing waviness ratio.

Surface streaklines of WSS confirmed what stated in the last paragraph. Reversed and highly three-dimensional flow was seen where pressure gradients were observed for AoA 20 and 32°. Particularly at the highest AoA the flow seemed to be fully detached from the leading edge to the trailing edge. Despite this fact the models including waviness ratios higher than 0.2 still had proven to produce much more lift at this conditions. The authors, following previous researchers' hypothesis, postulated that the lift enhancement was due to the WLEs acting as vortex generators that promote the mixing in the boundary layer increasing its momentum and prolonging the attachment zone. This affirmation does not agree with the WSS visualisations seen in the paper. The authors also included isosurfaces of spanwise vorticity at the same angles of attack. The images showed how vorticity is channelled in between protuberances and tend to merge or collapse to the zones were lower pressures were reported. It seems unclear whether the vortical structures were attracted to a previous existent low pressure zone or the accumulation of vortices creates the low pressure zone by it self. What it is clear is that low pressure zones positive correlate with zones where the vortices appear, which makes the WLEs effect to be more alike to the *"delta wing effect"* than to vortex generators' effect.

The work of Weber et al. [54] relates to [41, 57] since it was a numerical study carried out on wings with the same geometry of [41] but using a Reynolds Averaged approach as in [57]. In contrast to the last two, the simulations were not produced using the commercial software Fluent. The programs used in this occasion were STAR-CCM+ and SolidWorks Flow simulation (SFS). The spatial order of accuracy of the computations was not mentioned but the time step used for the unsteady calculations performed was $\Delta t = 2.59 \times 10^{-}5$. The models tested in this numerical experiment replicate those of Miklosovic et al. [34], so the wings tested where highly tapered with a semi-elliptical platform shape in contrast with [57], who used rectangular platforms. To validate and verify their results Weber et al. [54] performed several grid dependence studies on both codes until they reached their maximum computational power without still being grid converged. Nevertheless they also did a turbulence model dependence study that showed that the Spalart-Allmaras model using STAR-CCM+ was superior at low angles of attack

($\alpha < 6°$) with very good agreement with the experimental results of Miklosovic et al. [35]. At a moderate angle of attack lesser than the stall angle, again STAR-CCM+ showed to be superior to SFS, this time shifting to the $k - \omega$ turbulence model. Also at this stage unsteady calculations were used. In the post-stall regime the SFS with $k - \epsilon$ turbulence model was the code giving the best agreement with experiments although neither the programs with any turbulence model combination managed to capture correctly the stall angle or the lift an drag coefficients with enough accuracy. This shows that the RANS capabilities may not be enough to deal with this kind of problem with massive separation and high shear stress tensor variations from point to point. In fact, a side from the Spalart-Allmaras model for low angles of attack, all models either overpredicted or underpredicted the C_D with maximum errors of more than one order of magnitude. Despite the results of this numerical investigation are not very accurate, the flow visualisations that can be extracted from them are still useful to understand the stall mechanisms of a scalloped wing. Streamwise velocity and pressure contours (from STAR-CCM+), and streamlines and pressure distributions (from SFS) can be found in this paper.

The images show how for the non-scalloped wing, the separation begun with a trailing edge separation starting from the tip and progressing to the root and leading edge as the AoA was increased. On the other hand, although still presenting a similar pattern, the scalloped models had separation starting from the troughs between tubercles as mentioned in [11, 18, 41], and past the stall angle were able to maintain regions of apparent attached flow. The pressure contours showed in the paper are difficult to interpret because of the black and white images presented, nonetheless the authors cleverly attached point measurements at one trough and one peak tubercle locations which showed that the minimum pressure was always measured at the troughs which agrees with [57]. The authors relate the early stall in the trough regions with the upwash consequence of the pair of counter-rotating vortices that are created at each tubercle. This upwash flow increases the effective AoA at this sections which ultimately cause their early stall. In contrast the vortices generate a downwash flow on the peak sections which reduces their effective angle of attack making them more prone to flow attachment. In addition as aforementioned the lowest pressure on the troughs combined with the upwash flow resulted in severe adverse pressure gradients in these sections which are known to be highly related with fluid flow separation. This statements were confirmed by the inspection of different pressure coefficient distributions on the peak, trough and a baseline section. It was clear that the higher adverse pressure gradients were experienced by the trough regions followed by the baseline sections and lastly by the peak sections with the weakest adverse pressure gradient among them. The authors compared the tubercles with small delta wings located at the leading edge that caused the creation of streamwise vortices due to pressure differences between the suction and the pressure sides of the lifting surface.

Until now all the papers tend to promote the idea that the WLEs when applied to infinite wings deteriorate the lifting capabilities in the pre-stall regime while at the same time enhancing them in the post-stall regime. In the work of Zhang et al. [56] this is not the case. Zhang et al. conducted numerical simulation of sinusoidal leading edge aerofoils using a multigrid finite volume method for the solution of the URANS equations with the $k - \omega$ SST closure turbulence model. Although in the paper the authors studied the effect of the undulations on both static and flapping configurations, only static cases are considered in this review. After accomplishment of grid and time step dependence studies the lift measurements showed that the WLEs produced in all cases tested more lift than the baseline model. However it is worth saying that the Reynolds number of this numerical experiment was the lowest among all the simulations presented up to now with $Re = 1 \times 10^4$ which could be the reason for such different results. Guerreiro and Sousa [4] already showed that at low Re their experiments showed similar results but for a finite wing of $AR = 1$ and the wings studied here where of infinite AR. However familiar flow features were also depicted in this investigation. The minimum registered pressure values were again found in the troughs where also vortical structures were created. It was also found that the most adverse pressure gradients were those located at the troughs and the weaker ones at the peaks. Pressure contours of the models with tubercles amplitudes of 0.05c and 0.10c with respectively wavelengths of 0.25c and 0.50c showed very similar contour patterns. One might realise that this agrees with Hansen et al. [11] since the amplitude to wavelength ratio of those cases is the same $A/\lambda = 0.05/0.25 = 0.10/0.50 = 0.20$. It may be recalled that Hansen et al. [11] suggested that similar values of this ratio would lead to similar flow patterns.

The lowest Re numerical investigation reported here is not that of Zhang et al. [56] but that of Favier et al. [7] with $Re = 800$. The method they used to numerically solve the Navier-Stokes equations was DNS which is quite stringent in terms of Reynolds number. They used a Cartesian 3-D mesh with a immersed boundary method over a NACA 0020 aerofoil based section. An infinite wing with periodic boundary conditions in the span direction was used. Both convective and diffusive fluxes were approximated using a 2^{nd} order accurate central finite difference with a fractional time-step (three-steps low-storage Runge-Kutta) method for the time advancement. They used an incompressible formulation with a 2^{nd} order semi-implicit pressure corrector procedure. The final grid used by the researchers was made of 6×10^6 points, and the procedure they followed was validated against experimental data at $\alpha = 20°$, the same angle of attack they used for the whole set of simulations. This angle of attack was chosen to be in the post-stall regime of the NACA 0020 since most of the literature showed this was the range where more benefits could be obtained from the WLEs. For this flow conditions of $Re = 800$ and $\alpha = 20°$, the authors performed a parametric study on the amplitude and wavelength of the tubercles. They found out that for a given combination (A=0.07c and $\lambda = 1.0c$ namely) the vortex shedding experienced by the baseline was stopped and a quasi-steady behaviour was obtained at the expense of lower lift coefficient (lower drag was also obtained). For that given wavelength of $\lambda = 1.0c$ they found out that decreasing the amplitude also increased of both lift and drag fluctuations. Further investigation of isosurfaces of zero streamwise velocity flow showed that the tubercles highly disrupt the separation topology on the spanwise direction. While the baseline without any leading edge modifications experienced an homogeneous leading edge separation along the entire span, the undulated model with $A = 0.07c$ and $\lambda = 1.0c$ showed leading edge separation limited to the troughs. At the same time, signs of attached flow were seen at a thin strip located at the peak span section. This again agreed with other researchers [11, 18, 54, 56, 57].

Favier et al. [7] claim that the morphology of the flow over a WLE aerofoil is driven by streamwise vortices however they disagree with the general trend that associates the presence of those vortices with the pressure difference on the leading edge protuberances (sort of small delta wings). They proposed instead that the vortices are created by velocity gradients in the spanwise direction that evolve into Kelvin–Helmhotz instabilities that create vertical vorticity tubes that are almost instantaneously tilted by the bulk flow and aligned with the free stream. To prove that the authors used longitudinal velocity fluctuation profiles in the wake which showed slower flow at the peak's sections and faster flow at the troughs. They state that this additionally brings more momentum to the boundary layer which makes attachment more likely. However no mention on what makes that particular combination of amplitude and wavelength ($A = 0.07c$ and $\lambda = 1.0c$) more stable was done.

Favier also coauthored with Skillen from University of Manchester in Skillen et al. [49]. In this paper the authors replicate the experiments of Hansen [11] at $\alpha = 20°$ and $Re = 1.2 \times 10^5$. Incompressible Large Eddy Simulation was used to solve the filtered Navier-Stokes equations using a finite volume technique. The discretisation was *2nd order* accurate in space and time. The aerofoil section used was a NACA 0021, and the WLE parameters used were $h_{LE} = 0.015\bar{c}$ and $\lambda_{LE} = 0.11\bar{c}$. Force coefficient values from computations show to be 15% off with respect to Hansen [11], which authors claimed that was due to the fact that the numerical simulations were initially started from a laminar condition whereas the experimental study was performed in a wind tunnel with 0.8% turbulence intensity. Despite this fact, they proceeded to examine the results obtained.

Basically the undulations act to remove the oscillations in both force coefficients as observed in aforementioned papers. It is also shown how while at $\alpha = 20°$ the baseline is deep stall, the WLE model has portions of attached flow at the peak sections. At he trough sections a small laminar separation bubble is located near the leading edge, and then further downstream the flow finally separates. The authors suggest that the flow is deflected by the leading edge geometry towards the troughs, accelerating it, and ultimately creating suction peaks that in the end trigger more adverse pressure gradients on these sections. Skillen et al. [49] conclude that the variation of pressure in span generate the appearance of pairs of streamwise vortices that increase the momentum transfer from outside the boundary layer towards the peaks and ultimately makes them less prone to separation. This portions of attached flow, they say, are accountable for the extra lift generated by the modified aerofoils compared to the straight leading edge aerofoils. Nonetheless a sectional pressure plot presented in the paper suggests that the trough regions could produce more lift due to the more negative pressure values on the suction side, since the pressure side is identical for all the span sections.

As mentioned earlier, Rostamzadeh et al. [44] performed both numerical and experimental studies over WLE aerofoils based on the NACA 0021 section. Both numerical and experimental studies were performed at $Re = 1.2 \times 10^5$. The numerical method used was a Reynolds Averaged Navier Stokes (RANS) method, in particular the SST model was used combined with a finite volume solver (Ansys CFX 12.1). From numerical results, circulation was computed at all span locations, and shown a sinusoidal pattern similar to that of the leading edge geometry. The tubercles, they say, ripple the spanwise vortex sheets which in turn trigger the already mentioned counter-rotating streamwise vortex pairs. The authors claim that the mechanism of formation of these streamwise vortices is basically of *Prandtl's secondary flow of first kind*, where vorticity is reoriented from the spanwise direction towards the streamwise direction. Rostamzadeh et al. [44] depicted some key locations of the flow generated by the WLE geometry. First, from the shear stress lines, a point of detachment is found in the trough section, which then is followed downstream by a saddle point. In between those points a separation bubble was identified. Additionally, the flow from the peaks that escapes from the strong negative pressure gradient that attracts the flow towards the troughs, spirals into two foci near the trailing edge. Inspection of different WLE parameters, and different angles of attack, it can be seen that the shape and size of these key locations varies. For example, before the baseline's is reached, decreasing the WLE's wavelength λ_{LE}, and increasing the angle of attack α, both tend to break the separation bubble along the span, resulting in several bubbles all located at the same chord position. On top of this, increasing α also increases the size of the separation zone in the streamwise direction, as well as moving it further upstream. If α is increased enough the separation bubble and the foci region merge into a big separation zone which covers most of the chord length.

After baseline's post-stall angle, while the baseline is completely separated, the modified foils still have portions of attached flow. However these regions have complicated patterns which change depending on the WLE parameters (amplitude h_{LE} and wavelength λ_{LE}). Nevertheless, sectional lift plots show that maximum lift is always achieved at middle sections. Additionally, contour plots of streamwise vorticity on flow-perpendicular planes located downstream the aerofoils show that the relation h_{LE}/λ_{LE} is directly proportional to the strength of the streamwise vortices.

To close this section, the work of Lau et al. [32] is revisited. In contrast with the previous mentioned scientific papers, the calculations performed here are of aeroacoustic nature. No viscous effects were taken into account and hence the authors used the unsteady Euler equations which they solved using a high-order accurate numerical scheme (4^{th} order accurate in space and time). The flow around a NACA 0015 was simulated for different wavy leading edge geometries which they compared to a straight leading edge baseline. The flow was seeded with synthetic turbulence in order to evaluate the effect of the sinusoidal shapes on the aerofoil gust interaction noise. It was found out that the scalloped aerofoils reduced the sound produced by the lifting surface and more important that this reduction was strongly related with the ratio between the tubercles peak-to-peak amplitude and the gust wavelength, i.e. LEA/λ_g, with higher values of this ratio achieving the strongest noise reductions. However this reduction where found to saturate at a certain value of LEA/λ_g beyond which no more significant reductions were reported. On the other hand the wavelength of the protuberances showed minimum effect on noise reduction. The researchers discovered that the reduction was caused by a shifted phase response at different spanwise sections while for the baseline the pressure oscillations where in phase independently of the spanwise location of the measurement. This suggests that the WLEs, a side from making the flow more resistant to lifting force deterioration in the post-stall regime as mentioned in the rest of the papers, can also offer more robust performance against upstream flow disturbances. The sound production of an aerofoil due to gust interaction is associated with pressure force oscillations and hence if the noise of this interaction is reduced it means that the force fluctuations are softened which ultimately leads to more controllable lifting devices.

2.1.3 Wavy Leading Edges Recapitulation

In the last two subsections the more relevant experimental and numerical studies found by the author have been revisited. Nevertheless because the amount of information to be processed by the reader might be too large a recapitulation subsection is provided here which highlight the most important findings as well as common and contrasting statements done by past researchers in the matter of WLEs.

Results are different depending on whether the wings studied where of finite span [4, 8, 34, 38, 41, 54, 57] or infinite span [7, 11, 18, 32, 35, 44, 49, 56]. The experiments with finite wings include wing tip vortices and separation usually starts at the tips of the wing and then progresses towards the root. None of this effects is present using the infinite wing approach.

The studies have all been carried out between a range of $800 \geq Re \geq 10^6$. The WLEs seem to perform better than the straight leading edge aerofoils in the post stall regime for any given Re [4, 8, 11, 18, 34, 35, 41, 54, 56, 57] but only in few cases turned out to be better than the baseline in the pre-stall regime [4, 34, 56]. This performance enhancement in the pre-stall regime is mainly present in experiments at low Re and finite wing arrangements. Anyway all papers reviewed seem to agree to say that WLEs tend to have softer stall characteristics.

Separation/Attachment patters have been related to the wavy leading edge profiles. The flow seems to easily separate at the troughs while it remains attached at the peaks [7, 11, 18, 44, 49, 54]. Different pressure distributions are also observed due to the WLEs with higher pressure zones on the peaks and lower pressure zones at the troughs [41, 56, 57]. This patterned behaviour in the spanwise direction seems to be related to the appearance of streamwise vortices [7, 11, 18, 41, 44, 49, 54, 57]. In particular Favier et al. [7] state that the vortices are created due to velocity gradients in the spanwise direction (faster flow in the troughs [7, 8]) which trigger Kelvin-Helmholtz instabilities. These instabilities create vortices in the vertical direction that are immediately tilted and convected by the mean flow. Hansen et al. [11] found out that the interaction between these vortices is governed by the tubercles wavelength λ. At the same time they also believe that similar to the Vortex Generators, the sweep angle A/λ defines the vortex structure. Hansen et al. [11] also compared the Vortex generator's device height with the tubercles amplitude.

Force fluctuation reductions have also been measured [7, 32] which makes the WLEs very promising for applications facing highly disrupted flow conditions. In particular Lau et al. [32] found out that WLEs can help to reduce the pressure fluctuations over a lifting surface interacting with inflow turbulent flows.

Although many experiments have been carried out, it is still unclear what are the physical mechanisms that make the WLEs to be much better in post-stall regime. Some researchers say that the partial attachment at the peaks would be the reason [18]. Others claim that the tubercles can act as spanwise fences that confines separation to the wing tips [35, 38, 41], whereas many of them claim that the main reason of better post-stall performance is due to momentum exchange in the boundary layer due to the vortical structures induced by the tubercles [8, 11, 34, 41]. Additionally there exists the believe that the partial attachment at the peaks is related to the streamwise vortices that reduce the effective angle of attack because of the downwash flow [54].

2.2 Tandem Aerofoils Review

In the introduction Chapter 1 it has been mentioned that investigations are carried out on a tandem aerofoil configuration where the second element will have a wavy leading edge. It is worthwhile then define what exactly is considered as a tandem configuration herein. Figure 2.1 represents a typical tandem configuration like the ones that will be tested during this project. The main parameters are the horizontal distance between the leading edges, i.e. Stagger = S, the vertical distance, i.e. Gap = G, and the angle of attack of each aerofoil, i.e. δ_1, and δ_2. The symbols O_1, and O_2 represent the coordinates at the leading edges of their respecting aerofoils. The difference between both angles of attack is commonly known as Decalage = $D = \delta_1 - \delta_2$.

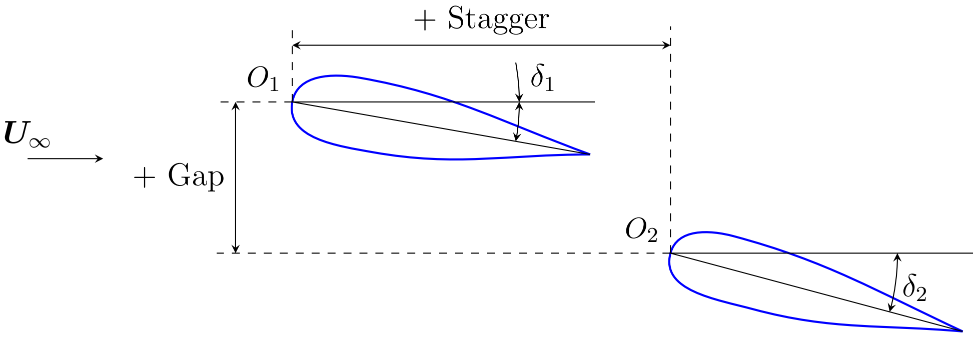

Figure 2.1: Tandem Configuration Parameters

This configuration has many applications. It can be used for simulating the effect of canard-wing interaction, or wing-tail interaction for example. If the second element is placed very close to the first it can be considered as a flap element although they usually tend to be much smaller than the main element. If the smaller element is the first one, it can be then considered as a slat element. Both flap and slat configurations are high-lift configurations. The main purpose of high-lift configurations is to increase the C_{lmax} of the main element at the expense of reducing the lifting capabilities of secondary elements. Tandem aerofoils are also representative of rotational lifting devices. Same spanwise sections of different blades can be seen as tandem aerofoils.

One of the most common direct applications of tandem aerofoils is the two-element high-lift arrangement. This is composed by a main aerofoil or element and a second, smaller element called flap. And for flap configurations the paper published by A.M.O. Smith in 1975 [50] might be the most referenced one. The author notes that the use of multi-element configurations for high-lift has been present since early XX century. Although it has been suggested that a single aerofoil shape can obtain the same amount of lift as a multi- element design, Smith states that properly designed multi-element are more convenient and that generally the greater the number of elements the greater the lift. Because of Bernoulli equation it is well known that that if the surface is to lift the velocity over it must be higher than that in the pressure surface. But when the flow reaches the trailing edge the flow is decelerated to velocities even lower than the free-stream. If this deceleration is too stiff it may cause separation because of the high adverse pressure gradient (APG). Two major aspects then arise when designing high-lift devices: 1) The analysis of the boundary layer, prediction of separation, and determination of the kinds of flows that are most favourable with respect to separation; and 2) analysis of the inviscid flow about a given shape with the purpose of finding shapes that put the least stress on the boundary layer.

Smith points out that one of the biggest misconceptions in multi-element aerodynamics is that slots supply a blowing type of boundary layer control. Instead the author highlights the five major effects present in a common high-lift configuration using multi-element aerofoils.

1. Slat effect: The circulation velocities of a former element, for example, a slat, run counter to the velocities on a downstream element in its LE zone and so reduce pressure peaks on the downstream element. The effect of this slat effect is to delay the stall angle. In the case of Tandem Aerofoils the aft element should stall at higher angles of attack.

2. Circulation effect: The upstream element is also benefited by the presence of the downstream element which causes the trailing edge of the adjacent upstream element to be in a region of high velocity that is inclined to the mean line at the rear of the forward element. Such flow inclination induces considerably greater circulation on the forward element.

3. Dumping effect: Because the trailing edge of a forward element is in a region of velocity appreciably higher than free-stream, hence the flow in the boundary layer does not suffer such a severe deceleration as it would happened in isolation. The higher discharge velocity relieves the pressure rise impressed on the boundary layer, thus alleviating separation problems or permitting increased lift.

4. Off-the-surface pressure recovery: The boundary layer from forward elements is dumped at velocities appreciably higher than free-stream. The final deceleration to free-stream velocity is done in an efficient manner. The deceleration of the wake occurs out of contact with a wall. Such a method is more effective than the best possible deceleration in contact with a wall.

5. Fresh-boundary-layer effect: Each new element starts out with a fresh boundary layer at its LE. Breaking up a flow into several short boundary layer runs reduces the risk of separation because thin boundary layers can withstand stronger adverse gradients than thick ones and thus lift can be increased.

To shed some light on this matter the past work of several researches is reviewed here concerning tandem aerofoil configurations. Rhodes [43] conducted inviscid computations they linked with a momentum integral boundary-layer analysis tool to investigate the effect of the key parameters of a *sweep-forward-sweep-rearward* (SFSR) tandem wing. Their parametric study showed that closely staggered aerofoils with negative decalage at a constant gap, enhanced the lifting capabilities in comparison with the single element. On the other hand, positive decalage performed poorly. The experiments showed that whatsoever the combination the flow of each wing was highly influenced by the presence of a second wing. For the fore wing the effect of the additional element was to have higher effective angle of attack whereas for the aft wing the effective angle of attack was reduced which agrees with [50]. In general decreasing the space in between the aerofoils tends to increase the efficiency of the hole system. But this improvement is no longer present if the elements are too close to each other when interaction becomes too strong. Increasing the angle AoA of the aft element results in an indirect increase of the fore element's lift and decrease of its drag. At the same time, having positive decalage, i.e. $\delta_1 > \delta_2$, is very much detrimental to the aft element.

Khan and Mueller [20] also performed a parametric study for a canard-wing system. The main purpose of their study was to investigate the effect of the relative position of the canard to the interaction of the canard's tip vortex and the downstream wing section. The were conducted in the open circuit South subsonic wind tunnel of the Aerospace Laboratory at Notre Dame. The parametric study focused on the gap and maintained a fixed value of stagger. The experiment focused on the low Reynolds number effects ($Re = 1.5 \times 10^5$ for these experiments), mainly the laminar separation bubbles. The results showed that when the aerofoils are located at $G = 0$ there exists a reduction on both lift and drag wing's coefficients. Nonetheless the reduction in drag is more drastic than that of lift and consequently an overall increase in the wings efficiency can be achieved. The drop in both coefficients is associated by Khan and Mueller [20] to the downwash and upwash effects of the canard's tip vortex. For a flow incidence angle of $\alpha = 0°$, in terms of drag, in the wing's upper surface, the upwash shifts the separation bubble upstream while the at the downwash region it is shifted downstream. At the same time, in the wing's lower surface there is no bubble in the inboard half of the wing's span, indicating that the flow remains laminar there. Khan and Mueller [20] state that that is the main reason for the drag decrease. If the incidence angle is increased to $\alpha = 10°$ the presence of turbulent boundary layer separation balances the gains obtained by increasing the laminar zone at the inboard zone and the wing's efficiency drops considerably. It was also observed that as the vertical distance between elements was increased the effect of the canard was less noticeable and the aerodynamic coefficients approached those of the single wing configuration. It is worth saying that the effect of the upstream element was weaker for configurations where the canard laid below the wing because the downwash effect is also weaker above the canard's wake [20].

Low Reynolds ($Re = 8.5 \times 10^4$ and 2×10^5) experiments were also conducted by Scharpf and Mueller [46]. However the experiments avoid the presence of tip vortices by the use of endplates. Force measurements were taken individually for each element at different angles of attack while the other element was kept at a fixed angle. On one hand, for a fixed δ_1, the lift coefficient of the aft element turned out to be lesser than that of the single aerofoil. Nonetheless whilst the single element stalled at $\alpha \approx 16°$ the tandem's second element did not stall for any of the tested δ_2's as suggested by Smith [50]. On the other hand, the tests at fixed δ_2 showed that the fore element of a tandem configuration has greater lift coefficients than the single element, and that these are even larger for larger values of δ_2 which was also anticipated by Smith [50]. Pressure distributions also confirm that the pressure peak is reduced for the aft element and that a less adverse pressure gradient is experienced by the fore element due to the presence of the downstream element. For both elements drag tend to be lower than that of the single element configuration for most of the tested angles. The authors conclude that the differences between the tandem and the single configurations are originated by the fact that although both elements are facing the same free stream conditions far upstream the effective angles of attack experienced by each of the aerofoils are completely modified by the presence of the other element. It is also noticeable that the tandem configuration increases the separation hysteresis range and that it is directly influenced by the decalage angle.

Fanjoy and Dorney [6] performed numerical simulations over a tandem aerofoil configuration formed by a pair of NACA 0012 aerofoils using an unsteady two-dimensional Navier-Stokes solver. The numerical scheme was 3rd order spatially and 2nd temporally accurate which used an upwind scheme for the inviscid fluxes and a standard central difference scheme for the viscous terms. The numerical integration was done implicitly and Newton sub-iteration were used at each global time step for numerical stability. The grid used combined an H-Grid and an O-Grid which were overlaid. The closest cells to the walls where of $y^+ = 0.5$. The investigations concerned different tandem configurations varying stagger S, and the flow incidence angle, but keeping the gap fixed at $G = 0$ at $Re = 6 \times 10^6$. A direct consequence of varying the angle of attack of the aerofoils by changing the free stream incidence is that the wake of the fore element, which is conducted by the bulk velocity, might avoid the aft element at even relatively small AoA. That technique is commonly used with single element aerofoils but has some issues when used with more than one aerofoil. Consequently for each run of fixed S, the relative angle of attack for the aft aerofoil was computed as well as the aerodynamic coefficients for both aerofoils. At $S = 4c$ the interaction between elements was already noticeable with the aft element seeing a smaller effective angle of attack. Further decrease of the stagger distance to $S = 3c$ made the effect become stronger, however at $S = 2c$ the effective AoA of the aft element was higher than for $S = 3c$. Independently of the effective AoA, the lift and the drag of the aft element decreased and increased respectively when decreasing the stagger. In contrast the performance of the fore aerofoil was substantially enhanced at lower stagger distances with increased lift and reduced drag. These results agree with [20, 43, 46, 50] which clearly shows that the increase of the fore element's performance is always at the expense of the detriment in the aft element.

Zhang and Yang [58] replicated the experiments of Scharpf [46] at $Re = 8.5 \times 10^4$ using a RANS approach with a $k - \epsilon$ turbulence model. They performed a parametric study for different decalage angles, gap and stagger distances. As previous results, the fore element, the canard, has enhanced capabilities compared to the single element case, but the aft element reduces its lifting capabilities. Nevertheless for the aft element, despite having less lift, its stall angle is increased by the presence of the upstream element. The authors [58] related the lift increase on the canard to the upwash flow field created by the wing and the detrimental effect on the wing with the downwash of the canard. As for the relative position of the aerofoils, the experiments showed that the best performance is achieved when the canard is located above the wing, i.e. when gap is positive as defined in Figure 2.1. It was also concluded that for the effect of tandem aerofoils be considerable the stagger distance has to be small enough because the experiments at 1.5 chord distance stagger showed greater lift increments for the canard (and also greater detriments for the wing) than those using 3 chord lengths of stagger distance.

At high angles of attack aerofoils start shedding vortices at its trailing edge. In a tandem configuration the vortices shed by the fore element have a direct impact on the second element. The effect of such interaction was investigated by Shirsath and Mukherjee [48] using two-dimensional Navier-Stokes computations with a SST $k-\omega$ turbulence model. Simulations were obviously of unsteady nature since they focused on the effect of the vortices coming from the fore element and then impinging in the aft aerofoil. For simulations where $\delta_1 = \delta_2$ the fore element tend to increase its lift after shedding a vortex progressively while the aft element experienced a significant peak at different time levels depending on the stagger distance due to the vortex probably climbing over its suction surface. The vortices carry low pressure in their cores which could explain why there exists such a sudden increase in lift on the rear aerofoil. The authors however did not mentioned any of this as the cause for the lift improvement and they just limited to describe the results obtained. After the lift peak, the aft aerofoil reduced its lift down to lower values of that of the fore element, as it had been reported in past papers. Another set of experiments were conducted by Shirsath and Mukherjee [48] at fixed δ_1 and different values for δ_2. Increasing δ_2 made the peak to be even stronger. It was also seen that for a fixed δ_1, increasing δ_2 not only increases the lift of the pitched aerofoil but also the upstream aerofoil's lift too with a sudden change in $\partial C_l/\partial t$ at the impingement moment.

2.3 High-Order Numerical Schemes Review

Because every problem in Fluid Mechanics is governed by a set of non-linear partial differential equations, i.e. the Navier-Stokes Equations, every problem tends to develop a very large range of length and time scales. So if maximum accuracy is requested, one has to fully resolve the entire range of scales, from the biggest to the smallest. However there are many different ways of approaching a problem which may give different results in terms of accuracy where the most accurate calculations are Direct Numerical Simulations (DNS) followed by the Large Eddy Simulations (LES) in second place. In the first mentioned, the whole range of scales is computed whereas for the second almost all the entire range is computed (resolved) and the effect of the rest, i.e. the effect of the smallest scales is modelled. There are however other methods that, although less accurate, do not require such big computational power as the ones just mentioned. An example of this could be the (U)RANS or Reynolds Averaged Navier-Stokes models.

Of the approaches mentioned beforehand the last is the preferred by the industry because can offer “quick” results up to some degree of accuracy whereas in research and academy more accurate methods are required. Other fields such as Aeroacoustics also demand a high level of accuracy, specially at the highest end of the wavelength spectrum. For such reasons, Spectral Methods have been traditionally used since they can faithfully represent the fluid dynamic variables and its derivatives among the whole range of scales.

Unfortunately the use of these methods strongly restricts the complexity of the geometries to study and the boundary conditions used. Other methods can overcome this limitations whilst still retaining the characteristic high-accuracy of the spectral methods up to some point. We focus here hence in one of these alternative methods, i.e. High-Order Compact (OHOC) Finite Difference schemes.

2.3.1 Interior Schemes

The basis of OHOC schemes is found in the Padé scheme in the form of its seven-point stencil which can be expressed as:

$$\beta f'_{i-2} + \alpha f'_{i-1} + f'_i + \alpha f'_{i+1} + \beta f'_{i+2} = c\frac{f_{i+3} - f_{i-3}}{6h} + b\frac{f_{i+2} - f_{i-2}}{4h} + a\frac{f_{i+1} - f_{i-1}}{2h} \tag{2.1}$$

Based on this, an approximation to the fist derivative was first suggested by Kreiss in 1974's Annual Review for Fluid Mechanics [37, p. 288] and lately tested by Hirsh [14]. Hirsh [14] stated that while standard High-Order Finite Difference schemes tend to use large stencils, the formulation shown in Equation 2.1 is much more compact, i.e. it uses only a grid point and its immediate neighbours, and thus allows the use of standard tridiagonal solvers such as the ones used with the 2nd order Central scheme whilst still retaining the 4th order of accuracy. But not only that but also comparing with the 4th order standard representation, although both exhibit the same order of accuracy, the compact scheme generates slightly more accurate results since the truncation coefficients are smaller.

On his 1992 paper, Lele [33] analysed the approximation of function derivatives in the form of Equation 2.1. Matching this equation with a Taylor series he obtained the following coefficient expressions for different orders of accuracy where the first unmatched coefficient determines the order of the truncation error.

$$a + b + c = 1 + 2\alpha + 2\beta \qquad \text{(second order)} \tag{2.2a}$$

$$a + 2^2 b + 3^2 c = 2\frac{3!}{2!}(\alpha + 2^2\beta) \qquad \text{(fourth order)} \tag{2.2b}$$

$$a + 2^4 b + 3^4 c = 2\frac{5!}{4!}(\alpha + 2^4\beta) \qquad \text{(sixth order)} \tag{2.2c}$$

$$a + 2^6 b + 3^6 c = 2\frac{7!}{6!}(\alpha + 2^6\beta) \qquad \text{(eighth order)} \tag{2.2d}$$

$$a + 2^8 b + 3^8 c = 2\frac{9!}{8!}(\alpha + 2^8\beta) \qquad \text{(tenth order)} \tag{2.2e}$$

It is noted that for the set of equations formed by Equations 2.1 and 2.2 if the system is restricted to $\beta = 0$ the derivatives can be obtained by solving a tridiagonal system of equations. However if β is nonzero the system is solved inverting a width-five banded matrix. Different parameter families can be obtained depending on the order of accuracy desired, e.g. a three-parameter family of 4th order is obtained using Equations 2.1, 2.2a, and 2.2b.

Although finite difference schemes are usually classified by their order of accuracy, Lele proposed a different way based on the Fourier analysis of the schemes' errors. The dependent variables are decomposed into their Fourier coefficients over a periodic domain $[0, L]$ with $\Delta x = L/N$ as:

$$f(x) = \sum_{k=-N/2}^{k=N/2} \hat{f}_k \exp\left(\frac{2\pi i k x}{L}\right) \tag{2.3}$$

If the scaled wavenumber $\kappa = w\Delta x = 2\pi k \Delta x/L = 2\pi k/N$ is used Equation 2.3 simplifies to just:

$$f(x) = \sum_{\kappa=-\pi}^{\kappa=\pi} \hat{f}_\kappa \exp\left(i\kappa x\right) \tag{2.4}$$

The exact differentiation of Equation 2.4 has coefficients $\hat{f}'_\kappa = i\kappa \hat{f}_\kappa$ whereas the use of finite difference approximations gives $(\hat{f}'_\kappa)_{fd} = i\bar{\kappa}\hat{f}$ where $\bar{\kappa} = \bar{w}\Delta x$ is the (scaled) modified wavenumber. The modified wavenumber is a function of the original wavenumber, i.e. $\bar{\kappa} = \bar{\kappa}(\kappa)$, and can be different for different derivative approximations. For schemes of the form of Equation 2.1 the modified wavenumber is given by:

$$\bar{\kappa}(\kappa) = \frac{a\sin(\kappa) + (b/2)\sin(2\kappa) + (c/3)\sin(3\kappa)}{1 + 2\alpha\cos(\kappa) + 2\beta\cos(2\kappa)} \tag{2.5}$$

Different schemes have different coefficients and hence the shape of its modified wavenumber is also different. Depending on how close a scheme's modified wavenumber remains to the exact solution determines the resolution characteristics of the scheme. Lele presented the *resolving efficiency* as the fraction of the entire wavenumber spectrum that a certain scheme is capable of approximate within a given error range. Thus depending on the formal accuracy imposed to Equation 2.1 different families of schemes with different sets of parameters are obtained, which will offer different characteristics in terms of its resolution when studied in the wavenumber domain. Higher order schemes will have more restrictions coming from Equation 2.2 and the number of free parameters will reduce, e.g. for a 10th order scheme a complete (closed) set of equations is obtained and therefore there are no free parameters making this scheme unique at that order of accuracy.

An interesting fact arising is that the lower the formal accuracy the most likely is a scheme to have high resolution characteristics. Because lower order models have more free parameters, more constraints can be added. In Lele [33] the modified wavenumber is forced to match the exact solution at three points. This gives three extra equations to add to the system formed by Equation 2.1 and 2.2. The result arising from this is the so called *spectral like resolution schemes*. The resulting scheme although being only 4th order accurate remains closer to the exact solution in the wavenumber domain for a wider range of wave numbers than for example the 10th order pentadiagonal scheme.

As mentioned by Lele [33], Compact Finite Difference schemes can be obtained from Equation 2.1. The schemes obtained can be forced to be accurate up to a certain order matching the corresponding Taylor series. Not aiming the highest possible order allows the creation of diverse free parameter scheme families. This free parameters can be used to restrict the schemes forcing them to enhance their resolution in the wavenumber domain. An step forward was taken by Kim [27] who adapted the strategy used by Tam and Web [51] to optimise the resolution of a central finite difference scheme, to optimise instead the compact schemes showed in [33]. In his paper, Kim presents a new set of finite difference schemes with maximum resolution obtained by an analytical optimisation procedure.

Kim uses the integrated error introduced in [51] with modifications to optimise the resolution characteristics of the Padé schemes. Minimising the error equals to optimise the schemes since an optimised schemes is understood as that that is able to reproduce the exact solution with minimum errors. Because most of the errors are made in the shorter waves, i.e. where the wavenumber approaches π, Kim uses a *Weighting Function* that first, makes the expression of the integrated error analytically integrable, and secondly, it weights the error towards the high end of the wavenumber spectrum forcing the resulting schemes to remain closer to the exact solution in that region where most of the errors are made. However Kim introduces a factor in the optimisation procedure that determines the range of wavenumbers where the minimisation of errors is going to be carried out. It turns out that at the very end of the spectrum, near π, the error is inevitably 1 due to Equation 2.5 being zero at $\kappa = \pi$. Then Kim stated that using a optimisation factor that covers the full range of wavenumbers is useless and additionally results in overshoot. In fact, Kim discovered that for every scheme there is a value of this factor that can produce optimum results bounding the overshoot error down to 0.5%.

Because the integrated error is a function that depends on the (scaled) modified wavenumber $\bar{\kappa}$, which at the same time depends on the coefficients a, b, c, α, and β, the minimum of the weighted error can be found where its derivatives respect to these coefficients equal zero (see [51]). Combining both sets of Equations 2.2 and the restrictions given in [51] a system of linear algebraic equations is obtained which is used to determine the values of the parameters a, b, c, α, and β appearing in Equation 2.1.

The minimisation of the integrated error is hence the key tool used by Kim to determine the optimum parameter values that make the modified wavenumber stay closer to the exact value within a wider range of wavenumbers and consequently increasing the resolution characteristics of the compact finite difference schemes.

Kim tested the most promising schemes by application to a simple wave convection problem in combination with a traditional 4^{th} Order Runge-Kutta method for time integration. The results showed that although some schemes have higher resolution characteristics, for obtaining accurate solutions it is also necessary to maintain a high level in the scheme's formal accuracy. Lower order compact schemes have more resolution in the wavenumber domain but their truncation error is also higher. Kim hence concludes that both the resolution as well as the truncation order determine the overall characteristics of the approximations. In addition it is mentioned that whether the schemes are tridiagonal ($\beta = 0$) or pentadiagonal ($\beta \neq 0$) has a strong effect on the scheme's global accuracy.

In a more recent piece of work Kim [21] introduced a newer version of his scheme presented in [27]. The optimisation procedure in this paper differed on the definition of the integrated error (see [27, p. 888-889]). A similar procedure was followed with first matching the Taylor series expansion of Equation 2.1 and then using Fourier transforms to operate in the wavenumber domain. Then the integrated error E was used to optimise the scheme's free coefficients in order to obtain maximum resolution characteristics.

However in this paper Kim adds two new variables to the game: δ, and n. It has been mentioned that aiming to a lower formal order of accuracy makes possible the use of extra constraints that can be used to determine the free parameters of a certain family of schemes and hence optimising them to produce accurate solutions within wider ranges of wavenumbers. However which coefficients in Equation 2.1 are used as free parameters has not been stated. The original choice of α, β, and c made in [27] was based on the fact that those are the extra coefficients not appearing in the standard formulation of a 4th order central difference scheme. Kim [21] tuned the optimisation parameters: r, δ, and n by trial and error until the best combination was found. He proved that independently of the chose of free parameters, similar results can be obtained if the optimisation parameters are adjusted accordingly.

2.3.2 Boundary Schemes

As one may notice the formulation showed up to now here can only be used if periodic boundary conditions are used. If non-trivial boundary conditions are aimed it is necessary to use a one-sided formulation, whose errors are of both dispersive and dissipative type. This near-boundary schemes must retain at least similar accuracy to that of the interior schemes since typically the global error tends to be dominated by the boundary error [33, p. 25]. The basis for the non-central or one-sided compact difference schemes can be found in Kim [26]. Again the author relies on the Padé schemes and the Fourier analysis to optimise the boundary schemes so dispersion, and dissipation as well since this time non-central stencils are used, are minimised.

As the interior schemes are based on the seven-point Padé formulation, it is clear that the interior formulation is no longer valid when applied to the nearest three points to any non-trivial boundary, i.e. $i = 0$, 1 and 2 where the boundary is at $i = 0$. Then using the same nomenclature as in [21] the expressions at the nearest three points is expressed as:

$$i = 0: \qquad \bar{f}'_0 + \alpha_{0,1}\bar{f}'_1 + \beta_{0,2}\bar{f}'_2 = \frac{1}{\Delta x}\sum_{j=0}^{3} a_{0,j} f_j, \tag{2.6a}$$

$$i = 1: \qquad \alpha_{1,0}\bar{f}'_0 + \bar{f}'_1 + \alpha_{1,2}\bar{f}'_2 + \beta_{1,3}\bar{f}'_3 = \frac{1}{\Delta x}\sum_{j=0}^{4} a_{1,j} f_j, \tag{2.6b}$$

$$i = 2: \qquad \beta_{2,0}\bar{f}'_0 + \alpha_{2,1}\bar{f}'_1 + \bar{f}'_2 + \alpha_{2,3}\bar{f}'_3 + \beta_{2,4}\bar{f}'_4 = \frac{1}{\Delta x}\sum_{j=0}^{5} a_{2,j} f_j. \tag{2.6c}$$

The formulation presented in Equation 2.6 is general and valid for both tridiagonal and pentadiagonal schemes, although for the tridiagonal schemes the coefficients $\beta_{i,j}$'s are equal to zero.

Following the procedure used in past papers, Kim shifts to the wavenumber domain to analyse the schemes. The Fourier transformation of Equation 2.6 yields to

$$\kappa[A(\kappa) + iB(\kappa)]\tilde{f} = [C(\kappa) + iD(\kappa)]\tilde{f}, \tag{2.7}$$

where A, B, C, and D are functions whose expressions can be found in [26, p. 181-182]. From this relation a similar expression to that on Equation 2.5 for the scaled modified wavenumber $\bar{\kappa}$ can be derived (see Equation 2.8). Because of the nature of the scheme (non-central) the expression for the modified wavenumber is in general complex in contrast with the interior scheme (central nature) which is pure real.

$$\bar{\kappa}(\kappa) = \frac{A(\kappa)C(\kappa) + B(\kappa)D(\kappa)}{[A(\kappa)]^2 + [B(\kappa)]^2} + i\frac{A(\kappa)D(\kappa) - B(\kappa)C(\kappa)}{[A(\kappa)]^2 + [B(\kappa)]^2} \tag{2.8}$$

The real part of Equation 2.8 is associated with the dispersion (phase) errors whereas its imaginary part is associated with dissipation (amplitude) errors. Therefore, the interior central scheme is non-dissipative, whereas the boundary non-central schemes are both dispersive and dissipative. The real part of the exact solution is given by $\mathrm{Re}(\bar{\kappa}) = \kappa$ and its imaginary part is given by $\mathrm{Im}(\bar{\kappa}) = 0$ since the exact solution has no dissipation. To minimise both errors Kim used the integrated error recast in a form which includes both errors in the formulation. The outcome of this optimisation were a new set of one-sided tridiagonal and pentadiagonal schemes with high accuracy and maximum resolution in terms of both dispersive and dissipative error. Additionally all the schemes presented in [26] were proved to be stable since the imaginary solutions of their modified wavenumber equation laid on the positive side of the imaginary axis. The exception to that is the 2nd order tridiagonal scheme which laid in the negative side. However as mentioned in [33] it is erroneous to conclude from the behaviour of the modified wavenumber that the scheme will lead to unstableness since the stability of the complete numerical scheme (including both interior and boundary schemes) must be determined by the appropriate eigenvalue analysis. In fact it turns out that the 2nd order tridiagonal scheme used with artificial selective damping did not lead to remarkable unstableness as stated by Kim [26, p. 186].

For problems involving non-trivial boundary conditions the Fourier analysis is not enough since can only be justified at a heuristic level [33]. The errors associated to the numerical scheme has to be assessed by numerical computations. Kim tested the combination of both interior and boundary schemes by computations of linear and non-linear wave problems with non-periodic boundary conditions for which high-quality results were obtained in both cases (see [26] for more detail).

In [21] Kim introduced the use of extrapolating functions in the form of splines formed by linear combination of polynomial and trigonometric functions in order to maintain the interior structure of the interior scheme near the boundaries. The extrapolating function provides virtual values outside the computational domain so the central scheme can be used at nodes $i = 0, i = 1$, and $i = 2$ (also at $i = N-2, i = N-1$, and $i = N$) where the boundary is located at $i = 0$ and $i = N$. The set of coefficients defining the spline functions were obtained by matching with the interior values of the objective function and its derivative and additionally requiring the extrapolating functions to be 4th order accurate. Kim additionally introduced an extra parameter in the trigonometric terms which then is used to optimise the schemes in the wavenumber domain.

Once the spline coefficients are obtained and expressed in terms of interior points which after some algebra and rearranging (see [21] for more details) take form of one-sided schemes expressed as:

$$i = 0: \qquad \bar{f}_0' + \gamma_{01}\bar{f}_1' + \gamma_{02}\bar{f}_2' = \frac{1}{\Delta x}\sum_{m=0,\neq 0}^{6} b_{0m}(f_m - f_0) \tag{2.9a}$$

$$i = 1: \qquad \gamma_{10}\bar{f}_0' + \bar{f}_1' + \gamma_{12}\bar{f}_2' + \gamma_{13}\bar{f}_3' = \frac{1}{\Delta x}\sum_{m=0,\neq 1}^{6} b_{1m}(f_m - f_1) \tag{2.9b}$$

$$i = 2: \qquad \gamma_{20}\bar{f}_0' + \gamma_{21}\bar{f}_1' + \bar{f}_2' + \gamma_{23}\bar{f}_3' + \gamma_{24}\bar{f}_4' = \frac{1}{\Delta x}\sum_{m=0,\neq 2}^{6} b_{2m}(f_m - f_2) \tag{2.9c}$$

The above equations can then close the pentadiagonal matrix (the shape of which originally comes from the application of 4th order pentadiagonal interior schemes) at the boundaries whilst maintaining the 4th order accuracy throughout. Nonetheless the parameters appearing in Equation 2.9 remain undefined since they are still non-linear functions of the extra parameter included in the trigonometric terms of the extrapolating functions. Kim used this extra parameters which he called *control variables* to maximise the range under which the relative deviation of the modified wavenumber respect the true wavenumber remained bounded between a certain error tolerance. For that Kim performed a Fourier analysis of Equation 2.9 that ended up with an expression of the form of Equation 2.8 (the expressions for functions A, B, C, and D, are different from those in [26] and can be found in [21, p. 1003]). As aforementioned Equation 2.8 is in general a complex function. For that reason Kim included in his definition of the maximum well-resolved wavenumber the influence of both dispersive (real) and dissipative (imaginary) errors by means of a weighted sum. The weighted sum allows to emphasise one of the errors over the other, however the author choice here was to equally weight both errors. The set of values for the control variables that produce maximum resolution characteristics can be found in [21, Table 3].

The outcome of Kim's work were a new set of one-sided boundary schemes with improved resolution with respect to older versions which additionally were derived requiring stricter error tolerances (the new schemes are bounded by an error tolerance of 0.3% in the worst case whereas for the older schemes an error tolerance of 0.5% was used).

As regards the stability of the combined new boundary schemes and interior schemes appearing in [21] Kim performed an eigenvalue analysis which showed that most of the eigenvalues were located in the negative side of the real axis (where the scheme is stable). However some of the eigenvalues with highest absolute value of its imaginary part were found to have positive real parts. Fortunately these eigenvalues were of small order of magnitude and they converge to zero as the number of calculation points increased. In practice it is found out by the author that those components are neutrally stable and do not produce any instabilities during calculations. Kim tested the new set of OHOC schemes against several bench cases such as: the one-dimensional scalar wave convection, the two-dimensional vorticity wave convection and the sound wave scattered by two rigid circular cylinders of different sizes. In the first two cases the scheme was applied to a simple Cartesian domain with equally spaced grid points whereas in the third case due to the complex geometry a multi-block H-type structured mesh was used. For the last case mentioned with discontinuous grid metrics *Characteristic interface boundary conditions*(see [29]) which will be mentioned in this report in following chapters and *Non-reflecting boundary conditions* (see [28]) were used. The implementation of the here mentioned OHOC schemes turned out to be successful with increased performance and accuracy though their application to benchmark cases.

Chapter 3

Methodology

3.1 Governing Equations

The governing equations of every fluid flow are described by the Navier-Stokes equations. These set of Partial Differential Equations (PDEs) describe how velocity, pressure, and density are related. The equations cast in conservation form are expressed in Equation 3.1 as

$$\frac{\partial \boldsymbol{Q}}{\partial t} + \frac{\partial \boldsymbol{E}}{\partial x} + \frac{\partial \boldsymbol{F}}{\partial y} + \frac{\partial \boldsymbol{G}}{\partial z} = \boldsymbol{S}_v = \frac{1}{Re_\infty}\left(\frac{\partial \boldsymbol{E}_v}{\partial x} + \frac{\partial \boldsymbol{F}_v}{\partial y} + \frac{\partial \boldsymbol{G}_v}{\partial z}\right), \tag{3.1}$$

where the conservative variables vector is $\boldsymbol{Q} = [\rho, \rho u, \rho v, \rho w, \rho e]^T$ and the with ρ, u, v, w, and e being: density, x-velocity component, y-velocity component, z-velocity component, and energy respectively. The vectors $\boldsymbol{E}$, $\boldsymbol{F}$, and $\boldsymbol{G}$ represent the inviscid flux terms and $\boldsymbol{E}_v$, $\boldsymbol{F}_v$, and $\boldsymbol{G}_v$ are the viscous flux terms. The expressions for the flux vectors are

$$\begin{aligned}
\boldsymbol{E} &= [\rho u, \rho u^2 + p, \rho uv, \rho uw, (\rho e + p)u]^T,\\
\boldsymbol{F} &= [\rho v, \rho uv, \rho v^2 + p, \rho vw, (\rho e + p)v]^T,\\
\boldsymbol{G} &= [\rho w, \rho uw, \rho vw, \rho w^2 + p, (\rho e + p)w]^T,\\
\text{where} \quad p &= \rho(\gamma - 1)\left[e - \frac{u^2 + v^2 + w^2}{2}\right]
\end{aligned}$$

and for the viscous terms

$$\begin{aligned}
\boldsymbol{E_v} &= [0, \tau_{xx}, \tau_{xy}, \tau_{xz}, (u\tau_{xx} + v\tau_{xy} + w\tau_{xz} + q_x)]^T,\\
\boldsymbol{F_v} &= [0, \tau_{xy}, \tau_{yy}, \tau_{yz}, (u\tau_{xy} + v\tau_{yy} + w\tau_{yz} + q_y)]^T,\\
\boldsymbol{G_v} &= [0, \tau_{xz}, \tau_{yz}, \tau_{zz}, (u\tau_{xz} + v\tau_{yz} + w\tau_{zz} + q_z)]^T.
\end{aligned}$$

where τ_{ij} is the stress tensor the components which expressed in Einstein notation, i.e. $x = x_1, y = x_2, z = x_3$ and $u = u_1, v = u_2$, and $w = u_3$, are

$$\tau_{ij} = \mu\left(\frac{\partial u_i}{\partial x_j} + \frac{\partial u_j}{\partial x_i}\right) + \delta_{ij}\lambda\frac{\partial u_i}{\partial x_i}. \tag{3.4}$$

In this equation μ represents the dynamic viscosity coefficient and λ represents the bulk coefficient viscosity. Also the heat fluxes q_i expressed in Einstein notation are

$$q_i = \frac{\mu}{(\gamma - 1) Pr Re_\infty M_\infty^2} \frac{\partial T}{\partial x_i}, \tag{3.5}$$

and Re_∞, M_∞ and Pr are the free stream Reynolds number and Mach number and the Prandtl number respectively.

One may notice that if viscous effects are neglected in the Navier-Stokes equations then the Right Hand Side (RHS) of Equation 3.1 disappears and the equations then simply to

$$\frac{\partial \boldsymbol{Q}}{\partial t} + \frac{\partial \boldsymbol{E}}{\partial x} + \frac{\partial \boldsymbol{F}}{\partial y} + \frac{\partial \boldsymbol{G}}{\partial z} = 0. \tag{3.6}$$

which are known also as the Euler equations. It can be seen that the assumption of inviscid flow is much more valid when the Reynolds number is high, i.e. the RHS of Equation 3.1 vanishes.

The technique used to solve this set of equations is based on Finite Difference (FD) methods , which were already reviewed in the last chapter and will be described with detail in the following sections. However the use of FD is more convenient for domains that have been discretised in cartesian grids with homogeneous grid spacing which allows the system of PDEs to be solved as a system of algebraic equations. Unfortunately this is not possible in most of the problems which involve complex geometries, and that is the case here. In this case it is usual to work in what are commonly known as Generalized coordinates ξ, η, ζ. In this coordinate system, where the spacing is constant Equation 3.1 is expressed as

$$\frac{\partial \hat{\boldsymbol{Q}}}{\partial t} + \frac{\partial \hat{\boldsymbol{E}}}{\partial \xi} + \frac{\partial \hat{\boldsymbol{F}}}{\partial \eta} + \frac{\partial \hat{\boldsymbol{G}}}{\partial \zeta} = \hat{\boldsymbol{S}}_v = \frac{1}{Re_\infty} \left(\frac{\partial \hat{\boldsymbol{E}}_v}{\partial \xi} + \frac{\partial \hat{\boldsymbol{F}}_v}{\partial \eta} + \frac{\partial \hat{\boldsymbol{G}}_v}{\partial \zeta} \right), \tag{3.7}$$

where the variables in the original coordinate system are related to the new ones by the Jacobian of the transformation J as

$$\hat{\boldsymbol{Q}} = \boldsymbol{Q}/J,$$

$$J = 1/[x_\xi (y_\eta z_\zeta - y_\zeta z_\eta) + x_\eta (y_\zeta z_\xi - y_\xi z_\zeta) + x_\zeta (y_\xi z_\eta - y_\eta z_\xi)]$$

$$\begin{aligned}
\hat{\boldsymbol{E}} &= (1/J)(\xi_x \boldsymbol{E} + \xi_y \boldsymbol{F} + \xi_z \boldsymbol{G}), &\quad \hat{\boldsymbol{E}}_v &= (1/J)(\xi_x \boldsymbol{E}_v + \xi_y \boldsymbol{F}_v + \xi_z \boldsymbol{G}_v), \\
\hat{\boldsymbol{F}} &= (1/J)(\eta_x \boldsymbol{E} + \eta_y \boldsymbol{F} + \eta_z \boldsymbol{G}), &\quad \hat{\boldsymbol{F}}_v &= (1/J)(\eta_x \boldsymbol{E}_v + \eta_y \boldsymbol{F}_v + \eta_z \boldsymbol{G}_v), \\
\hat{\boldsymbol{G}} &= (1/J)(\zeta_x \boldsymbol{E} + \zeta_y \boldsymbol{F} + \zeta_z \boldsymbol{G}), &\quad \hat{\boldsymbol{G}}_v &= (1/J)(\zeta_x \boldsymbol{E}_v + \zeta_y \boldsymbol{F}_v + \zeta_z \boldsymbol{G}_v).
\end{aligned}$$

$$\begin{pmatrix} \xi_x & \xi_y & \xi_z \\ \eta_x & \eta_y & \eta_z \\ \zeta_x & \zeta_y & \zeta_z \end{pmatrix} = J \begin{pmatrix} y_\eta z_\zeta - y_\zeta z_\eta & z_\eta x_\zeta - z_\zeta x_\eta & x_\eta y_\zeta - x_\zeta y_\eta \\ y_\zeta z_\xi - y_\xi z_\zeta & z_\zeta x_\xi - z_\xi x_\zeta & x_\zeta y_\xi - x_\xi y_\zeta \\ y_\xi z_\xi - y_\zeta z_\xi & z_\zeta x_\xi - z_\zeta x_\xi & x_\xi y_\eta - x_\eta y_\xi \end{pmatrix}$$

where ξ_x represents the derivative of x with respect to ξ. This terms are known as grid metrics and their inverse, i.e. x_ξ, the inverse grid metrics.

Now that the domain is discretised in equally spaced grid points in all three directions the flux and source terms can be differentiated using FD schemes. In this report the spatial differentiation technique used is the one proposed by Kim [21] described in Chapter 2. The following sections will describe the schemes used for both the schemes used for differentiation of the interior grid points, i.e. nodes in the range $3 \geq i \geq N-3$ where N represents the maximum number of points in one direction, and the ones used for the near boundary nodes, i.e. nodes 0,1,2 and N,N-1, and N-2.

3.2 Large Eddy Simulations Equations

For this project the technique chosen to tackle the turbulence modelling problem was the Implicit LES method (ILES). With this method Equation 3.1 is solved numerically and then filtered so oscillations of wavenumber beyond the filter's cut-off wavenumber are removed from the final solution. By this means the energy containing eddies are fully resolved whilst the smallest eddies remain unresolved, and whose effect on the final solution is supposed to be equivalent to the numerical dissipation inherited by the numerical schemes used. This technique reduces the effort required to get the final solution compared to regular LES methods which add an additional diffusion term to Equation 3.1 that needs to be computed at each time step.

When using the traditional LES approach, Equation 3.1 is transformed to its Favre Averaged version using a density weighted average, i.e. the so called Favre Averaging, technique shown in Equation 3.8

$$\tilde{\phi} = \frac{\widehat{\rho\phi}}{\hat{\rho}}, \tag{3.8}$$

where the hat denotes the filter operation and the tilde the Favre operation. Here $\tilde{\phi}$ represents the resolved part of ϕ, and the correspondent unresolved part is denoted by

$$\phi'' = \phi - \tilde{\phi}. \tag{3.9}$$

Applying the above operation to the Navier-Stokes equations, and using Einstein notation results into

$$\frac{\partial \hat{\rho}}{\partial t} + \frac{\partial}{\partial x_i}[\hat{\rho}\widetilde{x}_i] = 0 \tag{3.10a}$$

$$\frac{\partial}{\partial t}(\hat{\rho}\widetilde{u}_i) + \frac{\partial}{\partial x_j}\left[\hat{\rho}\widetilde{u}_i\widetilde{u}_j + \hat{p}\delta_{ij} + \underbrace{\widehat{\rho u_i'' u_j''}}_{(1)} - \widetilde{\tau}_{ji} - \underbrace{\widehat{\tau_{ji}''}}_{(2)}\right] = 0 \tag{3.10b}$$

$$\begin{aligned}\frac{\partial}{\partial t}(\hat{\rho}\tilde{e}) + \frac{\partial}{\partial x_j}\Bigg[&\hat{\rho}\widetilde{u}_j\tilde{e} + \widetilde{u}_j\hat{p} + \underbrace{C_p\widehat{\rho u_j'' T}}_{(3)} + \underbrace{\widetilde{u}_i\widehat{\rho u_i'' u_j''}}_{(4)} \\ &+ \underbrace{\frac{1}{2}\widehat{\rho u_j'' u_i'' u_i''}}_{(5)} + q_j - \underbrace{C_p\frac{\mu}{Pr}\frac{\partial \widehat{T''}}{\partial x_j}}_{(6)} - \widetilde{u}_i\widetilde{\tau}_{ij} - \underbrace{\widehat{u_i''\tau_{ij}}}_{(7)} - \underbrace{\widetilde{u}_i\widehat{\tau_{ij}''}}_{(8)}\Bigg] = 0\end{aligned} \tag{3.10c}$$

where the terms (1) to (8) are all unknown. Luckily terms (2) and (8) are neglected since the stresses from the resolved field tend in general to be much bigger than those of the unresolved field. For flows not reaching the hyper-sonic regime it is also common to neglect terms (5) and (7). Additionally term (6) can also be neglected in cases where

$$\left|\frac{\partial^2 \tilde{T}}{\partial x_j^2}\right| >> \left|\frac{\partial^2 \widehat{T''}}{\partial x_j^2}\right|,$$

which is true in all common flows. Finally, terms (1) and (4) can be modeled using an eddy-viscosity model such as

$$\tau_{ij}^{\mathrm{SGS}} \equiv -\widehat{\rho u_i'' u_j''} \approx \mu^{\mathrm{SGS}}\left(\frac{\partial \widetilde{u}_i}{\partial x_j} + \frac{\partial \widetilde{u}_j}{\partial x_i} - \frac{2}{3}\frac{\partial \widetilde{u}_k}{\partial x_k}\delta_{ij}\right) - \frac{2}{3}\hat{\rho}k^{\mathrm{SGS}}\delta_{ij}, \tag{3.11a}$$

$$\mu^{\mathrm{SGS}} = \hat{\rho}C_{s_1}\Delta^2\sqrt{2\widetilde{S_{ij}}\widetilde{S_{ij}}}, \tag{3.11b}$$

$$k^{\mathrm{SGS}} = C_{s_2}\Delta^2\widetilde{S_{ij}}\widetilde{S_{ij}}, \tag{3.11c}$$

where $\Delta = \sqrt[3]{\Delta x \Delta y \Delta z}$ is the cubic root of the cell volume, C_{s_1} and C_{s_2} are model constants usually set to 0.012 and 0.0066 respectively, and $\widetilde{S_{ij}}$ is the resolved strain rate tensor. To close the set of equations, term (3) is modelled using a gradient approximation as

$$q_j^{\mathrm{SGS}} \equiv C_p\widehat{\rho u_j'' T} \approx -C_p\frac{\mu^{\mathrm{SGS}}}{Pr_t}\frac{\partial \tilde{T}}{\partial x_j}, \tag{3.12}$$

which leads to the simplified form of

$$\frac{\partial \hat{\rho}}{\partial t} + \frac{\partial}{\partial x_i}[\hat{\rho}\widetilde{x_i}] = 0, \tag{3.13a}$$

$$\frac{\partial}{\partial t}(\hat{\rho}\widetilde{u_i}) + \frac{\partial}{\partial x_j}\left[\hat{\rho}\widetilde{u_i}\widetilde{u_j} + \hat{p}\delta_{ij} - \tau_{ji}^{\mathrm{TOT}}\right] = 0, \tag{3.13b}$$

$$\frac{\partial}{\partial t}(\hat{\rho}\tilde{e}) + \frac{\partial}{\partial x_j}\left[\hat{\rho}\widetilde{u_j}\tilde{e} + \widetilde{u_j}\hat{p} + q_j^{\mathrm{TOT}} - \widetilde{u_i}\tau_{ij}^{\mathrm{TOT}}\right] = 0, \tag{3.13c}$$

$$\tau_{ij}^{\mathrm{TOT}} = \widetilde{\tau_{ji}} + \tau_{ji}^{\mathrm{SGS}}, \tag{3.13d}$$

$$q_j^{\mathrm{TOT}} = q_j + q_j^{\mathrm{SGS}}, \tag{3.13e}$$

with all terms depending on the resolved quantities.

It is clear now how the ILES methodology is less computationally expensive than traditional LES since all Sub-Grid Scales (SGS) are implicitly modelled by the numeric schemes.

3.3 Interior Scheme

As aforementioned the OHOC finite difference schemes developed by Kim [21] are 4th order accurate numerical schemes optimised to achieve the maximum resolution in the wavenumber domain based on the Padé approximation of a seven-point stencil. The general expression for this is

$$\beta\bar{f}'_{i-2} + \alpha\bar{f}'_{i-1} + \bar{f}'_i + \alpha\bar{f}'_{i+1} + \beta\bar{f}'_{i+2} = \frac{1}{\Delta x}\sum_{m=1}^{3} a_m(f_{i+m} - f_{i-m}), \tag{3.14}$$

where f_i and $\bar{f}'_i$ represent the function to differentiate and its numerical representation of its spacial derivative with respect to x at the point x_i in the interval $\Delta x = x_{i+1} - x_i$.Matching coefficients with its Taylor expansion up to 4th order leads to the following conditions:

$$1 + 2(\alpha + \beta) = 2\sum_{m=1}^{3} m a_m, \tag{3.15a}$$

$$3(\alpha + 4\beta) = \sum_{m=1}^{3} m^3 a_m. \tag{3.15b}$$

If the dependent variable $f(x)$ is decomposed into its Fourier coefficients over a periodic domain $[0, L]$ with $\Delta x = L/N$ as

$$f(x) = \sum_{k=-N/2}^{k=N/2} \hat{f}_k \exp\left(\frac{2\pi i k x}{L}\right), \tag{3.16}$$

then if the scaled wavenumber $\kappa = w\Delta x = 2\pi k \Delta x / L = 2\pi k / N$ is used Equation 3.16 simplifies to just

$$f(x) = \sum_{\kappa=-\pi}^{\kappa=\pi} \hat{f}_\kappa \exp{(i\kappa x)}\,. \tag{3.17}$$

The exact differentiation of Equation 3.17 has coefficients $\hat{f}'_\kappa = i\kappa \hat{f}_\kappa$ whereas the use of finite difference approximations gives $(\hat{f}'_\kappa)_{fd} = i\bar{\kappa}\hat{f}$ where $\bar{\kappa} = \bar{w}\Delta x$ is the (scaled) modified wavenumber. The modified wavenumber is a function of the original wavenumber, i.e. $\bar{\kappa} = \bar{\kappa}(\kappa)$, and can be different for different derivative approximations. For schemes of the form of Equation 3.14 the modified wavenumber is given by:

$$\bar{\kappa}(\kappa) = \frac{2\sum_{m=1}^{3} a_m \sin(m\kappa)}{1 + 2\alpha\cos{(\kappa)} + 2\beta\cos{(2\kappa)}} \tag{3.18}$$

It can be seen in Figure 3.1 that for different schemes different curves are obtained, where the red straight dashed line corresponds to the exact differentiation. If κ_f is defined as the wavenumber related to the shortest well-resolved wave then an error tolerance ε can be defined as

$$\varepsilon = \frac{\bar{\kappa}(\kappa_f) - \kappa_f}{\kappa_f}, \tag{3.19}$$

and for a fixed value of ε all the wavenumbers that satisfy Equation 3.20 represent well-resolved waves, being $\kappa = \kappa_f(\varepsilon)$ consequently the biggest among them.

$$\frac{\bar{\kappa}(\kappa) - \kappa}{\kappa} \leq \varepsilon \tag{3.20}$$

Taking all this into account, the fraction of the spectrum representing poorly-resolved waves is $r(\varepsilon) \equiv 1 - \kappa_f/\pi$ and $e(\varepsilon) \equiv \kappa_f/\pi = 1 - r(\varepsilon)$ is the *resolving efficiency* of the scheme. The total error made by the approximations can be calculated by the integrated error E defined below.

$$E = \int_0^{r\pi} (\kappa - \bar{\kappa})^2 W(\kappa)\, d\kappa \tag{3.21}$$

Where r and $W(\kappa)$ are introduced representing the factor determining the range $(0 < r < \pi)$ where errors are accounted and the weighting function respectively. The introduction of the weighting function is necessary for two main reasons. In first place it makes possible to optimise the schemes to reduce the errors in the high-wavenumber range where most of the errors are made. Secondly, it simply makes Equation 3.21 analytically integrable. Kim proposes to replace $\bar{\kappa}$ by $(1+\delta)\kappa$ and the use of $W(\kappa) = [\kappa/(r\pi)]^n$ as weighting function which results into the following expression of the integrated error:

$$E = \int_0^{r\pi} \left\{ (1+\delta)\kappa[1 + 2\alpha\cos{(\kappa)} + 2\beta\cos{(2\kappa)}] - 2\sum_{m=1}^{3} a_m \sin{(mk)} \right\}^2 \left(\frac{\kappa}{r\pi}\right)^n d\kappa \tag{3.22}$$

Table 3.1: Interior Scheme Coefficients

α	β	a_1	a_2	a_3
0.5862704032801503	0.09549533555017055	0.6431406736919156	0.2586011023495066	0.007140953479797375

Table 3.2: Optimisation parameters

r	δ	n
0.8505	-0.000233	10

As mentioned in the literature review, minimising this error equals to maximise the spectral resolution of the schemes. The conditions for minimum values of E where given by Tam and Webb [51] in the form of

$$\frac{\partial E}{\partial a_1} = 0, \quad \frac{\partial E}{\partial a_1} = 0, \quad \frac{\partial E}{\partial a_3} = 0, \quad \frac{\partial E}{\partial \alpha} = 0, \quad \frac{\partial E}{\partial \beta} = 0. \tag{3.23}$$

If the minimum conditions of Equation 3.23 are combined with the restrictions that makes Equation 3.14 4th Order accurate, i.e. Equation 3.15 (see also Equation 2.2), a closed system of equations is obtained from where the coefficients α, β, a_1, a_2 and a_3 can be obtained once the optimisation parameters r, δ and n have been fixed. The values used here are the ones that Kim [21] suggests and can be checked out from Table 3.2 which lead to the scheme coefficients shown in Table 3.1.

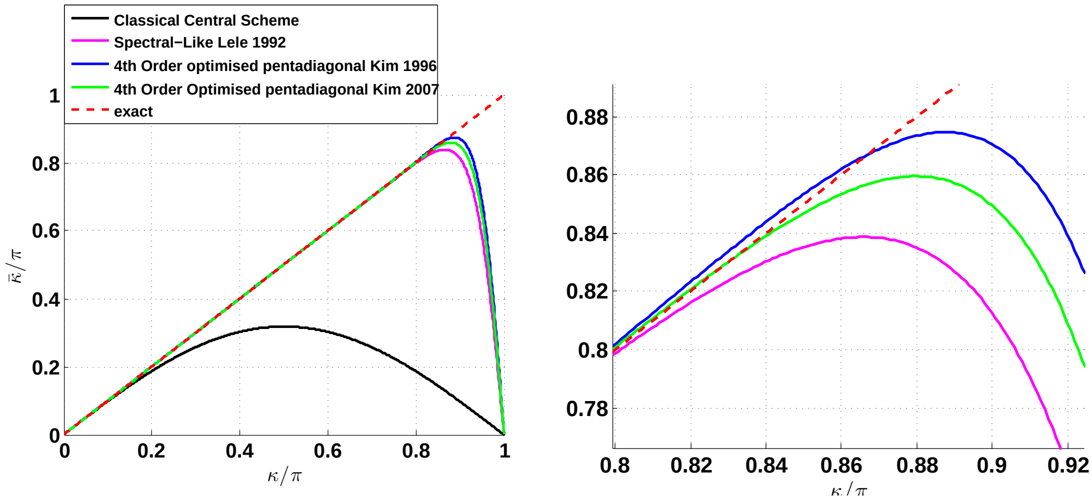

(a) Full view

(b) Zoomed view

Figure 3.1: Comparison of different numerical schemes resolution capabilities

The resulting resolution characteristics of the scheme are shown in comparison with other compact finite differences in Figure 3.1a. One may say that the older scheme presented in [27] (blue line) is able to mimic the exact solution for a larger range of wavenumbers than that presented in [21] and used here (green line). However the zoomed view shows that this is done with the expense of larger error tolerance in the optimised region. Just for the sake of comparison the classical central scheme is also represented.

It is seen that the classical scheme is only able to faithfully represent the exact solution for the first 20% of the spectral range. The coefficients of the scheme used for this study can be found in Table 3.1.

3.4 Boundary Scheme

Because the interior scheme needs information on both sides of the point of interest to compute its derivative it is not suitable for problems with non-periodic boundary conditions. In the case of the problem tackled here there exist a need for a scheme that allows the implementation of non-periodic boundaries such as walls in the aerofoil surface. In such cases the scheme is of necessity non-central (or one-sided). Fortunately in the literature review such a scheme has been covered and hence will be used for this study. This is the boundary scheme developed by Kim [21] which unlike its previous version [26] includes extrapolation techniques to obtain the information outside the computational domain boundaries. On this purpose the following spline function is used:

$$g_i(x^*) = f_i + \sum_{m=1}^{N_A} p_m (x^*)^m + \sum_{m=1}^{N_B} [q_m \cos(\phi_m x^*) + r_m \sin(\phi_m x^*)], \tag{3.24a}$$

$$\begin{aligned} g_i'(x^*) &= \frac{dg_i(x^*)}{dx} \\ &= \frac{1}{\Delta x} \left\{ \sum_{m=1}^{N_A} m p_m (x^*)^{m-1} - \sum_{m=1}^{N_B} \phi_m [q_m \sin(\phi_m x^*) - r_m \cos(\phi_m x^*)] \right\}, \end{aligned} \tag{3.24b}$$

where $x^* = (x - x_i)/\Delta x$ is the non-dimensional coordinate from the point of interest, N_A, and N_B determine the order of the polynomial and trigonometric series, the coefficients p_m, q_m and r_m are used to match the interior values for both the objective function and its derivative, and ϕ_m are control variables used to optimise the resolution characteristics of the boundary scheme when the exterior points of Equation 3.14 are substituted by extrapolated values.

Matching the interior profile of the objective function one may obtain the values for the coefficients p_n, q_m, and r_m where $n = [1, \cdots, N_A]$ and $m = [1, \cdots, N_B]$, expressed in terms of the interior values of the objective function. For a 4th order approximation the requirements are that (N_A, N_B) equal $(4, 3), (4, 4)$ and $(4, 4)$ for the nearest three boundary points respectively. Rearranging terms the interior scheme can be recast in a one-sided formulation including just interior values of the function and the unknown coefficients $\gamma_{i,j}$ and b_{0m}, b_{1m} and b_{2m} where $i = 0, 1, 2$, $j = 0, 1, 2$, and $m = [1, \cdots, 6]$ with $i \neq j$ and $m \neq i$ This unknown coefficients are all non-linear functions of the control variables, i.e. $\phi_1, \cdots, \phi_{N_B}$. The resulting formulation was already presented in

Subsection 2.3.2[Equation 2.9] but will be again retyped here for convenience.

$$i = 0: \qquad \bar{f}'_0 + \gamma_{01}\bar{f}'_1 + \gamma_{02}\bar{f}'_2 = \frac{1}{\Delta x}\sum_{m=0,\neq 0}^{6} b_{0m}(f_m - f_0) \tag{3.25a}$$

$$i = 1: \qquad \gamma_{10}\bar{f}'_0 + \bar{f}'_1 + \gamma_{12}\bar{f}'_2 + \gamma_{13}\bar{f}'_3 = \frac{1}{\Delta x}\sum_{m=0,\neq 1}^{6} b_{1m}(f_m - f_1) \tag{3.25b}$$

$$i = 2: \qquad \gamma_{20}\bar{f}'_0 + \gamma_{21}\bar{f}'_1 + \bar{f}'_2 + \gamma_{23}\bar{f}'_3 + \gamma_{24}\bar{f}'_4 = \frac{1}{\Delta x}\sum_{m=0,\neq 2}^{6} b_{2m}(f_m - f_2) \tag{3.25c}$$

It was also mentioned in the literature review that Kim [21] relied in the Fourier analysis for the definition of these parameters so the maximum resolution of the schemes was accomplished. Applying Fourier transforms to Equation 3.25 and grouping terms leads to the following expression of the modified wave number (see also Equation 2.7 and Equation 2.8 which are obtained by the same procedure)

$$\bar{\kappa}(\kappa) = \frac{A(\kappa)D(\kappa) - B(\kappa)C(\kappa)}{[A(\kappa)]^2 + [B(\kappa)]^2} - i\frac{A(\kappa)C(\kappa) + B(\kappa)D(\kappa)}{[A(\kappa)]^2 + [B(\kappa)]^2}, \tag{3.26}$$

where the expressions of the functions $A, B, C,$ and D can be found in [21, p. 1003]. It can be noted that Equation 3.26 has both real and imaginary parts and consequently has dispersion and dissipation errors. Both errors can be measured as

$$\varepsilon_R(\kappa) = \left|\frac{\mathrm{Re}[\bar{\kappa}(\kappa)] - \kappa}{\kappa}\right|, \tag{3.27a}$$

$$\varepsilon_I(\kappa) = \left|\frac{\mathrm{Im}[\bar{\kappa}(\kappa)]}{\kappa}\right|. \tag{3.27b}$$

It can be then defined a wavenumber κ_c^σ up to which the numerical scheme approximates the true solution within a maximum error tolerance σ. This is

$$\kappa_c^\sigma = \frac{1}{2}(\kappa_{Rc}^\sigma + \kappa_{Ic}^\sigma) \tag{3.28a}$$

$$\kappa_{Rc}^\sigma = \min(\kappa|\varepsilon_R(\kappa) = \sigma, 0 < \kappa < \pi), \tag{3.28b}$$

$$\kappa_{Ic}^\sigma = \min(\kappa|\varepsilon_I(\kappa) = \sigma, 0 < \kappa < \pi), \tag{3.28c}$$

where κ_{Rc}^σ and κ_{Ic}^σ represent the wavenumber up to which the numerical differentiation can approximate the true solution within a error tolerance σ in its real and imaginary parts respectively. Then the values of ϕ_m that define the rest of the constants in Equation 3.25 are computed by an iterative Newton-Raphson method that maximises the value of κ_c^σ. Kim [21] used a error tolerance of $\sigma = 0.001$, 0.002, and 0.003 for $i = 2$, 1 and 0 respectivelly which lead to the values of Table 3.3.

Table 3.3: Boundary Scheme Coefficients

Coefficients	$i = 0$	$i = 1$	$i = 2$
γ_{i0}	–	0.08360703307833438	0.03250008295108466
γ_{i1}	5.912678614078549	–	0.3998040493524358
γ_{i2}	3.775623951744012	2.058102869495757	–
γ_{i3}	–	0.9704052014790193	0.7719261277615860
γ_{i4}	–	–	0.1626635931256900
b_{i0}	–	-0.3177447290722621	-0.1219006056449124
b_{i1}	-3.456878182643609	–	-0.6301651351188667
b_{i2}	5.839043358834730	-0.02807631929593225	–
b_{i3}	1.015886726041007	1.593461635747659	0.6521195063966084
b_{i4}	-0.226526470654333	0.2533027046976367	0.3938843551210350
b_{i5}	0.3938843551210350	-0.03619652460174756	0.01904944407973912
b_{i6}	-0.01836710059356763	0.004080281417108407	-0.001057260523947668

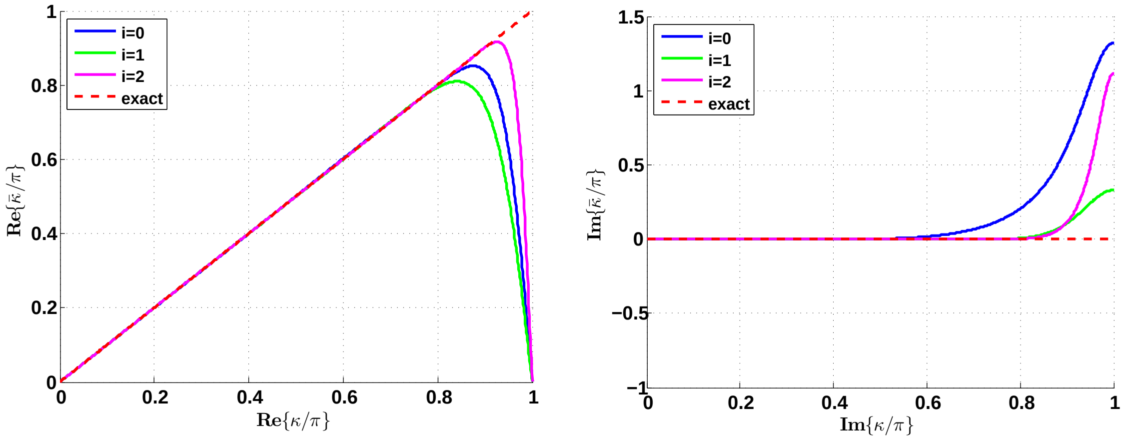

(a) Dispersion Errors

(b) Dissipation Errors

Figure 3.2: Modified Wavenumber vs. Wavenumber. a) Real Part, b) Imaginary Part.

Figure 3.2 shows the modified-wavenumber profiles for all three boundary points. It is seen that the most accurate in terms of dispersive errors is the scheme cast at node $i = 2$ and as the nodes get closer to the boundary, and hence need more points coming from extrapolation, the resolution of the schemes slightly decays. As regards the Dissipation discrepancies, the scheme cast at $i = 1$ seems to be the closest to the true solution despite being the less accurate dispersion-wise.

3.5 High-Order Compact Filters

The numerical recipes for spatial differentiation have been described in the last section. It has been shown that the methods used in this study are able to faithfully represent the true analytical differentiation up to very high wavenumbers (when transformed to the wavenumber domain). Nevertheless it is impossible to generate a finite difference approximation that covers the entire spectra without any error. As a consequence if the results are taken just straight away after the numerical differentiation without any kind of treatment, the errors made in the very high end of the wavenumber spectrum will be included in the final solution. Additionally it has been shown that the grid topology is directly included in the governing equations when transformed to the generalized coordinate system (see Equation 3.7). If the grid is not smooth enough (as it happens in body-fitted curvilinear grids), spurious waves can easily develop at those regions. On top of that, the boundary schemes are dissipative at high wavenumbers but the interior OHOC schemes are of non-dissipative nature because of its central formulation. Consequently, with the lack of numerical dissipation, the errors made can grow unboundedly and highly deteriorate the quality of the results.

There exists then the necessity of a numerical treatment that removes this spurious solutions and makes the general algorithm stable. For this reasons dissipative numerical schemes are chosen to control the errors growth. Other methods of doing this is to add artificially extra dissipation to the equations. The method chosen in this investigation is based on High-Order Compact Filters, and to be more exact, the method used is the one developed by Kim [22] which removes the spurious solution up to a user defined *"cut-off wavenumber"* (κ_C).

The filters have a similar formulation to the differentiating schemes and hence there is an interior version of the filter and also a boundary version. The filter used in the interior nodes has the following differential form

$$\beta\hat{\Delta}f_{i-2} + \alpha\hat{\Delta}f_{i-1} + \hat{\Delta}f_i + \alpha\hat{\Delta}f_{i+1} + \beta\hat{\Delta}f_{i+2} = \sum_{m=1}^{3} a_m(f_{i-m} - 2f_i + f_{i+m}), \tag{3.29}$$

where $\hat{\Delta}f_i = \hat{f}_i - f_i$ is the difference between the filtered value and the original with the hat representing the filtered value. In equation Equation 3.29 there are five unknown coefficients. Taylor expanding Equation 3.29 up to sixth-order and matching coefficients provides two extra equations leaving just three free parameters. The rest of the parameters are defined after shifting to the wavenumber domain where they can be expressed in terms of the cut-off wavenumber. The transfer function between the filtered and the unfiltered fields $T(\kappa)$ can be obtained in the wavenumber domain where $T(\kappa) = 1$ means no-filtering and $T(\kappa) = 0$ means complete filtering. The free parameters are fixed so the following conditions are met:

$$T(\pi) = 0 \tag{3.30a}$$

$$\frac{d^2T(\pi)}{d\kappa^2} = 0 \tag{3.30b}$$

$$T(\kappa_C) = \frac{1}{2} \tag{3.30c}$$

The last condition defines the cut-off wavenumber as the wavenumber where the transfer function gives "half-filtering". Adding these constraints to the system of equations fully defines the interior filter's coefficients in terms of the desired cut-off wavenumber.

For the boundary nodes, e.g. $i = 0, i = 1$ and $i = 2$ for a left boundary, the interior filters are no longer valid since exterior domain values are demanded in Equation 3.29. Kim [22] uses a 4th order polynomial extrapolating function to obtain these external values as a function of the interior values. The extrapolating function is of the form of

$$g(x^*) = f_0 + \sum_{m=1}^{4} c_m (x^*)^m, \tag{3.31a}$$

$$\hat{\Delta} g(x^*) = \hat{\Delta} f_0 + \sum_{m=1}^{4} d_m (x^*)^m, \tag{3.31b}$$

where again $x^* = (x - x_0)$ is a dimensionless distance from the boundary point as it happened with the extrapolating functions used for the derivation of the boundary finite difference scheme. However the extrapolating function are only based on polynomials for which eight coefficients need to be defined given the 4th order of formal accuracy requested. Six equations can be derived by matching the interior values while still preserving the pentadiagonal shape at the boundary. Extra equations are obtained by blending the boundary filter with the interior filter. The resulting boundary filter is

$$i = 0 : \hat{\Delta} f_0 + \gamma_{01} \hat{\Delta} f_1 + \gamma_{02} \hat{\Delta} f_2 = 0 \tag{3.32a}$$

$$i = 1 : \gamma_{10} \hat{\Delta} f_0 + \hat{\Delta} f_1 + \gamma_{12} \hat{\Delta} f_2 + \gamma_{13} \hat{\Delta} f_3 = 0 \tag{3.32b}$$

$$i = 2 : \gamma_{20} \hat{\Delta} f_0 + \gamma_{21} \hat{\Delta} f_1 + \hat{\Delta} f_2 + \gamma_{23} \hat{\Delta} f_3 + \gamma_{24} \hat{\Delta} f_4 = \sum_{m=0,\neq 2}^{5} b_{2m} (f_m - f_2), \tag{3.32c}$$

where all the coefficients depend on the values of the interior filter's parameters (for more detailed expressions of the boundary filter parameters see [22, Eq. 3.6]). Because the interior parameters are given by functions of the cut-off wavenumber, so are the boundary ones. It is possible to apply different cut-off wave numbers depending on the grid position. It is usual to have lower resolution schemes in the boundaries and hence it is desirable to increase the filtering on those zones. Increasing the filtering of the original function is achieved by a reduction in the cut-off wave number. For such reason the cut-off wavenumber could be defined by

$$\kappa_{C_i} = \begin{cases} \kappa_C & \text{for } 3 \leq i \leq N-3 \\ (1-\varepsilon)\kappa_C & \text{for } i = 2 \wedge N-2 \\ (1-2\varepsilon)\kappa_C & \text{for } i = 1 \wedge N-1 \\ (1-3\varepsilon)\kappa_C & \text{for } i = 0 \wedge N \end{cases}, \tag{3.33}$$

where ε is a weighting factor that makes κ_C smaller close to a boundary. The optimum value of this weighting factor was found to be $\varepsilon = 0.085$ by Kim [22] after performing a linear stability analysis of the combination of both filters and both difference schemes. This is the maximum value of ε that maintains the differencing-filtering system stable for $0.5\pi \leq \kappa_C \leq 0.88\pi$, i.e. the range where the system is stable for a fixed cut-off wavenumber all over the domain.

3.6 Grid Generation

In Section 3.1 it has been shown that working in the generalised coordinates allows the use of finite difference techniques designed for constant spacing rectangular grids. However, despite the grid in generalised coordinates might be rectangular, the actual problem in physical coordinates is still a body fitted curvilinear mesh. There are several methods available for the generation of structured curvilinear grids, e.g. conformal mapping, elliptic, or algebraic grid generation [9].

The grid used in this study is generated using algebraic grid generation combined with a multi-block strategy. The algebraic mesh generation is done defining the points on the boundaries, the interior grid points are then obtained by interpolation between the boundaries. The multi-block technique consists in splitting the domain in smaller subdomains called blocks. For each of the blocks the points are collocated at the boundaries and then interior ones are interpolated. It is important to try to resemble the computational grid as much as possible so the transformation between coordinate systems remains simpler. Also it is important to maintain continuity in the spacing between adjacent blocks up to the first spacing derivative (although continuity in the second derivative is also desirable). The main reason for this to happens is because of the grid metrics, i.e. $\xi_x, \xi_y, \xi_z, \eta_x, \cdots, \zeta_z$, directly appear in the governing equations when transformed to the generalised coordinates. Any discontinuities (in the discrete sense) in the spacing will increase the value of the grid metrics in great manner. So poor quality cells, like skewed or high aspect ratio cells, will also trigger errors that due to the low dissipative characteristic of the high-order methods described in the last section will be unmanageable. For that reason the grid has to be of very good quality.

The spacing between the nodes is controlled by the first derivative of the grid functions $x(\xi, \eta, \zeta), y(\xi, \eta, \zeta)$ and $z(\xi, \eta, \zeta)$. So for example if the spacing in the ξ direction for the x-coordinate it will be required that $\partial^2 x/\partial \xi^2$ is a continuous function. The grid for this study is generated using an in-house Fortran code that ensures the C–2 continuity of the grid function. The method used is easily understood if it is illustrated with a simple one-dimensional example.

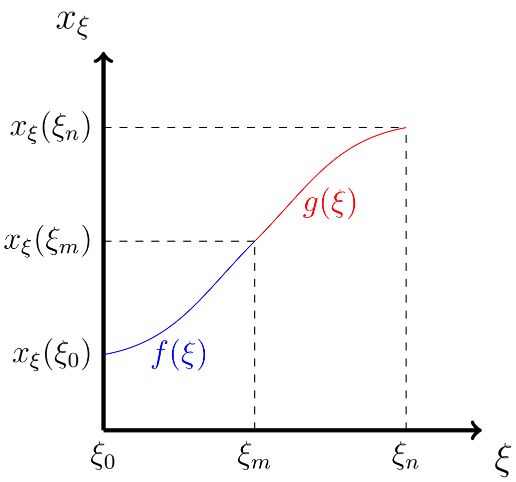

Figure 3.3: 1–D Grid Function Matching Example

In Figure 3.3 the grid function derivative has been plotted. It is a piecewise function formed by the function $f(\xi)$ for $\xi_0 < \xi < \xi_m$ and the function $g(\xi)$ for $\xi_m < \xi < \xi_n$. Here ξ_0 represents the start point of a boundary line and ξ_n represents the end point, whereas ξ_m is the point where the two functions f_a and f_b blend with C–1 continuity. Now, imagine two consecutive lines where grid points are to be collocated so the grid metrics vary smoothly. To ensure smooth variation function g_a of the first line has to blend with function f_b of the second line (subscript indicates line). For that to happen the following conditions have to be met:

$$x_a(\xi_n) = x_b(\xi_0) \qquad g_b(\xi_n) = f_a(\xi_0) \qquad g_b'(\xi_n) = f_a'(\xi_0), \tag{3.34a}$$

where the prime indicates derivation with respect to ξ. Note that constant value of the slope in Figure 3.3 means constant spacing between points with higher slopes indicating more distance between points. If the slope of $x_\xi(\xi)$ is then kept low at the boundaries ξ_0 and ξ_n, the points will be clustered at the extremes of the grid line. Using this method the points are defined in the boundaries of the blocks shown in Figure 3.4 where the numbers inside the block represent the block's id. The interior points are then simply interpolated from the values on the block boundaries. The result can be observed in Figure 3.5.

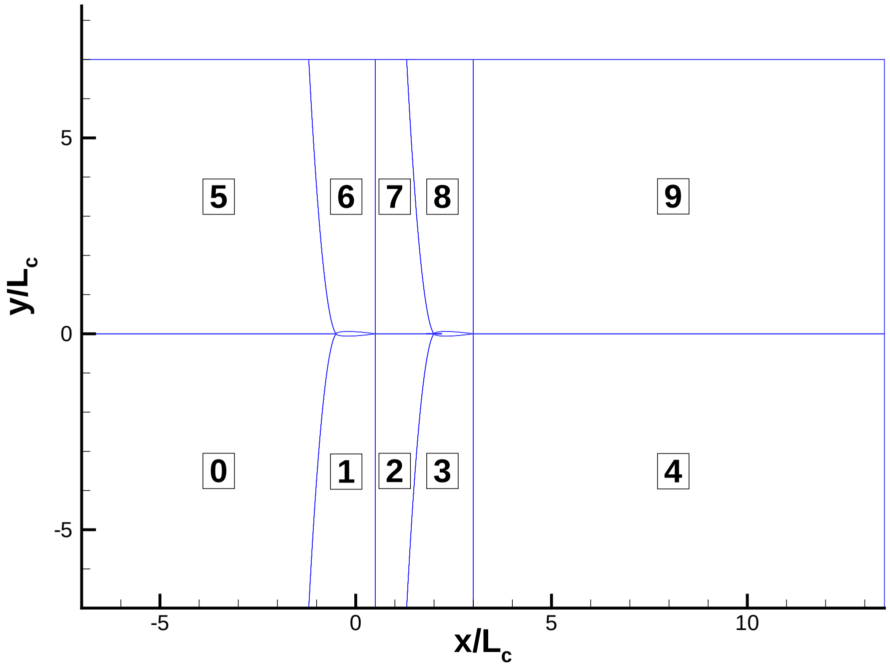

Figure 3.4: Grid Blocks

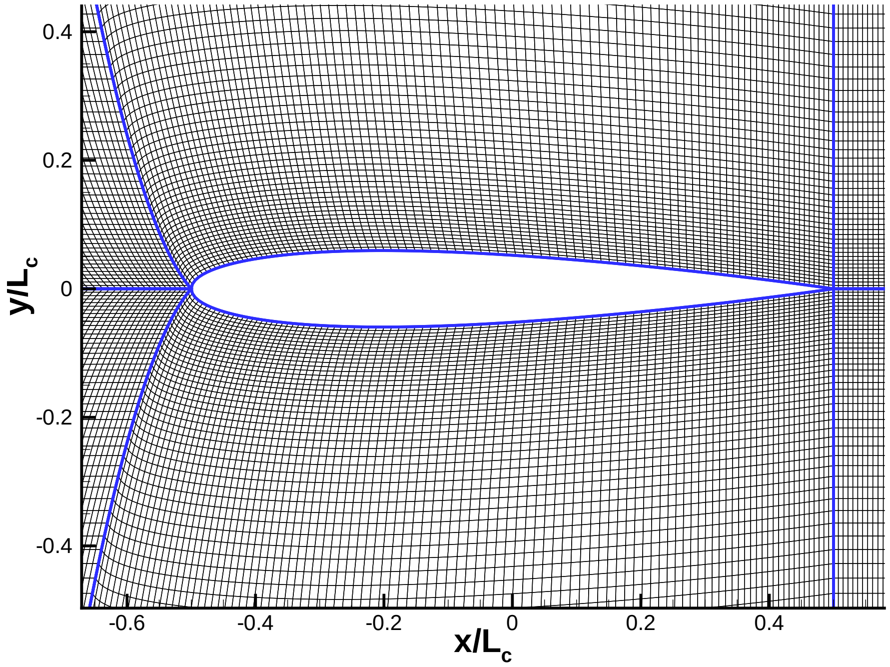

Figure 3.5: Aerofoil Zone Zoomed Grid

In Figure 3.5 it can be seen that the leading edge of the aerofoils is a complicated zone where is impossible to achieve continuity of all the grid functions. This regions are very prone to develop numerical errors that will feed into the final solution. For that reason it is indispensable to have some treatment in between block internal boundaries which will be discussed in the next sections. However it is wise to start calling these internal boundaries “block interfaces”. The physical boundaries of the computational domain are simply called boundaries herein.

3.7 Boundary Conditions

Solving a system of Partial Differential Equations it is usually known as solving the Boundary Value Problem. This is, the solution sought is a function that can uniquely represent the interior values for the given boundary conditions. The boundary conditions should represent the solution offside the solution domain and its influence on the solution. In one-dimensional problems for example, at its left boundary, the information is shared between the interior and the exterior at the boundary, where the effect of the external solution information is fed into the computational domain by means of waves of positive phase velocity, i.e. are propagating towards the interior of the domain. On the other hand, waves with negative phase velocity will transport information from the interior domain towards the exterior. At the right boundary the same would happen with opposite velocity signs.

The outgoing waves are fully determined by the interior solution, however the incoming waves need to be specified by the user in what is known as boundary conditions. Several approaches can be used for the definition of the boundary conditions, although here the generalised characteristic boundary conditions [25, 28, 52, 53]. For that starting from Equation 3.1 which is recovered here is necessary.

$$\frac{\partial \boldsymbol{Q}}{\partial t} + \frac{\partial \boldsymbol{E}}{\partial x} + \frac{\partial \boldsymbol{F}}{\partial y} + \frac{\partial \boldsymbol{G}}{\partial z} = \boldsymbol{S}_v, \tag{3.35}$$

A quasi-linear expression can be achieved using the following jacobian matrices:

$$\boldsymbol{A} = \frac{\partial \boldsymbol{E}}{\partial \boldsymbol{Q}}, \qquad \boldsymbol{B} = \frac{\partial \boldsymbol{F}}{\partial \boldsymbol{Q}}, \qquad \boldsymbol{C} = \frac{\partial \boldsymbol{G}}{\partial \boldsymbol{Q}}, \tag{3.36}$$

using them on Equation 3.35 the following quasi-linear expression is obtained:

$$\frac{\partial \boldsymbol{Q}}{\partial t} + \boldsymbol{A}\frac{\partial \boldsymbol{Q}}{\partial x} + \boldsymbol{B}\frac{\partial \boldsymbol{Q}}{\partial y} + \boldsymbol{C}\frac{\partial \boldsymbol{Q}}{\partial z} = \boldsymbol{S}_v. \tag{3.37}$$

Since the jacobian matrices, and their eigenvectors have simpler forms when the primitive variables $\boldsymbol{Q'} = [\rho, u, v, w, p]^T$ are used, Equation 3.37 can be transformed to

$$\begin{gathered}\boldsymbol{M}\frac{\partial \boldsymbol{Q'}}{\partial t} + \boldsymbol{AM}\frac{\partial \boldsymbol{Q'}}{\partial x} + \boldsymbol{BM}\frac{\partial \boldsymbol{Q'}}{\partial y} + \boldsymbol{CM}\frac{\partial \boldsymbol{Q'}}{\partial z} = \boldsymbol{S}_s = \\ \frac{\partial \boldsymbol{Q'}}{\partial t} + \boldsymbol{A'}\frac{\partial \boldsymbol{Q'}}{\partial x} + \boldsymbol{B'}\frac{\partial \boldsymbol{Q'}}{\partial y} + \boldsymbol{C'}\frac{\partial \boldsymbol{Q'}}{\partial z} = \boldsymbol{M}^{-1}\boldsymbol{S}_v = \boldsymbol{S}'_v,\end{gathered} \tag{3.38}$$

where

$$\boldsymbol{M} = \frac{\partial \boldsymbol{Q}}{\partial \boldsymbol{Q'}} = \begin{pmatrix} 1 & 0 & 0 & 0 & 0 \\ u & \rho & 0 & 0 & 0 \\ v & 0 & \rho & 0 & 0 \\ w & 0 & 0 & \rho & 0 \\ \frac{u^2+v^2+w^2}{2} & \rho u & \rho v & \rho w & \frac{1}{\gamma-1} \end{pmatrix} \tag{3.39}$$

and

$$\boldsymbol{A'} = \boldsymbol{M^{-1}AM}, \qquad \boldsymbol{B'} = \boldsymbol{M^{-1}BM}, \qquad \boldsymbol{C'} = \boldsymbol{M^{-1}CM}, \qquad \boldsymbol{S'_v} = \boldsymbol{M^{-1}S_v} \tag{3.40}$$

Transformation of Equations 3.37 and 3.38 to the generalised coordinates ξ, η, and ζ, is obtain by the chain rule.

$$\frac{\partial \boldsymbol{Q}}{\partial t} + \boldsymbol{K}_\xi \frac{\partial \boldsymbol{Q}}{\partial \xi} + \boldsymbol{K}_\eta \frac{\partial \boldsymbol{Q}}{\partial \eta} + \boldsymbol{K}_\zeta \frac{\partial \boldsymbol{Q}}{\partial \zeta} = \boldsymbol{S}_v, \tag{3.41a}$$

$$\frac{\partial \boldsymbol{Q'}}{\partial t} + \boldsymbol{K'_\xi} \frac{\partial \boldsymbol{Q'}}{\partial \xi} + \boldsymbol{K'_\eta} \frac{\partial \boldsymbol{Q'}}{\partial \eta} + \boldsymbol{K'_\zeta} \frac{\partial \boldsymbol{Q'}}{\partial \zeta} = \boldsymbol{S'_v}. \tag{3.41b}$$

where for example the flux jacobian matrices $\boldsymbol{K_\xi}$ and $\boldsymbol{K'_\xi}$ are given by

$$\boldsymbol{K}_\xi = \xi_x \boldsymbol{A} + \xi_y \boldsymbol{B} + \xi_z \boldsymbol{C}, \tag{3.42a}$$

$$\boldsymbol{K'_\xi} = \xi_x \boldsymbol{A'} + \xi_y \boldsymbol{B'} + \xi_z \boldsymbol{C'}, \tag{3.42b}$$

which are projections of $\boldsymbol{A}$, $\boldsymbol{A}'$, $\boldsymbol{B}$, $\boldsymbol{B}'$, $\boldsymbol{C}$, and $\boldsymbol{C'}$ on the direction $\boldsymbol{\xi} = [\xi_x, \xi_y, \xi_z]$, which is normal to a given plane of constant ξ.

Again the relation between both matrices is given by $\boldsymbol{M}$ as

$$\boldsymbol{K}_\xi = \boldsymbol{M K'_\xi M^{-1}} \tag{3.43}$$

The elements of the flux jacobian matrix $\boldsymbol{K'_\xi}$ is given by Hirsch [13, Equations 16.5.1 and 16.5.2], and recovered here

$$\boldsymbol{K'_\xi} = \boldsymbol{A'} \cdot \boldsymbol{\xi} = \begin{pmatrix} U_\xi & \rho\xi_x & \rho\xi_y & \rho\xi_z & 0 \\ 0 & U_\xi & 0 & 0 & \xi_x/\rho \\ 0 & 0 & U_\xi & 0 & \xi_y/\rho \\ 0 & 0 & 0 & U_\xi & \xi_z/\rho \\ 0 & \rho c^2\xi_x & \rho c^2\xi_y & \rho c^2\xi_z & U_\xi \end{pmatrix} \tag{3.44}$$

with

$$\begin{aligned} \boldsymbol{U} &= [u, v, w], \\ \boldsymbol{\xi} &= [\xi_x, \xi_y, \xi_z], \\ U_\xi &= \boldsymbol{U} \cdot \boldsymbol{\xi} = u\xi_x + v\xi_y + w\xi_z. \end{aligned} \tag{3.45}$$

The diagonalisation of $\boldsymbol{K'_x} i$ is given by

$$\boldsymbol{K'_\xi} = \boldsymbol{P'} \boldsymbol{\Lambda} \boldsymbol{P'}^{-1}, \tag{3.46}$$

where $\boldsymbol{\Lambda} = \boldsymbol{I\lambda}$ is the matrix containing the eigenvalues of $\boldsymbol{K'_\xi}$, which are:

$$\boldsymbol{\lambda} = [U_\xi, U_\xi, U_\xi, U_\xi + c|\boldsymbol{\xi}|, U_\xi - c|\boldsymbol{\xi}|]. \tag{3.47}$$

And $\boldsymbol{P'}$ and $\boldsymbol{P'}^{-1}$ are the right and left eigenvector matrices respectively. Using Equation 3.43 one can also define for the conservative variables the following matrices:

$$\boldsymbol{P} = \boldsymbol{MP'}, \tag{3.48a}$$

$$\boldsymbol{P}^{-1} = \boldsymbol{MP'}^{-1}, \tag{3.48b}$$

$$\boldsymbol{K}_\xi = \boldsymbol{P\Lambda P}^{-1}, \tag{3.48c}$$

which then, by moving the terms involving spatial derivatives with respect to η and ζ to the RHS of Equation 3.41 and merging all terms in a new source term $\boldsymbol{S}_v'^*$ the following expression is obtained:

$$\frac{\partial \boldsymbol{Q}}{\partial t} + \boldsymbol{K}_\xi \frac{\partial \boldsymbol{Q}}{\partial \xi} = \boldsymbol{S}_v^* = \boldsymbol{S}_v - \left(\boldsymbol{K}_\eta \frac{\partial \boldsymbol{Q}}{\partial \eta} + \boldsymbol{K}_\zeta \frac{\partial \boldsymbol{Q}}{\partial \zeta} \right), \tag{3.49a}$$

$$\frac{\partial \boldsymbol{Q'}}{\partial t} + \boldsymbol{K}_\xi' \frac{\partial \boldsymbol{Q'}}{\partial \xi} = \boldsymbol{S}_v'^* = \boldsymbol{S}_v' - \left(\boldsymbol{K}_\eta' \frac{\partial \boldsymbol{Q'}}{\partial \eta} + \boldsymbol{K}_\zeta' \frac{\partial \boldsymbol{Q'}}{\partial \zeta} \right). \tag{3.49b}$$

The system of Equation 3.49 can be written in characteristic by premultilication by $\boldsymbol{P'}^{-1}$, and $\boldsymbol{P}^{-1}$ respectively to obtain:

$$\boldsymbol{P}^{-1} \frac{\partial \boldsymbol{Q}}{\partial t} + \boldsymbol{P}^{-1} \boldsymbol{K}_\xi \frac{\partial \boldsymbol{Q}}{\partial \xi} = \boldsymbol{P}^{-1} \boldsymbol{S}_v^*, \tag{3.50a}$$

$$\boldsymbol{P'}^{-1} \frac{\partial \boldsymbol{Q'}}{\partial t} + \boldsymbol{P'}^{-1} \boldsymbol{K}_\xi' \frac{\partial \boldsymbol{Q'}}{\partial \xi} = \boldsymbol{P'}^{-1} \boldsymbol{S}_v'^*, \tag{3.50b}$$

then using the following relations

$$\begin{aligned} \tilde{\boldsymbol{\xi}} &= \frac{\boldsymbol{\xi}}{|\boldsymbol{\xi}|}, & \delta \tilde{U}_\xi &= \tilde{\xi}_x \delta u + \tilde{\xi}_y \delta v + \tilde{\xi}_z \delta w \\ \delta \tilde{\vartheta}_1 &= \tilde{\xi}_z \delta v - \tilde{\xi}_y \delta w, & \delta \tilde{\vartheta}_2 &= -\tilde{\xi}_z \delta u + \tilde{\xi}_x \delta w, \\ \delta \tilde{\vartheta}_3 &= \tilde{\xi}_y \delta u - \tilde{\xi}_x \delta v, \end{aligned} \tag{3.51}$$

and

$$\delta \boldsymbol{R} = \boldsymbol{P}^{-1} \delta \boldsymbol{Q} = \boldsymbol{P'}^{-1} \delta \boldsymbol{Q'} \quad = \begin{pmatrix} \tilde{\xi}_x (\delta \rho - \delta p / c^2) + \delta \tilde{\vartheta}_1 \\ \tilde{\xi}_y (\delta \rho - \delta p / c^2) + \delta \tilde{\vartheta}_2 \\ \tilde{\xi}_z (\delta \rho - \delta p / c^2) + \delta \tilde{\vartheta}_3 \\ \delta p / \rho c + \delta \tilde{U}_\xi \\ \delta p / \rho c - \delta \tilde{U}_\xi \end{pmatrix} \tag{3.52}$$

finally the following expression is obtained:

$$\frac{\partial \boldsymbol{R}}{\partial t} + \boldsymbol{\Lambda} \frac{\partial \boldsymbol{R}}{\partial \xi} = \boldsymbol{S}_c = \boldsymbol{P}^{-1} \boldsymbol{S}_v^* = \boldsymbol{P'}^{-1} \boldsymbol{S}_v'^* \tag{3.53}$$

U_ξ and δU_ξ represent the velocity normal to the boundary and its derivative, and $\tilde{\boldsymbol{\xi}}$ the unitary boundary normal vector. The terms $\delta\vartheta_1$, $\delta\vartheta_2$ and $\delta\vartheta_3$ are the projections of the velocity vector on the intersection lines formed by the normal plane defined by $\tilde{\boldsymbol{\xi}}$ and the yz, xz, and xy planes respectively. They are all three perpendicular to $\tilde{\boldsymbol{\xi}}$ consequently when written as the vectors $\delta\tilde{\boldsymbol{\vartheta}}_1 = [0, \tilde{\xi}_z \delta v, -\tilde{\xi}_y \delta w]$, $\delta\tilde{\boldsymbol{\vartheta}}_2 = [-\tilde{\xi}_z \delta u, 0, \tilde{\xi}_x \delta w]$, and $\delta\tilde{\boldsymbol{\vartheta}}_3 = [\tilde{\xi}_y \delta u, -\tilde{\xi}_x \delta v, 0]$. The terms in the diagonal of $\boldsymbol{\Lambda}$ represent the entropy (first term), vorticity (second and third) and acoustic (fourth and fifth) waves. It is clear that the entropy and vorticity waves always convect with the flow at the boundary whereas velocity convection of the acoustic waves depend on the value of c, i.e. the sound speed. For subsonic flows the first fourth waves are entering the domain whereas the fifth is exiting for a inlet boundary considered at $\xi = 0$. At the outlet, $\xi = N$, on the contrary, just the fifth mode represents an incoming wave whereas the rest are outgoing waves. Equation 3.53 is a quasi-one-dimensional expression, basis of the boundary treatment developed by Kim and Lee [25, 28]. Detailed definitions of the matrix terms can be found in [25, 28]. The second term in Equation 3.53 is the convection term in characteristic form. Its relation to the original convection term is given by

$$\xi_x \frac{\partial \boldsymbol{E}}{\partial \xi} + \xi_y \frac{\partial \boldsymbol{F}}{\partial \xi} + \xi_z \frac{\partial \boldsymbol{G}}{\partial \xi} = \boldsymbol{P\Lambda} \frac{\partial \boldsymbol{R}}{\partial \xi} = \boldsymbol{PL}. \tag{3.54}$$

The matrices $\boldsymbol{P'}^{-1}$ and $\boldsymbol{P'}$ are:

$$\boldsymbol{P'}^{-1} = \frac{\rho}{c} \begin{pmatrix} \tilde{\xi}_x c/\rho & 0 & \tilde{\xi}_z & -\tilde{\xi}_y & -\tilde{\xi}_x/(\rho c) \\ \tilde{\xi}_y c/\rho & -\tilde{\xi}_z & 0 & \tilde{\xi}_x & -\tilde{\xi}_y/(\rho c) \\ \tilde{\xi}_z c/\rho & \tilde{\xi}_y & -\tilde{\xi}_x & 0 & -\tilde{\xi}_z/(\rho c) \\ 0 & \tilde{\xi}_x & \tilde{\xi}_y & \tilde{\xi}_z & 1/(\rho c) \\ 0 & -\tilde{\xi}_x & -\tilde{\xi}_y & -\tilde{\xi}_z & 1/(\rho c) \end{pmatrix} \tag{3.55a}$$

$$\boldsymbol{P'} = \frac{c}{\rho} \begin{pmatrix} \tilde{\xi}_x \rho/c & \tilde{\xi}_y \rho/c & \tilde{\xi}_z \rho/c & \rho/(2c) & \rho/(2c) \\ 0 & \tilde{\xi}_z & -\tilde{\xi}_y & -\tilde{\xi}_x/2 & -\tilde{\xi}_x/2 \\ -\tilde{\xi}_z & 0 & \tilde{\xi}_x & -\tilde{\xi}_y/2 & -\tilde{\xi}_y/2 \\ \tilde{\xi}_y & -\tilde{\xi}_x & 0 & -\tilde{\xi}_z/2 & -\tilde{\xi}_z/2 \\ 0 & 0 & 0 & (\rho c)/2 & (\rho c)/2 \end{pmatrix} \tag{3.55b}$$

The primitive equations are recovered if Equation 3.54 is premultiplied by $\boldsymbol{P'}$ as:

$$\frac{\partial \boldsymbol{Q'}}{\partial t} + \boldsymbol{P'L} = \boldsymbol{P'S}_c, \tag{3.56}$$

and explicitly,

$$\frac{\partial \rho}{\partial t} + \tilde{\xi}_x L_1 + \tilde{\xi}_y L_2 + \tilde{\xi}_z L_3 + \frac{1}{2}(L_4 + L_5) = \tilde{\xi}_x S_{c1} + \tilde{\xi}_y S_{c2} + \tilde{\xi}_z S_{c3} + \frac{1}{2}(S_{c4} + S_{c5}) \tag{3.57a}$$

$$\frac{\partial u}{\partial t} - \tilde{\xi}_z L_2 + \tilde{\xi}_y L_3 + \frac{\tilde{\xi}_x}{2}(L_4 - L_5) = -\tilde{\xi}_z S_{c2} + \tilde{\xi}_y S_{c3} + \frac{\tilde{\xi}_x}{2}(S_{c4} - S_{c5}) \tag{3.57b}$$

$$\frac{\partial v}{\partial t} + \tilde{\xi}_z L_1 - \tilde{\xi}_x L_3 + \frac{\tilde{\xi}_y}{2}(L_4 - L_5) = \tilde{\xi}_z S_{c1} - \tilde{\xi}_x S_{c3} + \frac{\tilde{\xi}_y}{2}(S_{c4} - S_{c5}) \tag{3.57c}$$

$$\frac{\partial w}{\partial t} - \tilde{\xi}_y L_1 + \tilde{\xi}_x L_2 + \frac{\tilde{\xi}_z}{2}(L_4 - L_5) = -\tilde{\xi}_y S_{c1} + \tilde{\xi}_x S_{c2} + \frac{\tilde{\xi}_z}{2}(S_{c4} - S_{c5}) \tag{3.57d}$$

$$\frac{\partial p}{\partial t} + \frac{c^2}{2}(L_4 + L_5) = \frac{c^2}{2}(S_{c4} + S_{c5}) \tag{3.57e}$$

Additionally if Equations 3.57b, 3.57c and 3.57d are multiplied by $\tilde{\xi}_x$, $\tilde{\xi}_x$ and $\tilde{\xi}_z$ respectively and then combined the following expression for the normal velocity is obtained:

$$\frac{\partial \tilde{U}_\xi}{\partial t} + \frac{1}{2}(L_4 - L_5) = \frac{1}{2}(S_{c4} - S_{c5}). \tag{3.58}$$

The system of Equation 3.57 has been newly derived here and it has some differences with respect the one that can be found in [25, 28]. However equation Equation 3.57e and Equation 3.58 are still the same. As it will be seen in the following pages, the wall, and outflow boundary conditions mainly depend on these two equations, and the modification of the system should not affect in great manner the results obtained. In a personal communication with Kim, he explained that terms L_4 and L_5 are the more important ones concerning to reflections on the boundaries, an hence having used the mistaken set of equations of [25, 28] to derive the boundary conditions had not affected the final results in a great manner. In conclusion, the development of new boundary conditions is added to the future work list. Anyway, because the old ones have been used in every simulation done up to date, they will be described in the following subsections.

Now, focusing on the convection term $\boldsymbol{L}$, it is calculated at every time step during the calculation by an iterative process the steps of which are:

1. Fluxes in Equation 3.41 are evaluated using the finite difference techniques described in the previous sections and the normal-flux derivative $\partial\hat{\boldsymbol{E}}/\partial\xi$ is used as an initial guess to be corrected at the end of the iterative procedure.

2. The convection term $\boldsymbol{L}$ in Equation 3.53 is computed by the following expression:

$$\boldsymbol{L} = J\boldsymbol{P}^{-1}\left\{\frac{\partial\hat{\boldsymbol{E}}}{\partial\xi} - \left[\boldsymbol{E}\frac{\partial}{\partial\xi}\left(\frac{\xi_x}{J}\right) + \boldsymbol{F}\frac{\partial}{\partial\xi}\left(\frac{\xi_y}{J}\right) + \boldsymbol{G}\frac{\partial}{\partial\xi}\left(\frac{\xi_z}{J}\right)\right]\right\}. \tag{3.59}$$

3. Physical conditions, e.g. soft inflow, non reflecting outflow, wall, are then imposed at the boundary and the corrected characteristic convected term $\boldsymbol{L}^*$ is obtained.

4. The normal-flux derivative is then recomputed using the new corrected $\boldsymbol{L}^*$ in Equation 3.59 rearranged as:

$$\left(\frac{\partial\hat{\boldsymbol{E}}}{\partial\xi}\right)^* = \frac{1}{J}\boldsymbol{P}\boldsymbol{L}^* + \left[\boldsymbol{E}\frac{\partial}{\partial\xi}\left(\frac{\xi_x}{J}\right) + \boldsymbol{F}\frac{\partial}{\partial\xi}\left(\frac{\xi_y}{J}\right) + \boldsymbol{G}\frac{\partial}{\partial\xi}\left(\frac{\xi_z}{J}\right)\right], \tag{3.60}$$

   which is plugged again into Equation 3.41. The solution then is obtained by time integration of Equation 3.41.

To implement step 3 physical boundary conditions have to be met by the terms of $\boldsymbol{L}$ in Equation 3.57. Depending on the conditions required to the system of Equation 3.57 different physical boundary conditions can be achieved.

3.7.1 Soft Inflow Condition

For a subsonic inlet, only the L_5 characteristic wave can be directly obtained from the domain's interior information because it is the only leaving wave. For the rest of the waves they need to be prescribed using physical conditions. Kim and Lee [28] decided to impose the far upstream velocity and pressure, and considered quasi-isentropic conditions at the boundary. This conditions they expressed as

$$L_1^* = 0, \tag{3.61a}$$

$$L_2^* = K_{in} \left\{ \left[\tilde{\xi}_x(w - w_\infty) - \tilde{\xi}_z(u - u_\infty) \right] /2 \right\}, \tag{3.61b}$$

$$L_3^* = K_{in} \left\{ \left[-\tilde{\xi}_x(v - v_\infty) + \tilde{\xi}_y(u - u_\infty) \right] /2 \right\}, \tag{3.61c}$$

$$L_4^* = K_{in} \left[(\tilde{U} - \tilde{U}_\infty) + (p - p_\infty)/\rho c \right] = K_{in} \left[\tilde{\xi}_x(u - u_\infty) + \tilde{\xi}_y(v - v_\infty) \right] \tag{3.61d}$$

where K_{in} is a constant used to ensure a well-posed problem when pressure and velocity conditions are not close enough to those imposed in the far upstream. When this happens, non-physical reflections are created at the inlet boundary so the inlet velocity and pressure are forced to be close to the far upstream condition. The expression of K_{in} is

$$K_{in} = \sigma_{in}(1 - M_{max}^2)(c/l), \tag{3.62}$$

where σ_{in} is a coefficient that defines the inlet reflections, M_{max} is the maximum Mach number in the entire flow, c is the speed of sound, and l is the characteristic length of the domain. The value recommended in [28] was $\sigma_{in} = 0.25$. Additionally for viscous computations, the viscous stresses and heat flux gradients are set to zero in the boundary normal direction.

3.7.2 Nonreflecting Outflow Condition

For a subsonic outlet, in contrast with the inlet, only one wave cannot be obtained from the internal information, that is L_5. L_5 is the only characteristic wave entering the domain whereas all L_1, L_2, L_3 and L_4 are leaving it. Therefore an expression for the L_5 amplitude is needed at the boundary. If for example the pressure at the outlet is set to be equal to the far dowstream pressure, will lead to a well-posed problem that will however produce non-physical acoustic reflections.

Kim and Lee [28] imposed the value of the far downstream static pressure, and similarly to what done in the inlet, to avoid reflections a constant K_{out} is used to control the boundary reflectivity. The condition for the incoming wave is

$$L_5^* = K_{out} \left[(p - p_\infty)/\rho c \right], \tag{3.63}$$

with

$$K_{out} = \sigma_{out}(1 - M_{max}^2)(c/l), \tag{3.64}$$

where $\sigma_{out} = 0.25$ as in the inlet as suggested by Poinsot and Lele [42]. Again, if the flow is considered viscous, both tangential stresses and heat flux gradients in the boundary normal direction are set to zero.

3.7.3 Inviscid Wall Condition

An inviscid wall is that where no penetration is allowed, i.e. the fluid velocity is zero in the direction normal to the wall, but there is freedom of movement in the tangential plane, i.e. slip condition. Considering a flow travelling at a subsonic velocity from left to right, for a wall located at the left boundary the phase velocity signs indicate that L_5 is the wave transporting the information from the interior domain whereas L_4 transfers information from outside the solution domain. If the wall is located on the right boundary the opposite occurs with L_5 incoming and L_4 leaving the domain. Depending on the wall relative position to the flow velocity the amplitudes are given by

$$\text{(left wall)} \qquad L_4^* = L_5 + S_{C_4} - S_{C_5}, \tag{3.65a}$$

$$\text{(right wall)} \qquad L_5^* = L_4 - S_{C_4} + S_{C_5}. \tag{3.65b}$$

3.7.4 Viscous Wall Condition

In a viscous wall, as well as no penetration velocity, the tangential velocities are supposed to be zero too, i.e. non-slip condition. The amplitude of the characteristic waves then is given by

$$\text{(left wall)} \qquad L_4^* = L_5 + S_{C_4} - S_{C_5}, \tag{3.66a}$$

$$\text{(right wall)} \qquad L_5^* = L_4 - S_{C_4} + S_{C_5}, \tag{3.66b}$$

$$\text{(both sides)} \qquad \begin{cases} L_2^* = L_3^* = 0, \\ S_{C_2}^* = S_{C_3}^* = 0. \end{cases} \tag{3.66c}$$

It can be seen that the first two expressions are the same as if it was an inviscid wall. However the absence of tangential velocity results in Equation 3.66c. In this case however the viscous source term $\hat{\boldsymbol{S}}_v^*$ needs to be updated using the characteristic source term as

$$\hat{\boldsymbol{S}}_v^* = \frac{1}{J}\boldsymbol{P}\boldsymbol{S}_C^* + \left[\boldsymbol{E}\frac{\partial}{\partial \xi}\left(\frac{\xi_x}{J}\right) + \boldsymbol{F}\frac{\partial}{\partial \xi}\left(\frac{\xi_y}{J}\right) + \boldsymbol{G}\frac{\partial}{\partial \xi}\left(\frac{\xi_z}{J}\right) + \frac{\partial \hat{\boldsymbol{F}}}{\partial \eta} + \frac{\partial \hat{\boldsymbol{G}}}{\partial \zeta}\right]. \tag{3.67}$$

Equation 3.67 is solved for the viscous source term where the characteristic source term has been replaced by its updated version so the boundary conditions are satisfied.

The boundary conditions presented here are sufficient to define the Equation 3.41 at the boundaries for the tandem aerofoil case studied here for both viscous and inviscid computations. Nevertheless because of the Multi-block grid strategy used additional interface conditions need to be supplied so the information is communicated between adjacent blocks. This is covered in the next subsection.

3.7.5 Interface Boundary Conditions

As aforementioned, the inclusion of bodies in the computational domain usually lead to grid singularities that cause spurious oscillations that will end up contaminating the final solution. The grid singularities appear at points where the grid metric derivatives are not unique. This happens for example at both the leading and the trailing edge of the aerofoils of Figure 3.4. A close view of the leading edge zone is shown in Figure 3.6 where the blue lines represents the block boundaries. It is seen that four blocks meet at the leading edge of the aerofoil and that block 5 shares an block boundary with block 6 on its right and another one with block 0 at its bottom. The shared boundaries are referred as *block interface boundaries* herein. The block interface between block 5 and 6 is a constant ξ interface whereas the interface between block 5 and 0 is a constant η interface.

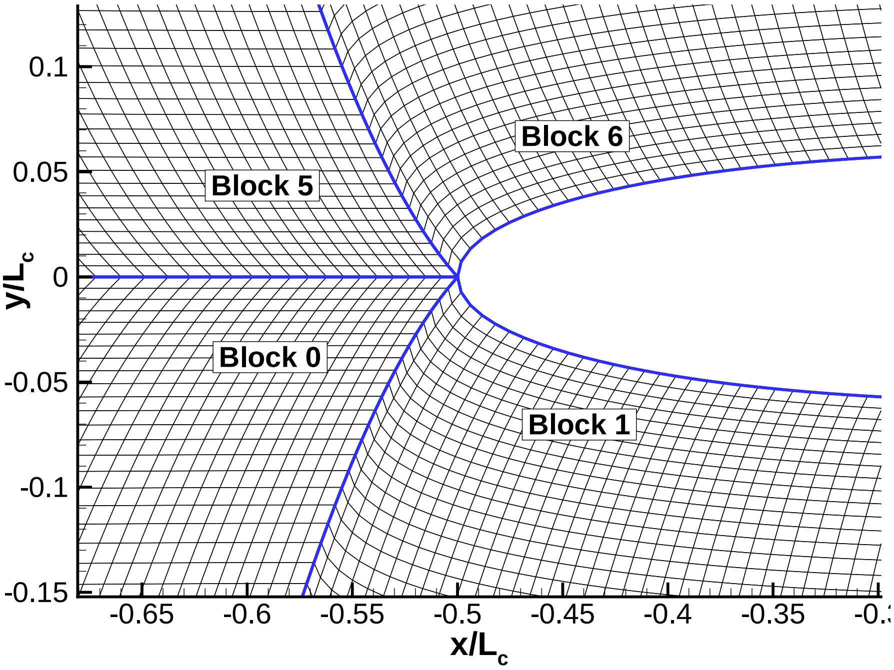

Figure 3.6: Leading Edge Zoomed View

Consider the interface of $\xi = $ const between block 5 and 6. To avoid the grid metrics discontinuity at this boundary the boundary scheme is used at the block boundaries. However this isolates the blocks not allowing the information to flow from one block to its neighbours. To let information flow between blocks an interface boundary condition has to be implemented. Now, the discontinuity can be expressed in terms of the metric gradient as $\nabla\xi^L \neq \nabla\xi^R$, i.e. the gradient on the left block does not match the gradient of the right block. This mismatch is in terms of the norm of the gradient but not in terms of its direction. Because both blocks share the same direction, the gradient in both blocks is always aligned with the normal direction of the $\xi = const$ boundary. That is

$$\frac{\nabla\xi^L}{|\nabla\xi^L|} = \nabla\tilde{\xi}^L, \quad \frac{\nabla\xi^R}{|\nabla\xi^R|} = \nabla\tilde{\xi}^R, \quad \nabla\tilde{\xi}^L = \nabla\tilde{\xi}^R. \tag{3.68}$$

In past subsections the characteristic wave equation in the boundary normal direction has been used to define several boundary conditions. Kim and Lee [29] cast the characteristic equation in the block interfaces where all variables and variables time derivatives must match. Consequently also the characteristic variables time derivative must also match at the interface.

$$\frac{\partial \boldsymbol{R}^L}{\partial t} = \frac{\partial \boldsymbol{R}^R}{\partial t}, \tag{3.69}$$

which leads to the following relation between left and right sided waves:

$$\boldsymbol{L}^L - \boldsymbol{S}_C^L = \boldsymbol{L}^R - \boldsymbol{S}_C^R \tag{3.70}$$

Again here the sign of the convection speeds will determine whether a wave is entering or exiting a block unit. However an incoming wave of one block will also be an exiting wave of its immediate adjacent block. This, on contrast to the other boundary conditions, means that both incoming and outgoing waves can be obtained from the interior values of the blocks. The method then consists in that every block calculates its outgoing waves form its own information whilst the incoming waves are corrected by the outgoing waves of its immediate block neighbour.

$$\text{for}\, m = 1, \cdots, 5 \begin{cases} L_m^{L^*} = L_m^R - S_{C_m}^R + S_{C_m}^L, & \text{if } \lambda_m^L/|\lambda_m^L| = \lambda_m^R/|\lambda_m^R| \leq 0 \\ \\ L_m^{R^*} = L_m^L - S_{C_m}^L + S_{C_m}^R, & \text{if } \lambda_m^L/|\lambda_m^L| = \lambda_m^R/|\lambda_m^R| \geq 0 \end{cases} \tag{3.71}$$

3.8 Sponge Zone

In Subsections 3.7.1 and 3.7.2 the inflow and outflow boundary conditions have been described. It has been highlighted the importance of avoiding flow reflections at the domain's boundaries. The *Soft Inflow* and the *Nonreflecting Outflow* conditions reduce the reflection level at the boundaries, however even with such boundary conditions reflections may appear. For these reason the code used for this study uses what known as *Sponge Zone* boundary conditions as well. The sponge zone can be seen as an artificial linear forcing/damping near the boundaries. For simplicity the Euler Equations Equation 3.6 will be used here for describing the implementation of the sponge zone. With Equation 3.6 in mind, the sponge zone treatment is represented by an additional term added to the equations at the right-hand side:

$$S_S = (\boldsymbol{Q} - \boldsymbol{Q_{ref}}) = \sigma(x,y) \begin{pmatrix} \rho - \rho_\infty \\ \rho u - \rho_\infty u_{gust} \\ \rho v - \rho_\infty v_{gust} \\ \rho w - \rho_\infty w_{gust} \\ \rho e_t - \rho_\infty e_{t_{gust}} \end{pmatrix},$$

$$\text{and: } e_{t_{gust}} = \frac{p_\infty}{(\gamma-1)\rho_\infty} + \frac{u_{gust}^2 + v_{gust}^2 + w_{gust}^2}{2}, \tag{3.72}$$

with:

$$\begin{gathered} \sigma(x,y) = \sigma_0\{1 + cos[\pi A(x) B(y)]\}/2, \\ x \in [x_{min}, x_{max}] \;\text{ and }\; y \in [y_{min}, y_{max}], \end{gathered} \tag{3.73}$$

and:

$$\begin{cases} A(x) = 1 - \max[1 - (x - x_{min}/L_S, 0] - \max[1 - (x_{max} - x)/Ls, 0], \\ B(y) = 1 - \max[1 - (y - y_{min}/L_S, 0] - \max[1 - (y_{max} - y)/Ls, 0], \end{cases} \tag{3.74}$$

where $\boldsymbol{Q}$ is the vector containing the flow variables, $\boldsymbol{Q_{ref}}$ (ρ_∞, $\rho_\infty u_{gust}$, $\rho_\infty v_{gust}$, $\rho_\infty w_{gust}$, and $\rho_\infty e_{t_{gust}}$) is the vector containing the desired reference solution aimed at the sponge zone, and σ is a free parameter known as sponge zone parameter that controls the strength of the forcing/damping in the sponge zone. The coefficient $\sigma(x, y)$ depends on the x and y position only, and consequently it is the same for each "z-plane". Equation 3.73 enables a smooth transition from the interior where the sponge zone is not present to the boundary where its effect is the biggest (σ_0). The initial value used for the work done here was $\sigma_0 = 8$. It is worth noting that all velocities, energy and pressure terms are followed by the "*gust*" subscript. This indicates that as well as being useful to control the reflection on the boundaries, the sponge zone can be used to introduce a certain flow profile at the sponge zone.

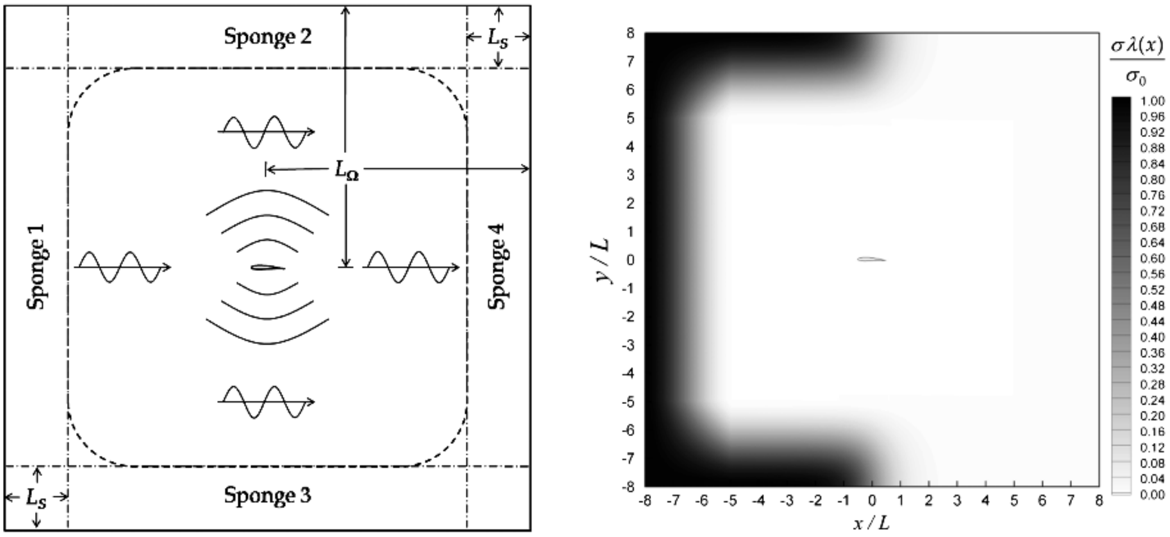

(a) Schematical Computational Domain Setup

(b) Sponge Zone Profile for Velocity Forcing

Figure 3.7: Sponge Zone Sketch and Profile Plot extracted from Kim et al. [31]

The sponge zone treatment used in this project is the one proposed by Kim et al. [31]. In Figure 3.7a one can see the location of the sponge zone close to the domain's boundaries and its geometric parameters L_Ω (distance from the domain's centre to the boundary limits) and L_S (sponge zone's thickness). Because the problem studied in this project is a tandem aerofoil case, the arrangement is not exactly the same, nonetheless Figure 3.7 will be enough to understand how the sponge is implemented in essence. The definition of the sponge source term proposed in [31] is

$$\boldsymbol{S}_S = \sigma(x,y)\begin{pmatrix} \rho - \rho_\infty \\ \lambda(x)(\rho u - \rho_\infty u_{gust}) \\ \lambda(x)(\rho v - \rho_\infty v_{gust}) \\ \lambda(x)(\rho w - \rho_\infty w_{gust}) \\ p - p_\infty \end{pmatrix}, \tag{3.75}$$

where the total energy has been substituted by the pressure since forcing applied on total energy overrides density and velocity. Additionally a weighting factor $\lambda(x)$ is introduced to modify the intensity of the sponge forcing depending on the streamwise direction. The weighting function is given by

$$\lambda(x) = (1-\varepsilon)[1-\tanh(x/L)]/2 + \varepsilon, \tag{3.76}$$

where ε is a constant representing the minimum desired value for λ, which in the case seen in Figure 3.7b and also in this project has been set to $\varepsilon = 0$ as suggested by Kim et al. [31] in order to avoid excessive constraint in the outflow condition.

3.9 Code Parallelisation

Nowadays High-Performance Computing clusters have become very popular among both industry and academia. Parallel computing is the key tool here which enables to have big jumps in computational efficiency by either sharing tasks or data between several computers. The in-house Fortran code has been parallelised using Message Passage Interface (MPI) libraries. MPI is a language-independent protocol by which the system will copy the program on to each node's processor where it will be executed independently. Unlike OMP, MPI encourages memory locality. This means that each processor will have its own private copy of each variable. There is no shared memory space, which means that if a variable allocated on some particular process is desired to be known by any other processor a communication between processors is needed.

As everything in life, this has an upside and a downside. On one hand, memory locality removes any chance of two processors trying to write to the same memory location at the same time, i.e. race conditions. On the other hand as mentioned above, communications between processors become capital in MPI. When two or more processors need to exchange information they need to 'speak' through the interconnect. Communications are synonym of overhead, and thus it is desirable to avoid them as much as possible.

Additionally, some would think that a code that runs in parallel among multiple threads will perform much faster than the serial code. This is only true if some considerations are taken into account. First of all, the code has to be designed in such a way that all the threads are doing useful work during execution time. No matter how many processors a program uses if they just sit there waiting to other processors to finish their individual tasks. A good analogy is viewing the team of processors as a cycling team on a time trial race. In this scenario the time of the team is determined by the slowest member of the team. So a good way to reduce the time is to distribute the effort as equal as possible between all the team mates so they all finish the race in good shape. Following this analogy, if we overload a particular thread/cyclist it will take more time to finish and then the overall performance of the team will decrease. This is commonly known as load balancing, and a good parallel programmer should distribute the effort evenly between all threads.

A common strategy when dealing with grid based problems, as it is the case here, is to split the domain as evenly as possible among the available processors. In a perfect world this should solve the problem supposing that once the data has been distributed among the processors, the problem can be then solved independently at every processor. However in real world if the grid is just split and distributed among the processors the information is confined inside every subdomain without any communication between subdomains. In Section 3.7 it has been shown that waves carrying information should be able to cross any internal (artificial) boundaries so information is convected from inlet to outlet and vice versa.

A possible solution that enables information to be exchanged between adjacent subdomains is the use of *halo points*. This points are points at which all communication between subdomains happens. Kim and Sandberg [30] parallelised a system of compact differencing and filtering of [21, 22] using three halo points for the differencing scheme and a predictor-corrector method for the filtering scheme. A similar one-sided compact finite difference schemes of [21] where used, however the extrapolating function parameters where determined from interior as well as the halo points. As in [21] the control variables where used to optimise the scheme in the wavenumber domain. Although the work of Kim and Sandberg [30] meant a great advantage with respect to previous work done by other researchers using overlapped subdomains [47], still, parallel artifacts arose from the subdomain boundaries for vortex-driven flows.

In a more recent piece of work, Kim [23] presents a new set of both differencing and filtering *subdomain boundary* (SB) schemes. The starting point was again the Optimised High-Order Compact finite difference schemes and filters of [21, 22] (see Equations 3.14, 3.25, 3.29, and 3.32). The system of equations formed by the difference and the filtering schemes expressed in matrix-vector form is:

$$\text{Differencing System:} \qquad \boldsymbol{P}\bar{\boldsymbol{f}}' = \frac{1}{\Delta x}\boldsymbol{Q}\boldsymbol{f}, \tag{3.77a}$$

$$\text{Filtering System:} \qquad \boldsymbol{P}_F\hat{\Delta}\boldsymbol{f} = \boldsymbol{Q}_F\boldsymbol{f}, \tag{3.77b}$$

where $\boldsymbol{f}$, $\bar{\boldsymbol{f}}'$, and $\hat{\Delta}\boldsymbol{f}$ are the objective function, numerical derivative, and filter's contribution nodal values respectively. The matrices $\boldsymbol{P}$, $\boldsymbol{P}_F$, $\boldsymbol{Q}$, and $\boldsymbol{Q}_F$ are the coefficient matrices for differencing and filtering respectively with the subscript F standing for filter matrices. Because the process used in [23] is quite similar for the parallelisation of both the filtering and the differencing system, just the latter is shown here as an illustrative example.

$$\boldsymbol{P} = \begin{pmatrix} 1 & \gamma_{01} & \gamma_{02} & 0 & \cdots & \cdots & \cdots & \cdots & 0 \\ \gamma_{10} & 1 & \gamma_{12} & \gamma_{13} & 0 & \cdots & \cdots & \cdots & 0 \\ \gamma_{20} & \gamma_{21} & 1 & \gamma_{23} & \gamma_{24} & 0 & \cdots & \cdots & 0 \\ 0 & \beta & \alpha & 1 & \alpha & \beta & 0 & \cdots & 0 \\ \vdots & \ddots & \ddots & \ddots & \ddots & \ddots & \ddots & \ddots & \vdots \\ 0 & \cdots & 0 & \beta & \alpha & 1 & \alpha & \beta & 0 \\ 0 & \cdots & \cdots & 0 & \gamma_{24} & \gamma_{23} & 1 & \gamma_{21} & \gamma_{20} \\ 0 & \cdots & \cdots & \cdots & 0 & \gamma_{13} & \gamma_{12} & 1 & \gamma_{10} \\ 0 & \cdots & \cdots & \cdots & \cdots & 0 & \gamma_{01} & \gamma_{02} & 1 \end{pmatrix} \tag{3.78}$$

$$\boldsymbol{Q} = \begin{pmatrix} b_{00} & b_{01} & b_{02} & b_{03} & b_{04} & b_{05} & b_{06} & 0 & \cdots & \cdots & 0 \\ b_{10} & b_{11} & b_{12} & b_{13} & b_{14} & b_{15} & b_{16} & 0 & \cdots & \cdots & 0 \\ b_{20} & b_{21} & b_{22} & b_{23} & b_{24} & b_{25} & b_{26} & 0 & \cdots & \cdots & 0 \\ -a_3 & -a_2 & -a_1 & 0 & a_1 & a_2 & a_3 & 0 & \cdots & \cdots & 0 \\ 0 & -a_3 & -a_2 & -a_1 & 0 & a_1 & a_2 & a_3 & 0 & \cdots & 0 \\ \vdots & \ddots & \ddots & \ddots & \ddots & \ddots & \ddots & \ddots & \ddots & \ddots & \vdots \\ 0 & \cdots & 0 & -a_3 & -a_2 & -a_1 & 0 & a_1 & a_2 & a_3 & 0 \\ 0 & \cdots & \cdots & 0 & -a_3 & -a_2 & -a_1 & 0 & a_1 & a_2 & a_3 \\ 0 & \cdots & \cdots & 0 & -b_{26} & -b_{25} & -b_{24} & -b_{23} & -b_{22} & -b_{21} & -b_{20} \\ 0 & \cdots & \cdots & 0 & -b_{16} & -b_{15} & -b_{14} & -b_{13} & -b_{12} & -b_{11} & -b_{10} \\ 0 & \cdots & \cdots & 0 & -b_{06} & -b_{05} & -b_{04} & -b_{03} & -b_{02} & -b_{01} & -b_{00} \end{pmatrix} \tag{3.79}$$

$$\boldsymbol{R} = \left(\begin{array}{c|c} \boldsymbol{R}_A & \boldsymbol{0} \\ \hline \boldsymbol{0} & \boldsymbol{R}_B \end{array}\right) = \\ = \left(\begin{array}{cccccccc|cccccccc} 1 & \gamma_{01} & \gamma_{02} & 0 & \cdots & \cdots & \cdots & \cdots & \cdots & \cdots & \cdots & \cdots & \cdots & \cdots & \cdots & 0 \\ \gamma_{10} & 1 & \gamma_{12} & \gamma_{13} & 0 & \cdots & \cdots & \cdots & \cdots & \cdots & \cdots & \cdots & \cdots & \cdots & \cdots & 0 \\ \gamma_{20} & \gamma 21 & 1 & \gamma_{23} & \gamma_{24} & 0 & \cdots & \cdots & \cdots & \cdots & \cdots & \cdots & \cdots & \cdots & \cdots & 0 \\ 0 & \beta & \alpha & 1 & \alpha & \beta & 0 & \cdots & \cdots & \cdots & \cdots & \cdots & \cdots & \cdots & \cdots & 0 \\ \vdots & \ddots & \ddots & \ddots & \ddots & \ddots & \ddots & \ddots & \ddots & \ddots & \ddots & \ddots & \ddots & \ddots & \ddots & \vdots \\ 0 & \cdots & 0 & \beta & \alpha & 1 & \alpha & \beta & 0 & \cdots & \cdots & \cdots & \cdots & \cdots & \cdots & 0 \\ 0 & \cdots & \cdots & 0 & \beta & \alpha & 1 & \alpha & 0 & 0 & \cdots & \cdots & \cdots & \cdots & \cdots & 0 \\ 0 & \cdots & \cdots & \cdots & 0 & \beta & \alpha & 1 & 0 & 0 & 0 & \cdots & \cdots & \cdots & \cdots & 0 \\ \hline 0 & \cdots & \cdots & \cdots & \cdots & 0 & 0 & 0 & 1 & \alpha & \beta & 0 & \cdots & \cdots & \cdots & 0 \\ 0 & \cdots & \cdots & \cdots & \cdots & \cdots & 0 & 0 & \alpha & 1 & \alpha & \beta & 0 & \cdots & \cdots & 0 \\ 0 & \cdots & \cdots & \cdots & \cdots & \cdots & \cdots & 0 & \beta & \alpha & 1 & \alpha & \beta & 0 & \cdots & 0 \\ \vdots & \ddots & \ddots & \ddots & \ddots & \ddots & \ddots & \ddots & \ddots & \ddots & \ddots & \ddots & \ddots & \ddots & \ddots & \vdots \\ 0 & \cdots & \cdots & \cdots & \cdots & \cdots & \cdots & \cdots & \cdots & 0 & \beta & \alpha & 1 & \alpha & \beta & 0 \\ 0 & \cdots & \cdots & \cdots & \cdots & \cdots & \cdots & \cdots & \cdots & \cdots & 0 & \gamma_{24} & \gamma_{23} & 1 & \gamma_{21} & \gamma_{20} \\ 0 & \cdots & \cdots & \cdots & \cdots & \cdots & \cdots & \cdots & \cdots & \cdots & \cdots & 0 & \gamma_{13} & \gamma_{12} & 1 & \gamma_{10} \\ 0 & \cdots & \cdots & \cdots & \cdots & \cdots & \cdots & \cdots & \cdots & \cdots & \cdots & \cdots & 0 & \gamma_{02} & \gamma_{01} & 1 \end{array}\right) \tag{3.80}$$

For explanatory purposes, lets consider a computational domain which is split into two smaller subdomains at is centre so each subdomain contains $M = (N-1)/2$ elements where $N+1$ is the total number of elements. The left subdomain is referred as Subdomain A and the right as Subdomain B. To be able to perform independent computations in each subdomain the pentadiagonal matrix $\boldsymbol{P}$ needs to substitute some of the off-diagonal elements by zero so it can be independently inverted for each subdomain. The resulting matrix is $\boldsymbol{R}$ (see Equation 3.80). If Equation 3.77a is premultiplied by $\boldsymbol{R}\boldsymbol{P}^{-1}$ the following relations are obtained:

$$\boldsymbol{R}\bar{\boldsymbol{f}}' = \frac{1}{\Delta x}\boldsymbol{R}\boldsymbol{P}^{-1}\boldsymbol{Q}\boldsymbol{f} = \frac{1}{\Delta x}\boldsymbol{S}\boldsymbol{f}, \tag{3.81}$$

where $\boldsymbol{S} = \boldsymbol{R}\boldsymbol{P}^{-1}\boldsymbol{Q}$ is a matrix that is at the same time formed by four submatrices $\boldsymbol{S}_A$, $\boldsymbol{T}_A$, $\boldsymbol{S}_B$, and $\boldsymbol{T}_B$ (subscript indicates different subdomains) as:

$$\boldsymbol{S} = \left(\begin{array}{c|c} \boldsymbol{S}_A & \boldsymbol{T}_B \\ \hline \boldsymbol{T}_A & \boldsymbol{S}_B \end{array}\right), \tag{3.82}$$

which leads to the following quasi-disjoint system of equations:

$$\boldsymbol{R}_A\bar{\boldsymbol{f}}'_A = \frac{1}{\Delta x}(\boldsymbol{S}_A\boldsymbol{f}_A + \boldsymbol{T}_B\boldsymbol{f}_B), \tag{3.83a}$$

$$\boldsymbol{R}_B\bar{\boldsymbol{f}}'_B = \frac{1}{\Delta x}(\boldsymbol{S}_B\boldsymbol{f}_B + \boldsymbol{T}_A\boldsymbol{f}_A). \tag{3.83b}$$

The vectors $\boldsymbol{f}_A$, $\boldsymbol{f}_B$, $\bar{\boldsymbol{f}}'_A$, and $\bar{\boldsymbol{f}}'_B$ represent the subdomain-wise associated elements of the original vectors $\boldsymbol{f}$ and $\bar{\boldsymbol{f}}'$ and the matrices $\boldsymbol{S}_A$, $\boldsymbol{T}_A$, $\boldsymbol{S}_B$, and $\boldsymbol{T}_B$ are as shown in Equation 3.84

$$\boldsymbol{S}_A = \begin{pmatrix} b_{00} & b_{01} & b_{02} & b_{03} & b_{04} & b_{05} & b_{06} & 0 & \cdots & \cdots & 0 \\ b_{10} & b_{11} & b_{12} & b_{13} & b_{14} & b_{15} & b_{16} & 0 & \cdots & \cdots & 0 \\ b_{20} & b_{21} & b_{22} & b_{23} & b_{24} & b_{25} & b_{26} & 0 & \cdots & \cdots & 0 \\ -a_3 & -a_2 & -a_1 & 0 & a_1 & a_2 & a_3 & 0 & \cdots & \cdots & 0 \\ 0 & -a_3 & -a_2 & -a_1 & 0 & a_1 & a_2 & a_3 & 0 & \cdots & 0 \\ \vdots & \ddots & \ddots & \ddots & \ddots & \ddots & \ddots & \ddots & \ddots & \ddots & \vdots \\ 0 & \cdots & 0 & -a_3 & -a_2 & -a_1 & 0 & a_1 & a_2 & a_3 & 0 \\ 0 & \cdots & \cdots & 0 & -a_3 & -a_2 & -a_1 & 0 & a_1 & a_2 & a_3 \\ 0 & \cdots & \cdots & \cdots & 0 & -a_3 & -a_2 & -a_1 & 0 & a_1 & a_1 \\ -c_{1M} & \cdots & \cdots & \cdots & -c_{16} & -c_{15} & -c_{14} & -c_{13} & -c_{12} & -c_{11} & -c_{10} \\ -c_{0M} & \cdots & \cdots & \cdots & -c_{16} & -c_{05} & -c_{04} & -c_{03} & -c_{02} & -c_{01} & -c_{00} \end{pmatrix} \tag{3.84a}$$

$$\boldsymbol{T}_B = \begin{pmatrix} 0 & \cdots & \cdots & \cdots & \cdots & 0 \\ \vdots & \ddots & \ddots & \ddots & \ddots & \vdots \\ a_3 & 0 & \cdots & \cdots & \cdots & 0 \\ -c^*_{10} & -c^*_{11} & -c^*_{12} & -c^*_{13} & \cdots & -c^*_{1M} \\ -c^*_{00} & -c^*_{01} & -c^*_{02} & -c^*_{03} & \cdots & -c^*_{0M} \end{pmatrix} \tag{3.84b}$$

$$\left.\begin{array}{l} (\boldsymbol{S}_B)_{l,m} = -(\boldsymbol{S}_A)_{M-l,M-m} \\ (\boldsymbol{T}_A)_{l,m} = -(\boldsymbol{T}_B)_{M-l,M-m} \end{array}\right\} \quad \text{for} \left\{ \begin{array}{c} l = 0, \cdots, M \\ m = 0, \cdots, M \end{array} \right\} \quad \text{with } M = \frac{N-1}{2} \tag{3.84c}$$

In Equation 3.84 one can observe that only two rows at the bottom representing the nearest two points to the subdomain interface have been modified with respect to the original formulation, i.e. the rows containing c_{0m}, c_{1m}, c^*_{0m} and c^*_{1m}, where the star represents values obtained from the adjacent subdomain. Based on the above matrices, the compact differencing scheme at the subdomain boundaries becomes:

$$\begin{aligned}
&\bar{f}'_i + \alpha \bar{f}'_{i\pm1} + \beta \bar{f}'_{i\pm2} = \pm\frac{1}{\Delta x}\left(\sum_{m=0}^{M} c_{0m} f_{i\pm m} + h_0\right), \\
&\alpha \bar{f}'_i + \bar{f}'_{i\pm1} + \alpha \bar{f}'_{i\pm2} + \beta \bar{f}'_{i\pm3} = \pm\frac{1}{\Delta x}\left(\sum_{m=0}^{M} c_{1m} f_{i\pm m} + h_1\right), \\
&\beta \bar{f}'_i + \alpha \bar{f}'_{i\pm1} + \bar{f}'_{i\pm2} + \alpha \bar{f}'_{i\pm3} + \beta \bar{f}'_{i\pm4} = \pm\frac{1}{\Delta x}\left[\sum_{m=1}^{2} a_m (f_{i\pm2\pm m} - f_{i\pm2\pm m}) + a_3 (f_{i\pm5} - h_2)\right],
\end{aligned} \tag{3.85}$$

where $i = 0$ or $i = N_S$ for each subdomain defined by $i \in [0, N_S \geq M]$. The terms h_0, h_1 and h_2 are halo terms which are calculated with information owned by a single subdomain but which are used in the adjacent domains. The values of them are given by:

$$\left.\begin{aligned}
&(h_0, h_1) = \sum_{m=0}^{M} (c^*_{0m}, c^*_{1m}) f^*_{l\pm m} \\
&h_2 = f^*_l
\end{aligned}\right\} \quad \text{with } l = \begin{cases} N^*_S \\ 0 \end{cases} \quad \text{for } i = \begin{cases} 0 \\ N_S \end{cases} \tag{3.86}$$

The differencing scheme has been used here for explaining Kim's [23] method, nevertheless all of the beforehand mention also applies to the derivation of the SB compact filtering scheme with minor differences (see [23] for further information).

Up to here Equation 3.83 is just the result of a lineal-algebraic transformation and hence the results obtained are the same that those of a serial implementation. However the stencil size could become extremely large if if the entire rows of "c" coefficients are used, i.e. $M = N_S$. At the same time if M is reduced too much the SB scheme largely deviates from its serial version and spurious fluctuations appear at the subdomain interfaces. As the ideal case is that when the parallel scheme leads to the same results as the serial scheme, Kim [23] transforms the new SB scheme to the wavenumber domain form where it compares its resolution with the interior scheme by computing a L_2-norm based deviation from the original scheme. A plot of the deviation versus the stencil size M [23, Fig. 6] shows that if the deviation is wanted to be always below 3% the size of the stencil has to be at least $M = 11$ for the differencing scheme and $M_F = 8$ for the filtering scheme.

3.10 Parallel Scalability

In this section the scalability of the code is presented. The study was performed using University of Southampton's cluster *Iridis4*. The problem size was kept constant in all cases, and computational time was measured for different number of processors used. The time measured does not include I/O actions. Because of the nature of the code, at least 12 processors need to be used, since that is the minimum number of blocks used when simulating a single element aerofoil. For that case columns 2 and 3 are chopped off the grid shown in Figure 4.16. The problem size was fixed to 30.72 millions of points and the maximum number of cores used was 384. In order to measure the scalability and the efficiency of the code both Speed-Up S_u and Parallel efficiency P_{eff} were measured. The definition of these is found in Equation 3.87 where T_s is the simulation time, T_w is the wall time, and n_p is the number of processors used. The results obtained can be seen in Table 3.4.

$$S_u = \frac{[T_w/T_s]_{12}}{[T_w/T_s]_{n_p}} \tag{3.87a}$$

$$P_{eff} = \frac{S_u}{n_p/12} \tag{3.87b}$$

Figure 3.8 shows that the code scales well, being even better than the linear scalability, i.e. doubling the number of cores halves the time needed. This is due to the size of the problem being too big for the case of 12 processors, i.e. the memory needed is bigger than the cache memory, which is the fastest memory, and hence there is more likelihood of *cache missing*. It is worth noticing that when using 384 processors nearly just an hour is needed of wall time is needed per non-dimensional time unit of simulation time.

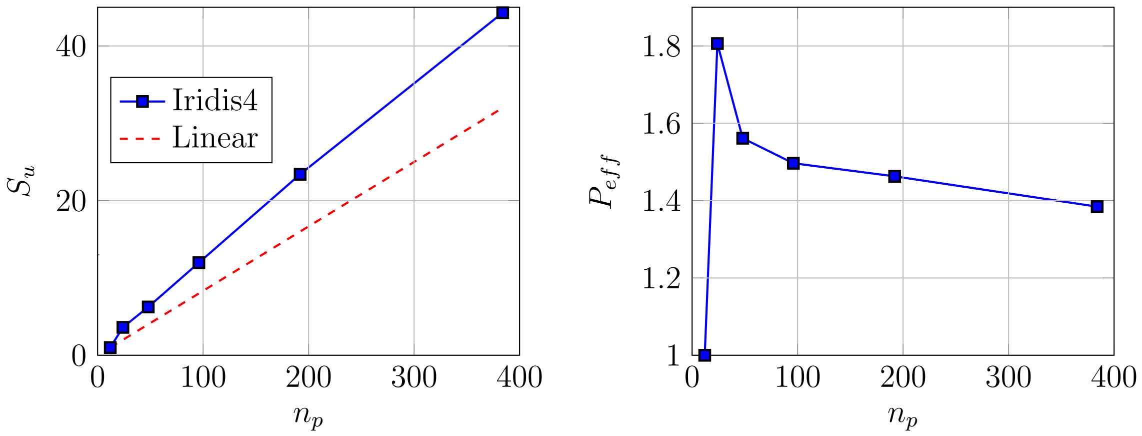

(a) Speed-Up

(b) Parallel Efficiency

Figure 3.8: Scalability Tests

Table 3.4: Scalability Test Data

n_p	T_w[s]	T_s[Time Unit]	T_w/T_s[h/Time Unit]	S_u	Linear S_u	P_{eff}
12	1.73E+004	0.1	48.089	1.000	1	1.000
24	4.79E+003	0.1	13.312	3.613	2	1.806
48	2.77E+003	0.1	7.700	6.245	4	1.561
96	1.45E+003	0.1	4.016	11.973	8	1.497
192	7.40E+002	0.1	2.055	23.405	16	1.463
384	3.91E+002	0.1	1.085	44.301	32	1.384

3.11 Time Discretisation

Up to here spatial discretisation has been extensively described in the last sections but it must be recalled that Equation 3.7 represents the Unsteady three-dimensional Navier-Stokes equations in vector form and consequently a time marching scheme is needed for their solution. Fourth order compact finite difference schemes and sixth order filters have been widely used in combination with an explicit fourth order Runge-Kutta [21–23, 26–28, 30] time advancing method with successful results. The Runge-Kutta (R-K) method used for time advancing in this numerical investigation is a multi-stage method, i.e. the time step integration is done with intermediate stages. The method can be expressed as:

$$\text{for } \frac{\partial \boldsymbol{Q}}{\partial t} = \boldsymbol{F}(\boldsymbol{Q}, t) \begin{cases} \boldsymbol{Q}^{n_1} = \boldsymbol{Q}^{n} + \dfrac{\Delta t}{4}\boldsymbol{F}(\boldsymbol{Q}^{n}, t), \\ \boldsymbol{Q}^{n_2} = \boldsymbol{Q}^{n} + \dfrac{\Delta t}{3}\boldsymbol{F}(\boldsymbol{Q}^{n_1}, t), \\ \boldsymbol{Q}^{n_3} = \boldsymbol{Q}^{n} + \dfrac{\Delta t}{2}\boldsymbol{F}(\boldsymbol{Q}^{n_2}, t), \\ \boldsymbol{Q}^{n+1} = \boldsymbol{Q}^{n} + \dfrac{\Delta t}{1}\boldsymbol{F}(\boldsymbol{Q}^{n_3}, t), \end{cases} \tag{3.88}$$

where $\boldsymbol{Q}$ is the vector containing the variables and $\boldsymbol{F}$ represents the fluxes sum, which is both a function of $\boldsymbol{Q}$ and time t, and Δt is the time-step. The four stages are represented in Equation 3.88 where the initial solution is given at the time level n and the new update at time level $n+1$. Intermediate contributions are given at time stages n_1, n_2, and n_3.

Because this formulation is explicit, i.e. the solution at the actual time level Q^{n+1} does not appear on the RHS of Equation 3.88, an special care has to be taken with the value of the time step to maintain the numerical method stable. The stability of the method is given by the Courant-Friedrichs-Levy (CFL) condition which in terms of the characteristic velocities is:

$$CFL = \Delta t U_\xi + \Delta t U_\eta + \Delta t U_\zeta \leq 1. \tag{3.89}$$

U_ξ, U_η, and U_ζ are the characteristic wave's convection velocities in the three computational directions ξ, η and ζ. This expressions means that information is not allowed to cross more than one cell per time-step, otherwise the system will become unstable.

3.12 Geometry Definition

The geometry that defines the WLE tandem aerofoil is shown in Figure 3.9. The two aerofoils are based on a NACA0012 section. The chord of the fore element (L_{c1}) is constant along the span and the aft element's chord (L_{c2}) varies with a sinusoidal profile. The mean chord length for the aft element is equal to the fore element's chord length. Additionally each section of the aft element retains the original NACA0012 section. The amplitude of the WLEs is defined by h_{LE} and its wavelength by λ_{LE}. The ratio between the amplitude and the wavelength is defined as

$$\theta = \frac{h_{LE}}{\lambda_{LE}}, \tag{3.90}$$

and will be referred as WLE sweep angle, or simply sweep angle herein. Strictly speaking the angle should be $\theta_{real} = \arctan^{-1}\left(\lambda_{LE}/4h_{LE}\right)$, which would give the angle of the WLE's peaks viewed from the top. Nonetheless for simplicity Equation 3.90 will be used. These are hence the WLE related parameters.

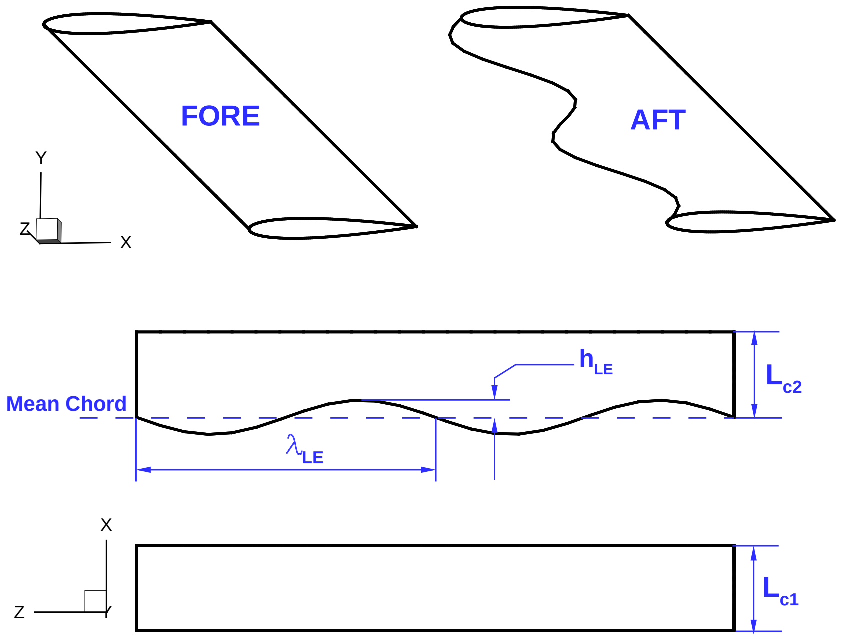

Figure 3.9: Wavy Leading Edge parameters

The tandem parameters have already been defined in Figure 2.1, which for completeness is recovered here in Figure 3.10. Both Figure 3.9 and 3.10 define the geometrical parameters of the Tandem WLE configuration (TWLE).

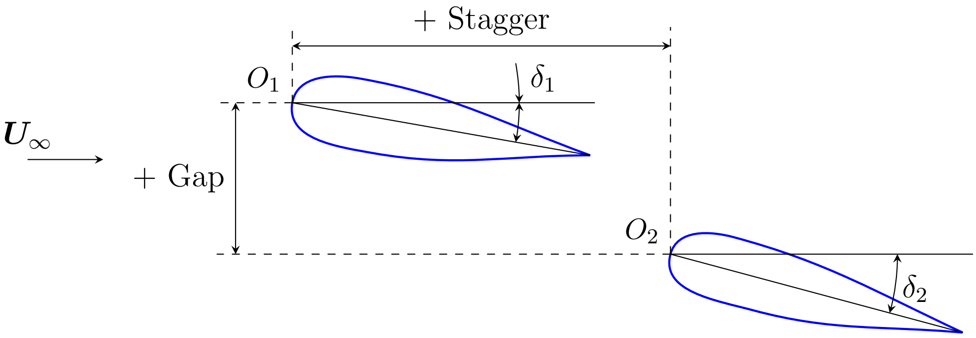

Figure 3.10: Tandem Configuration Parameters

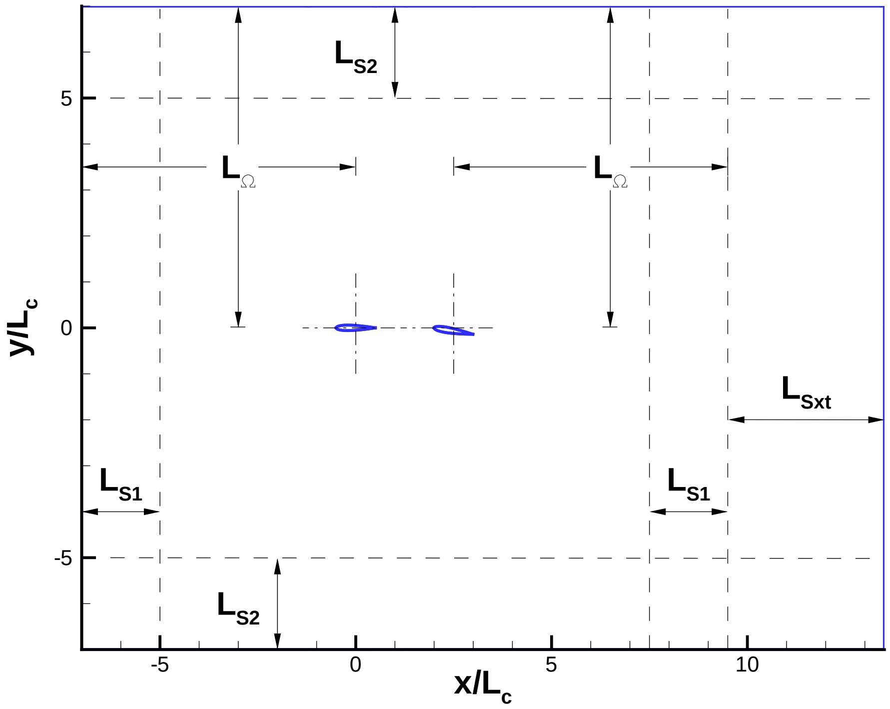

Figure 3.11: Domain Sketch with the most important parameters

In Figure 3.11 one can also see the main parameters defining the geometry of the computational domain. These parameters are the domain size L_Ω, the horizontal sponge thickness L_{S1}, the vertical sponge thickness L_{S2}, and the extra sponge thickness L_{Sxt}. The sponge thicknesses have been kept constant throughout all simulations carried out to date, and their values can be found in Table 3.5.

Table 3.5: Sponge Thicknesses

Sponge Thickness	Value
L_{S1}	$2L_c$
L_{S2}	$2L_c$
L_{Sxt}	$4L_c$

Chapter 4

Verification and Validation

4.1 Introduction

In first place it is necessary to state that the whole of the simulations carried out so far have been done using the Euler equations (see Equation 3.6). The reason for this is that the numerical schemes used for solving those equations are the same as for the Navier-Stokes equations but the cost of the simulations is much smaller. Consequently, during the development stage, which is the one undergoing at the moment, the Euler equations are the best for testing the brand new developed grid structures for double element configurations without the requirement of massive computational environments and long waiting intervals. Now, once that has been stated, the AIAA defines verification and validation as [1]:

Verification: the process of determining that a model implementation accurately represents the developer's conceptual description of the model and the solution to the model.

Validation: the process of determining the degree to which a model is an accurate representation of the real world from the perspective of the intended uses of the model.

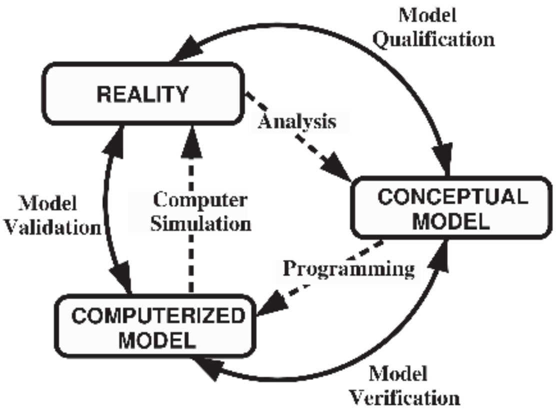

Figure 4.1: Verification and Validation diagram [36]

Figure 4.1 represents the verification and validation process as described by Oberkampf and Trucano [36]. By observation of Figure 4.1 the process of verification can be related to the process of checking that the computerised model faithfully represents the conceptual model which in the case of Computational Fluid Mechanics are the Navier-Stokes equations Equation 3.1. On the other hand validation is related to the linkage between the computerised model or code with the real world.

The circle is also closed by the *Qualification* process which the Society of Computer Simulation defines as: "Determination of adequacy of the conceptual model to provide an acceptable level of agreement for the domain of intended application". This is understood as if the model (the set of PDEs) are the best approximation of the reality. Both qualification and validation are more rooted in the question of how accurate is the solution in the physical sense whereas verification is more rooted in the question of how accurate is the solution in the mathematical sense.

In terms of verification, the real problem is given in a continuous media as it is the air surrounding the pair of aerofoils. However the PDEs are solved by a discrete method (Finite Difference Technique) which approximates the real continuous solution. The use of infinite elements in the discretisation would lead to a perfect solution, nevertheless this will be extremely computationally expensive. Consequently the grid needs to be fine enough so the solutions are not affected by the discretisation errors while still being computationally efficient. A grid dependency study can show that the errors decrease with increasing number of points. Similarly, the real problem happens in an almost unbounded domain whereas the computational model must be defined by a finite bounded region. The domain needs to be as well big enough so the far upstream and dowstream conditions are met. Nonetheless, similarly to what happens in wind tunnel experiments if the walls of the testing section are too close to the model under investigation, i.e. too high *Blockage ratio*, if the boundaries of the computational domain are located too close to the model of investigation the flow can be affected by the flow conditions imposed at the boundaries. The domain dependency tests are used to verify this.

4.2 Inviscid Validation

For the inviscid validation, because the Euler equations have been used in the development stage due to the fact that computations are much less expensive than Navier-Stokes computations, results are compared to an inviscid-irrotational panel method based on constant strength sources and vortices [12]. Because the original version of the code was oriented to single element aerofoils, the code had to be updated using the method of Chaves [3].

Because the panel method used does not include compressibility effects, for comparison with the Euler's code it is necessary to apply some correction to the results. The following rule can be used to transform from incompressible to compressible results

$$C_p = \frac{C_{p_I}}{\beta} \qquad \text{with } \beta = \sqrt{1 - M_\infty^2} \tag{4.1}$$

which is known as the Prandtl-Glauer rule, where C_{p_I} is the incompressible value, β is the Prandtl-Glauert coefficient and M_∞ is the free-stream Mach number. Notice here that the Mach number used here to obtain the transformed results is the free-stream Mach number. This can imply that transformed results may still differ from the Euler's code results at critical locations such as the leading and trailing edge, as well as the location of the suction side pressure peak [55]. Woodward [55] proved that transformations using the local Mach number at the surface would lead to much better results.

4.2.1 Grid Dependency Tests

The consistency of the results with regards the grid resolution where tested using three different grids with coarse, medium, and fine resolutions respectively. The number of points used per block can be seen in Table 4.1, 4.2, and 4.3 where only bottom blocks' number of points are shown since the top row has the same configuration.

Table 4.1: Number of Points per Block for the Coarse Grid

	Block No.				
Direction	0	1	2	3	4
ξ	100	50	50	50	100
η	100	100	100	100	100
ζ	15	15	15	15	15

Table 4.2: Number of Points per Block for the Medium (baseline) Grid

	Block No.				
Direction	0	1	2	3	4
ξ	200	100	100	100	200
η	200	200	200	200	200
ζ	15	15	15	15	15

Table 4.3: Number of Points per Block for the Fine Grid

	Block No.				
Direction	0	1	2	3	4
ξ	400	200	150	200	400
η	400	400	400	400	400
ζ	15	15	15	15	15

The results obtained from this simulations are showed in Figure 4.2 in the form of pressure coefficient distributions over the aerofoils. It seems that for the solving the Euler equations the coarse grid would be enough, however since the final aim is to switch to the Navier-Stokes equations as soon as the development stage is finished, it was worth trying finer grid resolutions because when viscosity effects are account, the length scales of the flow that the LES method aims to solve become really small.

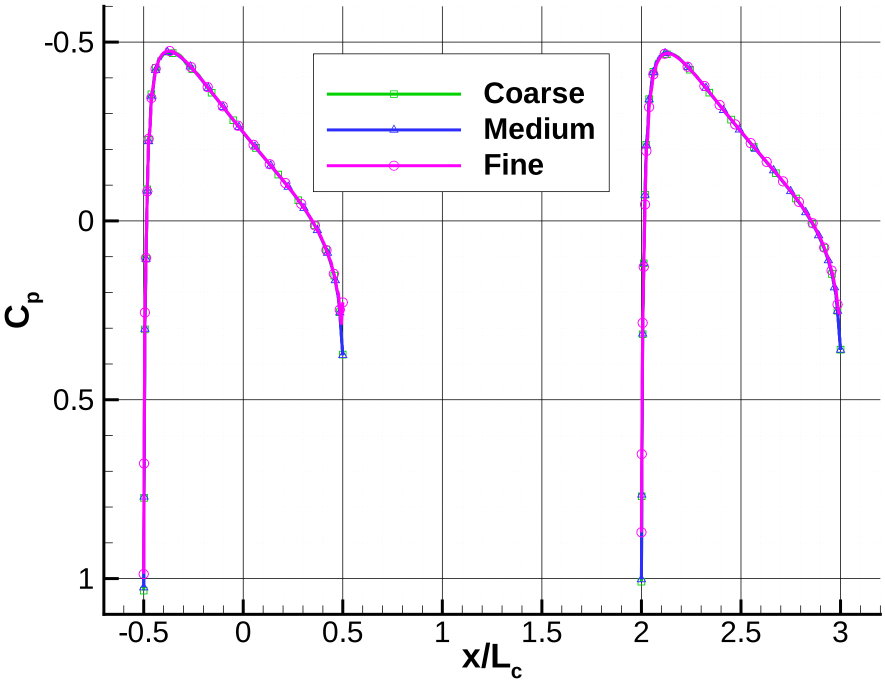

Figure 4.2: C_p comparison for three different grid resolutions at zero AoA, where "C" means coarse resolution grid, "M" means medium resolution grid and "F" means fine resolution grid.

4.2.2 Domain Dependency Tests

In this section the effect of the domain size over the final solution is tested. The domain sizes used ranged between 5 and 11 chord lengths and pressure coefficient distributions are measured over the two elements of the tandem configuration. Results of the study are compared with values obtained from the potential code with compressibility corrections. Figure 4.3 shows how results seem to be quite similar for both elements at different domain sizes L_Ω. However a close look at the first element trailing edge reveals that the domain size has a direct impact in the determination of the leading edge pressure peak as Figure 4.4 shows. It seems that longer domain sizes better agree with the panel method results. This behaviour had been observed earlier by Kim et al. [31], who related the effect of this pressure peak differences with the sponge zone. Nevertheless the level of agreement with the panel code is high.

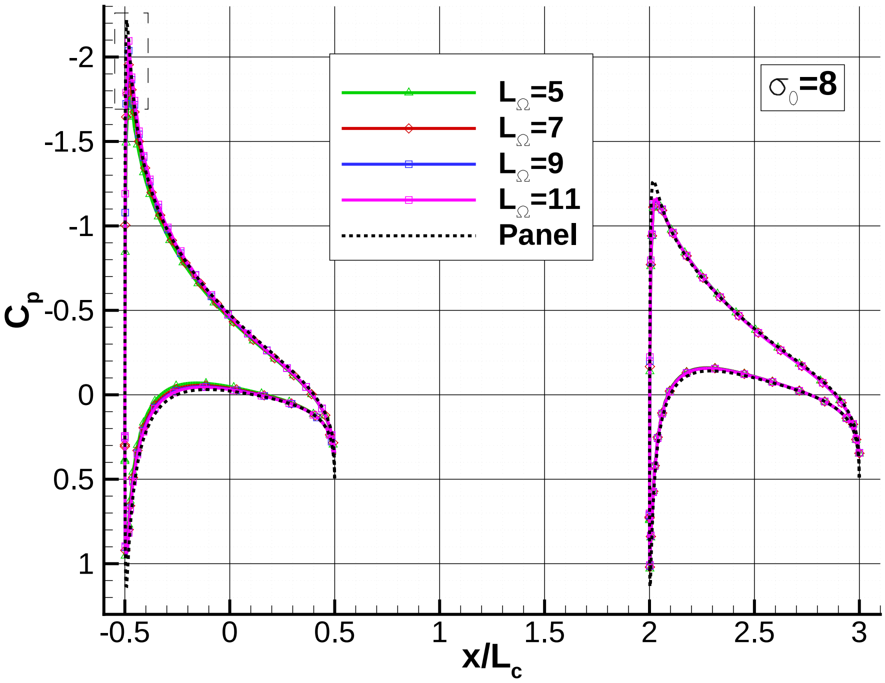

Figure 4.3: C_p for different domain sizes at $\delta_1 = 4°$ and $\delta_2 = 4°$. Enlarged View

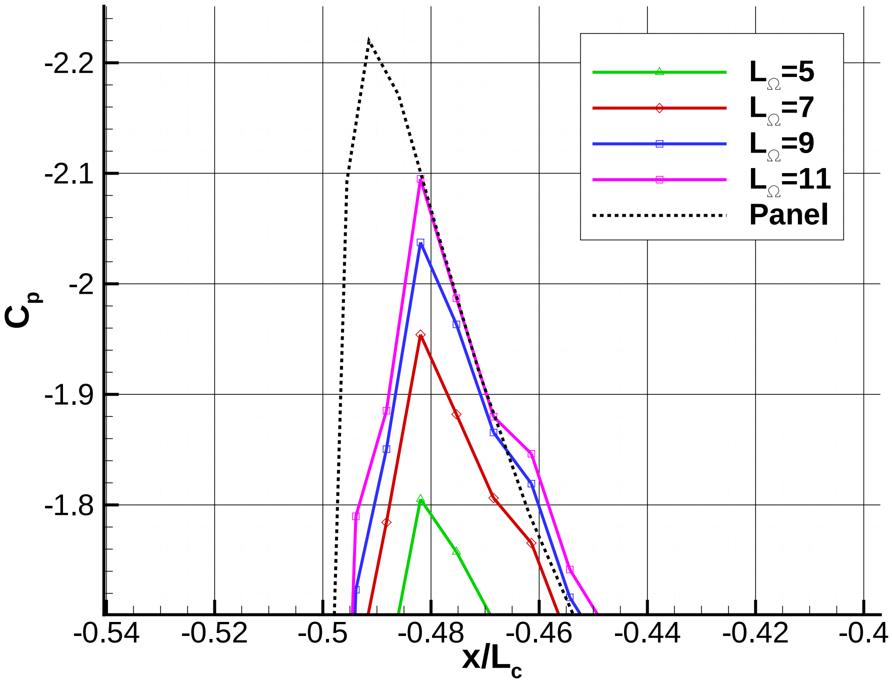

Figure 4.4: C_p for different domain sizes at $\delta_1 = 4°$ and $\delta_2 = 4°$. Zoomed view

Although it could be though that the forcing due to the inclusion of the sponge zone at the boundaries to ensure non-reflecting boundary conditions could affect this pressure peak differences, it turns out that varying the value of the sponge coefficient σ_0 (see Equation 3.73) does not disturb the results. The results of Figure 4.3 and 4.4 where calculated using a value of $\sigma_0 = 8$. In Figure 4.5 the different sponge zone coefficients' results are compared. It is clearly seen that the general shape of the pressure distribution has not changed form Figure 4.3.

On top of that a close look at the leading edge (Figure 4.6) reveals that the differences are inappreciable. This is confirmed by other test done with values of σ_0 ranging from 5 to 11, but due to the fact that all of them lead to very similar results the case of $\sigma_0 = 11$ is shown in Figure 4.7 and 4.8 for the sake of completion. This is a good sign since indicates that the sponge parameter does not affect the solutions and plus, it is seen from Figure 4.4 that solutions between the domain of 9 chord lengths and 11 does not vary that much.

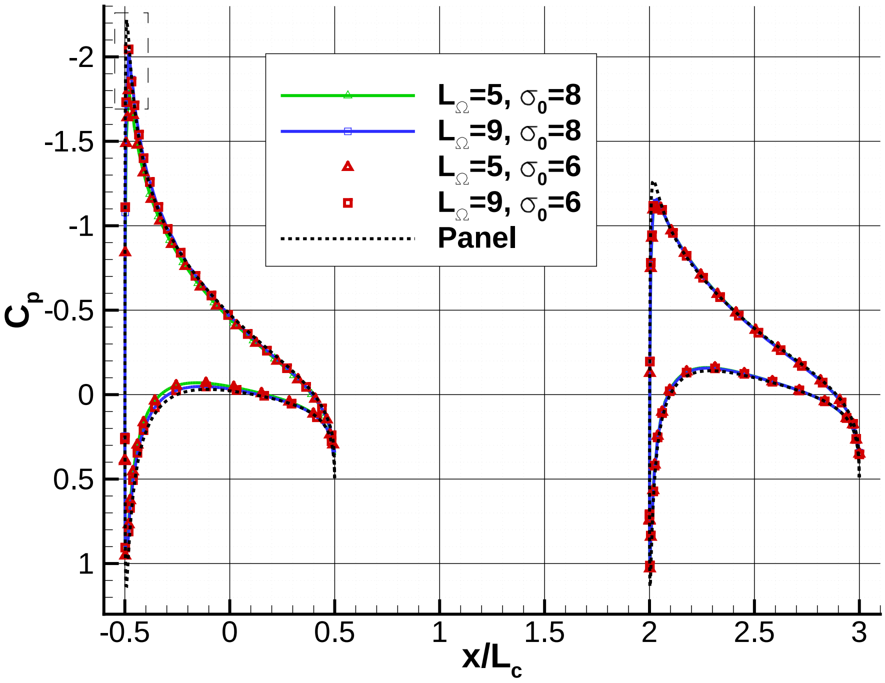

Figure 4.5: C_p for domain sizes of 5 and 9 chord lengths at $\delta_1 = 4°$ and $\delta_2 = 4°$ and $\sigma_0 = 6$ compared with the original sponge configuration with $\sigma_0 = 8$. Enlarged View

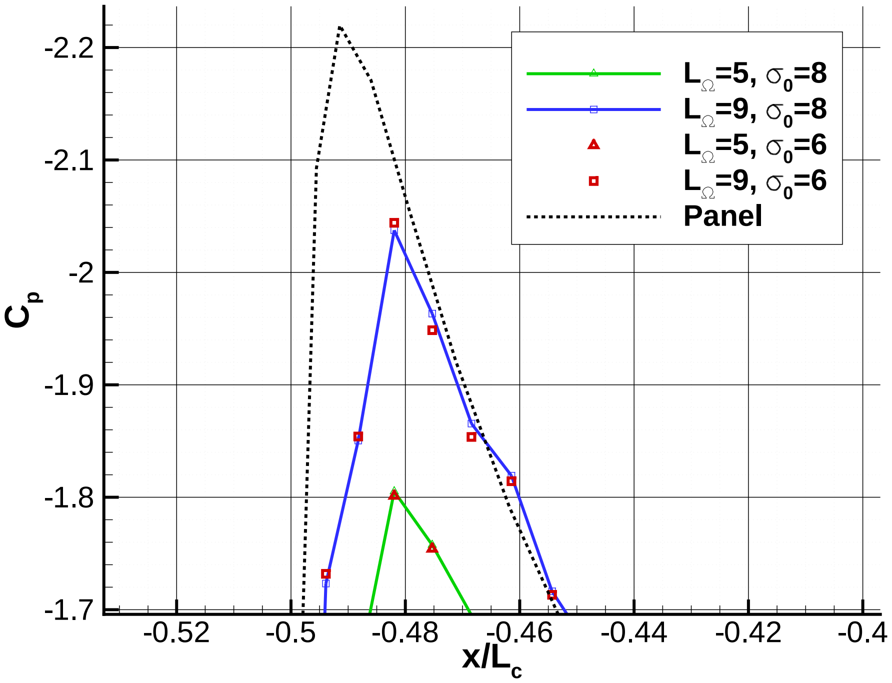

Figure 4.6: C_p for domain sizes of 5 and 9 chord lengths at $\delta_1 = 4°$ and $\delta_2 = 4°$ and $\sigma_0 = 6$ compared with the original sponge configuration with $\sigma_0 = 8$. Zoomed view

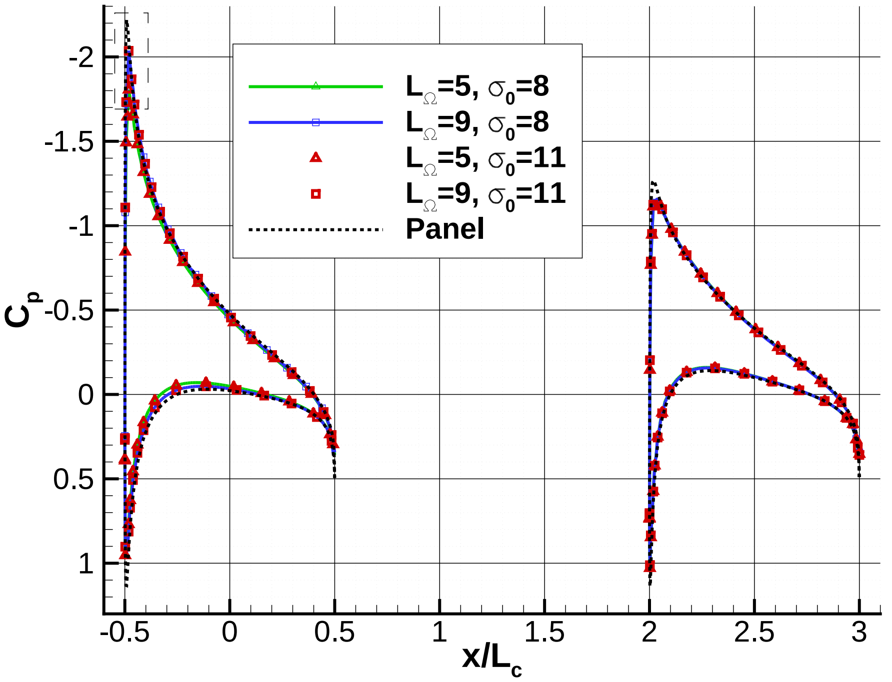

Figure 4.7: C_p for domain sizes of 5 and 9 chord lengths at $\delta_1 = 4°$ and $\delta_2 = 4°$ and $\sigma_0 = 11$ compared with the original sponge configuration with $\sigma_0 = 8$. Enlarged View

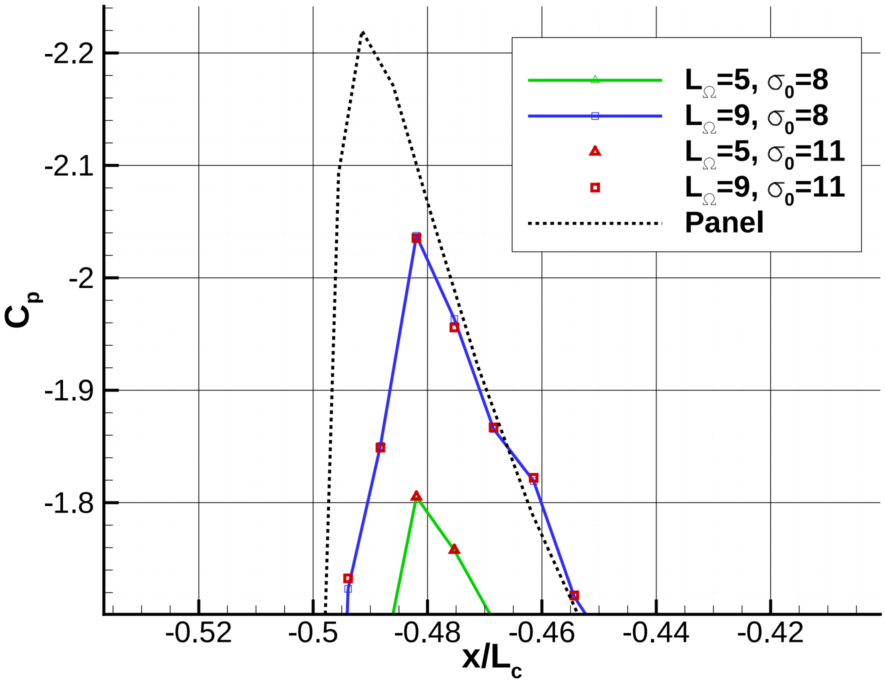

Figure 4.8: C_p for domain sizes of 5 and 9 chord lengths at $\delta_1 = 4°$ and $\delta_2 = 4°$ and $\sigma_0 = 11$ compared with the original sponge configuration with $\sigma_0 = 8$. Zoomed view

4.2.3 Angle of Attack Study

In order to validate the method used in this project to investigate the tandem aerofoil configuration, which is the base of the final study of WLE in the aft element, different simulations were conducted. In first place following what Fanjoy and Dorney [6] did, the effect of varying the inflow incidence angle was tested for small angles between 0° and 4°. The results of this study can be observed in Figure 4.9. Results agree with literature since it is seen that an increase in the angle of attack is much beneficial for the fore element than for the second element. Additionally the agreement with the panel method results is still high. Note here that the angle of attack has been varied the same way for the panel method by changing the free-stream flow's incidence angle too.

However as aforementioned, the implications of such study (changing the flow incidence angle) is only valid for small angles of attack since the interference between both elements is the ultimate goal of the study. If the incidence angle is too high the wake of the first element would be convected at such a high angle that the wake would not impact on to the aft element. And because also one of the main objectives is to perform a parametric study of both elements relative position and WLEs parameters, it is important to be able to rotate the aerofoils at different angles independently. To achieve such thing it is necessary to physically rotate the aerofoils and then create a brand new mesh for each combination of δ_1 and δ_2, whereas changing the flow incidence can be achieved by modification of the boundary conditions, which is much easier and less time consuming. In a sense that is the reason why that approach was initially the one taken. Nonetheless the rotation of the elements was also implemented and results comparing both approaches for $\delta_1 = \delta_2 = 4°$ are shown in Figure 4.10.

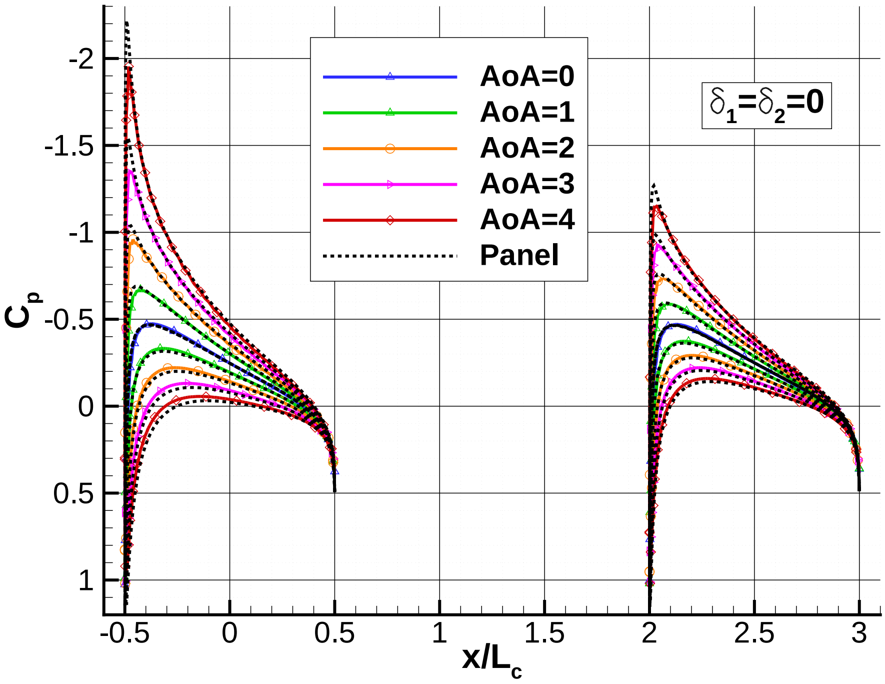

Figure 4.9: C_p distributions for different flow incidence angles. The number after "A" indicates the incidence angle. Black dashed line represents the correspondent panel method computation

It is seen in Figure 4.10 that the level of agreement between both mentioned approaches is very high. Compared with the results from the panel method with element's rotation results are also in good agreement. Being sure that the element's rotation had been correctly implemented, another study was carried where the AoA of the first element was kept fixed at $\delta_1 = 0$ and then the aft element's AoA (δ_2) was varied between 2° and 6°. From Section 2.2 it is known that even while keeping the fore element at $\delta_1 = 0°$ it is still possible to increase its lifting capabilities by increasing δ_2. And that effect is clearly seen in Figure 4.11. However, and although the agreement with the panel method is still really high for the aft element, the potential code predicts slightly higher pressure differences between upper and lower surfaces of the fore element. It must be noted that the panel method does not attend to compressibility effects and the results of it have only been transformed using the Prandtl-Glauert rule (Equation 4.1). Therefore the effect of the dowstream element is much important in the panel method than in the Euler code.

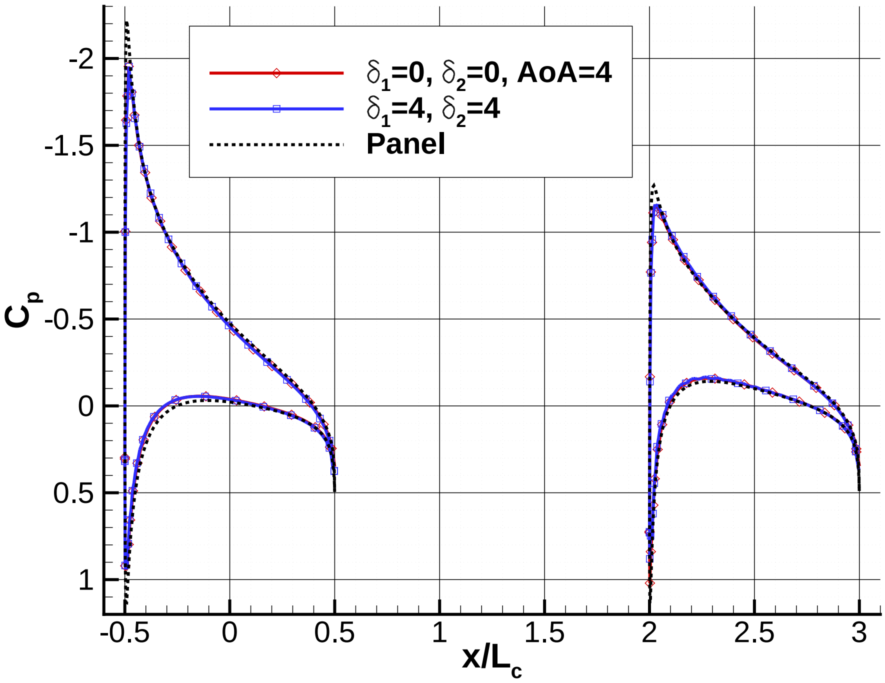

Figure 4.10: C_p distributions for fixed $\delta_1 = 4°$ and $\delta_2 = 4°$ compared with incidence angle case $AoA = 4°$. Black dashed line represents the correspondent panel method computation

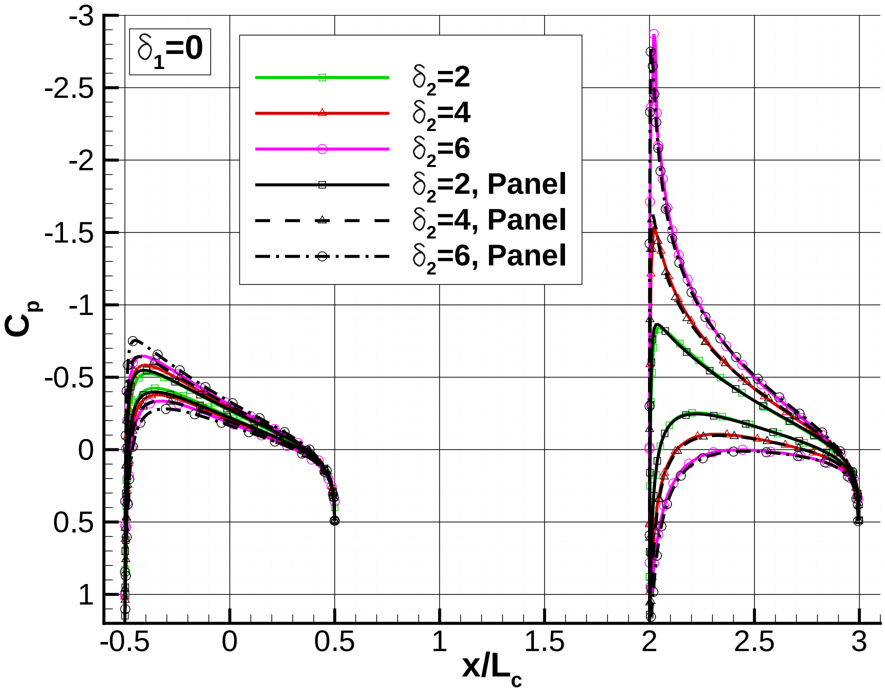

Figure 4.11: C_p distributions for fixed $\delta_1 = 0°$ and different δ_2. Black lines represent the correspondent panel method computation

4.3 Viscous Validation

In the last section (Section 4.2) the inviscid version of the code has been tested for different grids, domains and elements relative positions. However the ultimate goal of the project is to investigate the tandem arrangement in a viscous flow using LES. For this reason in this chapter results from the viscous mode of the code are compared with those of [19]. In [19] a Direct Numerical Simulation (DNS) is performed at $Re = 120000$ over a NACA0012 aerofoil using a finite difference technique on both the streamwise and normal directions whilst a spectral method is used on the spanwise direction.

Jones [19] uses a volume forcing technique to trigger turbulence within the boundary layer. Such technique is mimic and introduced to the code in order to obtain similar results. Additionally, Synthetic Inflow Turbulence (SIF) is used in some cases to increase the level of turbulence in the domain and in the end do the same job as the volume forcing and trigger transition to turbulence in the boundary layer.

In the following sections a recently implemented new grid structure will be presented which gives more freedom in terms of the elements relative position. Also, a grid sensitivity study will be performed on this new grid and results will be compared to those of [19].

4.3.1 New Grid Block Structure

As just mentioned in the prior section, a new grid block structure is introduced at this stage so it will facilitate the investigation of different elements relative position influence on the flow with more freedom. The new structure can be seen in Figure 4.12, and it shows how now the two aerofoils are allowed to come much closer than with the prior grid structure (see Figure 3.4). In addition the new grid allows to have much better aspect ratios for all block's cells, specially in the leading edge regions of the aerofoil which increase the stability of the code. On top of this, the two layers of blocks surrounding the aerofoils allow to increase the computational effort on the aerofoils surroundings in a very efficient, and intuitive manner.

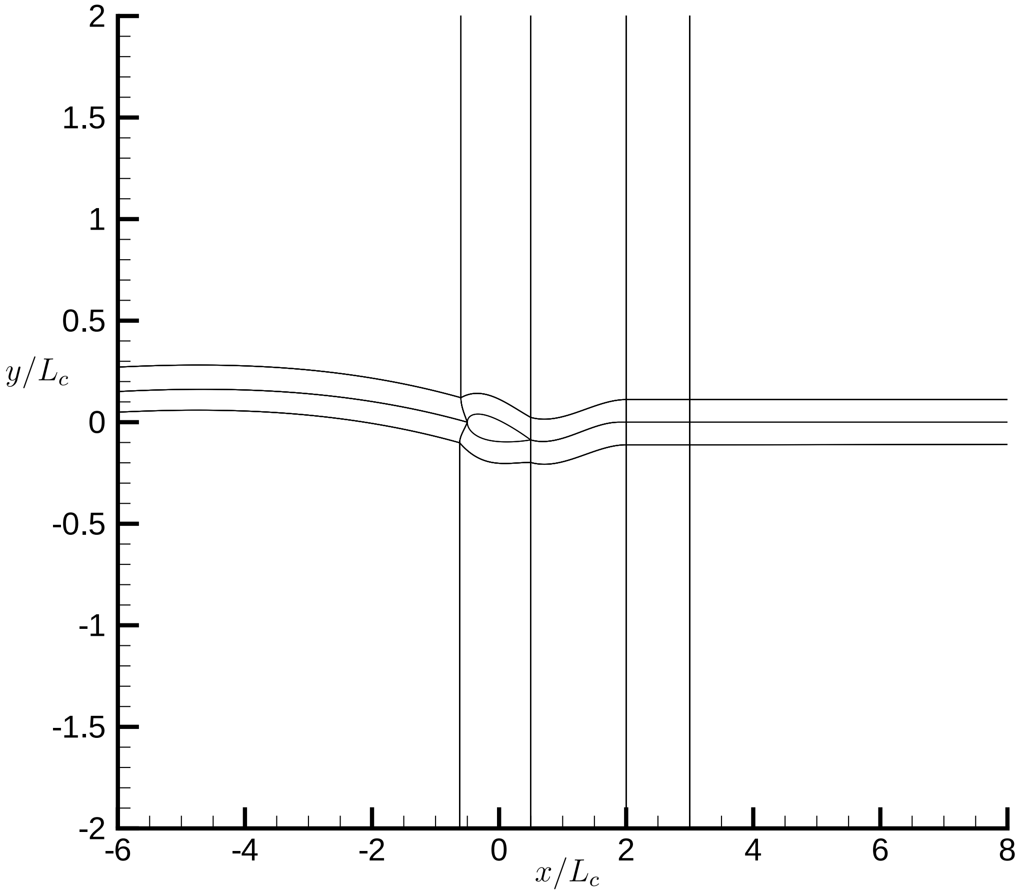

Figure 4.12: New Grid Block Structure Sketch

Nevertheless this new block strategy increments the number of blocks needed per simulation and hence the number of points where communication is needed between blocks. The number of blocks needed is increased from 10 to 20 since the rows of blocks (5 blocks per row) are now 4 instead of 2. A closer look to what the grid looks like near the leading edge can be seen in Figure 4.13

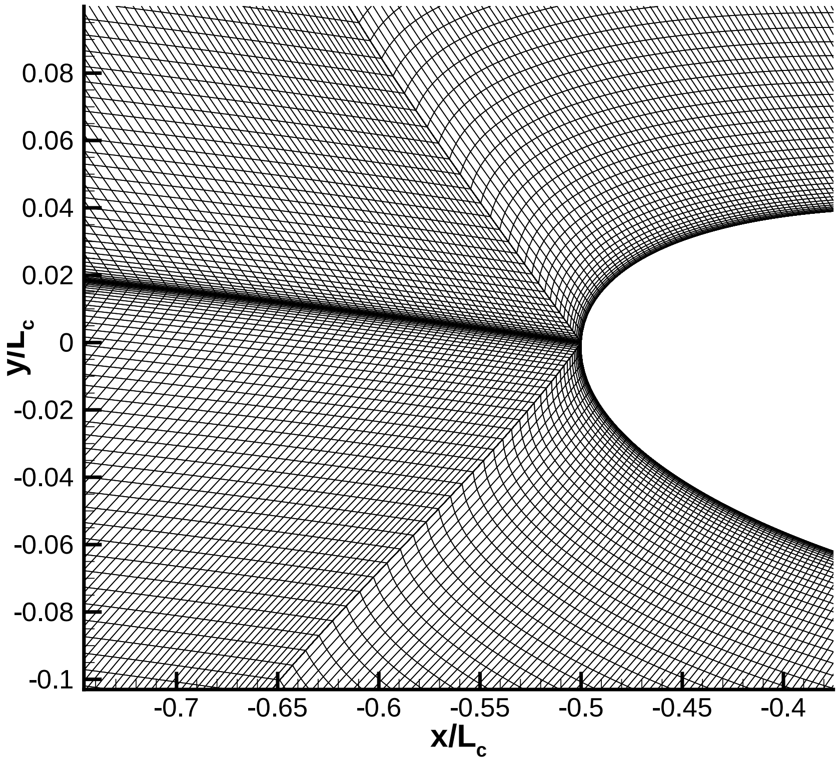

Figure 4.13: New Grid Zoomed view near Fore Element's Leading edge

4.3.2 Triggering Turbulence

Two different strategies are used to achieve the same goal here: triggering turbulence transition in the aerofoil's boundary layer. As mentioned before in [19] a volume forcing method is used. The first method used in the following simulations is similar to that of [19] with minor modifications. The forcing is based on three cosine functions $f_1(t), f_2(t)$ and $f_3(t)$ with three different frequencies $\omega_f = [\omega_{f1}, \omega_{f2}, \omega_{f3}]$. The forcing is applied at the same location of [19] (x_{fo}, y_{fo}). A weighting function is used $g_f(x, y)$ so the forcing is maximum at $x = x_{fo}$ and $y = y_{fo}$ and then fades away with distance from this point. The expression of the weighting function is:

$$\begin{aligned} g_n(x,y,z) &= \frac{1}{2}\exp\left(-k_0 R^2\right)\cos\left(\beta_{fn} z\right), \\ \text{with:} \qquad k_0 &= \frac{\ln\left(0.0001\right)}{r_f^2}, \\ \beta_{fn} &= \frac{2\pi n}{span}, \\ R &= \sqrt{(x - x_{fo}) + (y - y_{fo})}, \end{aligned} \tag{4.2}$$

where r_f is the radius of influence around the forcing point and β_{fn} is the spanwise wavelengths that will be excited by the forcing. Finally the forcing function is simply given by

$$\begin{aligned} F(x,y,z,t) &= \sum_{n=1}^{n=3} f_n g_n \\ \text{where:} f_n &= A_f \cos(w_{fn} t)/3 \end{aligned} \tag{4.3}$$

The parameters used for the forcing are given in Table 4.4 where M_∞ is the free stream Mach number.

Table 4.4: Forcing Parameters (assume aerofoil's trailing edge at $(x, y) = (1, 0)$)

Parameter	Value
x_{fo}	0.1
y_{fo}	0.129
ω_{f1}	$44.76M_\infty$
ω_{f2}	$53.60M_\infty$
ω_{f3}	$53.60M_\infty$
β_{f1}	$\frac{2\pi}{span}$
β_{f2}	$\frac{6\pi}{span}$
β_{f3}	$\frac{8\pi}{span}$

The second method used to trigger turbulence is based on the work of Kim [24]. In this method synthetic Homogeneous Isotropic Turbulence (HIT) is quietly injected at the most upstream boundary by means of the sponge zone (see Section 3.8). If sufficient amount of turbulence remains when it reaches the aerofoil after being convected by the mean flow, the boundary layer will naturally transition to turbulence.

Figure 4.14 shows the effect of using the Volume Forcing for example. It can be noticed how vortical structures start to develop after the boundary layer becomes turbulent.

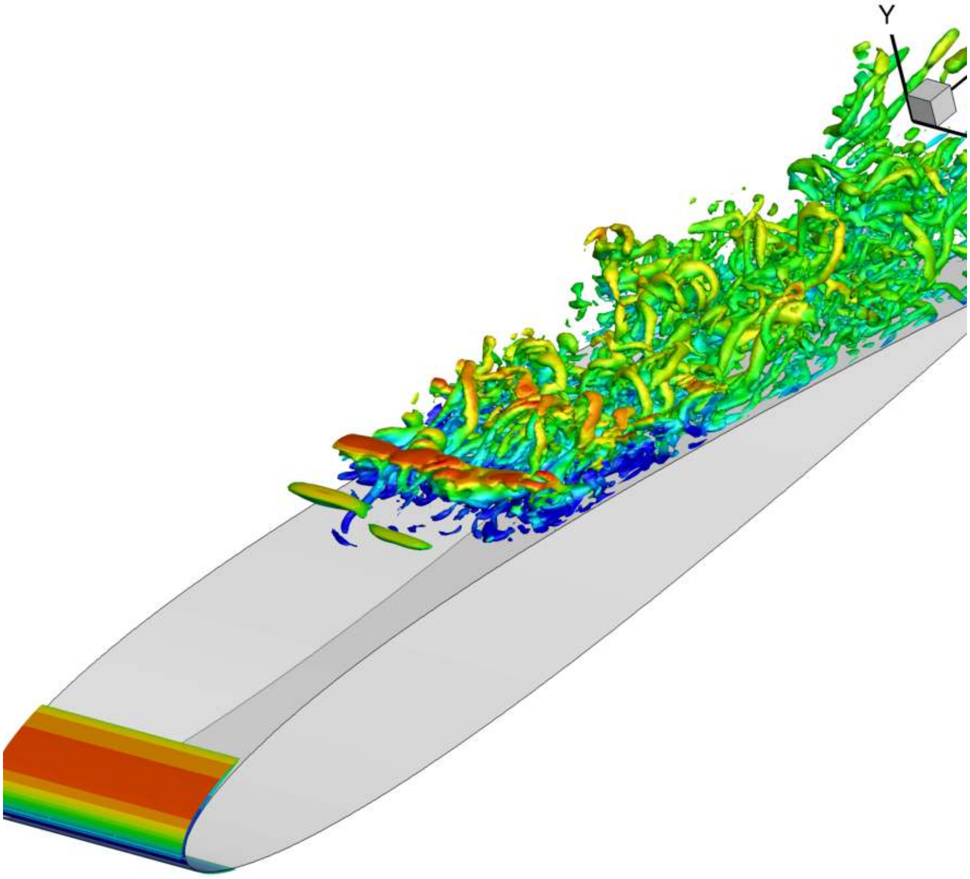

Figure 4.14: Isosurfaces of the non-dimensional velocity gradient second invariant $Q = 150$ coloured by streamwise Mach number

Table 4.5: Separation and Reattachment points

Case	x_s	x_r
VF	0.089	0.594
SIT	0.071	0.594
3DU [19]	0.099	0.607

Figure 4.15 shows comparison between both methods and also against [19, fig. 12]. It is seen that both methods give good approximations to the DNS solution, with the SIT case having a little over-prediction. However both methods do agree in terms of separation and reattachment points. The case tested here is a NACA0012 aerofoil at $\alpha = 5°$ and $Re = 1.2E5$. It is shown in [19] that for this flow conditions a Laminar Separation Bubble is present, which length is given by the separation x_s and reattachment x_r points just mentioned.

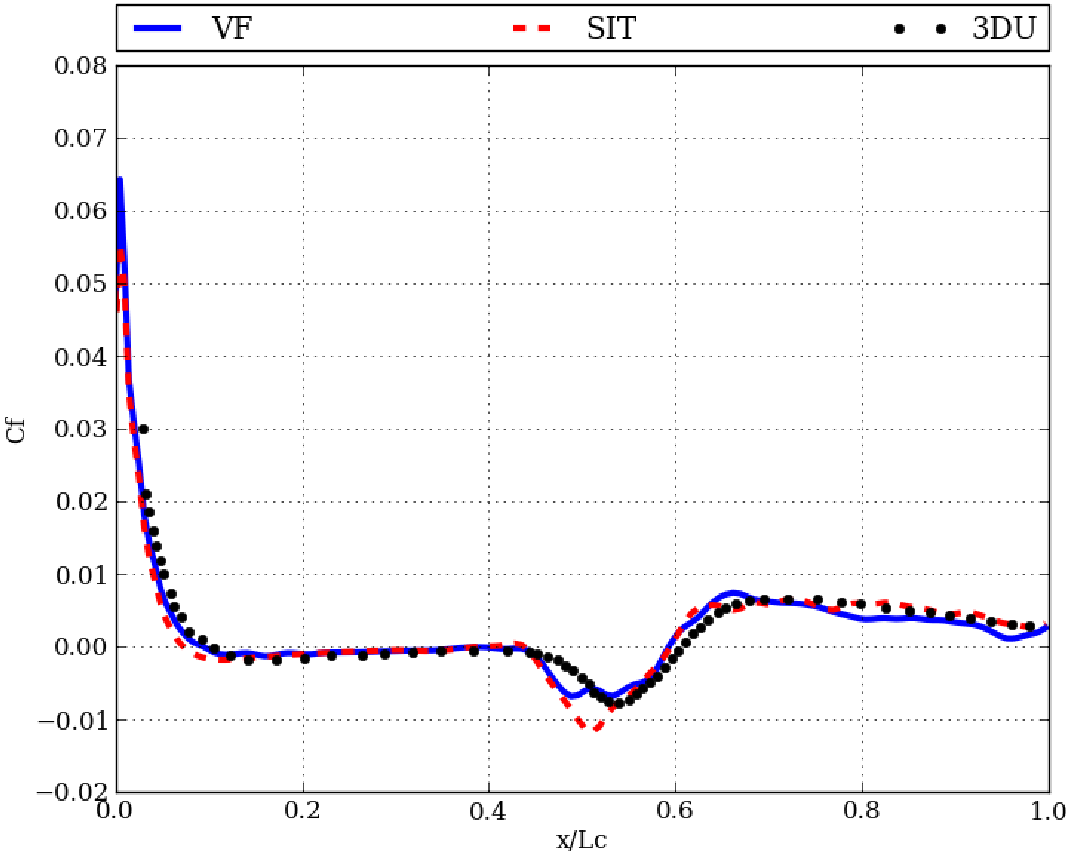

Figure 4.15: C_f comparison between Volume Forcing (VF) and Synthetic Inflow Turbulence (SIT) methods for triggering transition

From Table 4.5 it can be seen that the deviations are -1.049% and -2.77% of the chord length (L_c) for the separation point respectively in each case, and $+1.274\%$ for the reattachment point for both cases. In this particular case, where it is known from literature where the forcing needs to be applied, the Volume Forcing might be more convenient, however if this was not known, the SIT method proves to give close results in terms of separation and reattachment points. In future computations where the nature of transition is not known a priori, the SIT method seems to be the way to go.

Nevertheless for the sake of this validation case, the Volume Forcing method is used in all results shown in this chapter unless it is stated otherwise.

4.3.3 Grid Dependence Study

In the past section the grid used for both VF and SIT cases was based on the G1 grid parameters (see Table 4.6), but other three more grids have been used to test the sensitivity of the simulations to different discretisation levels. In Table 4.6 the number of points used per block in each direction can be checked, where ξ_n is the number of points used in blocks of column n in the ξ direction and η_n is the number of points used in blocks of

Table 4.6: Grid case study

Grid:	G1	G2	G3	G4
ξ_0	200	400	200	300
ξ_1	150	200	200	300
ξ_2	100	100	100	100
ξ_3	50	100	80	80
ξ_4	200	400	200	300
η_0	180	360	180	180
η_1	60	60	60	60
ζ_0	50	50	75	75

row n in the η direction. The row and column distrubution can be seen in Figure 4.16. Note that row 2 is equal to row 1 and row 3 is equal to row 0 because the problem is set to be symmetric with respect to the centre line in terms of grid points.

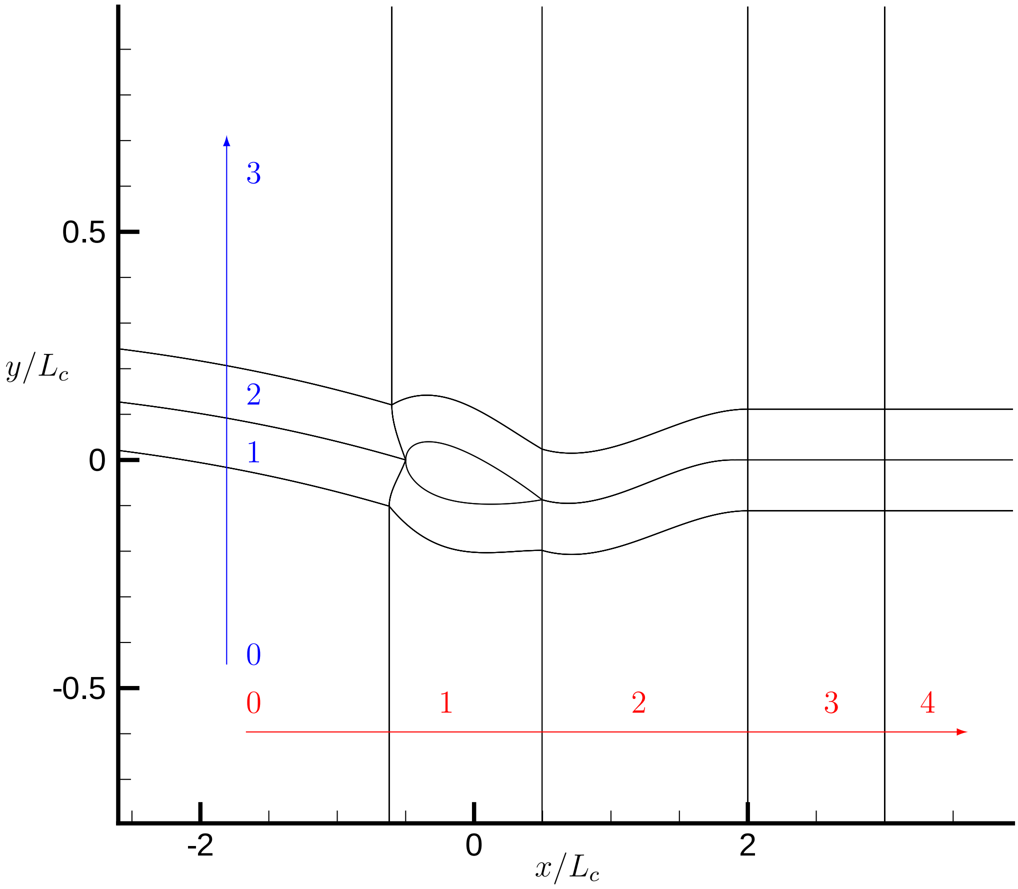

Figure 4.16: Columns and Rows structure for the grid

The results from this four grids are compared in Figure 4.17. It is observed that the most determinant parameter is the number of points used in the span direction, since the curves converge to G4 when the number of points is increased. It is also observed that agreement with the DNS case (3DU) is best up until the 40% of the chord length and then after the 70% of the chord length. However both G3 and G4 disagree in the middle section with respect to the DNS, where coarser grids seem to give closer results to 3DU.

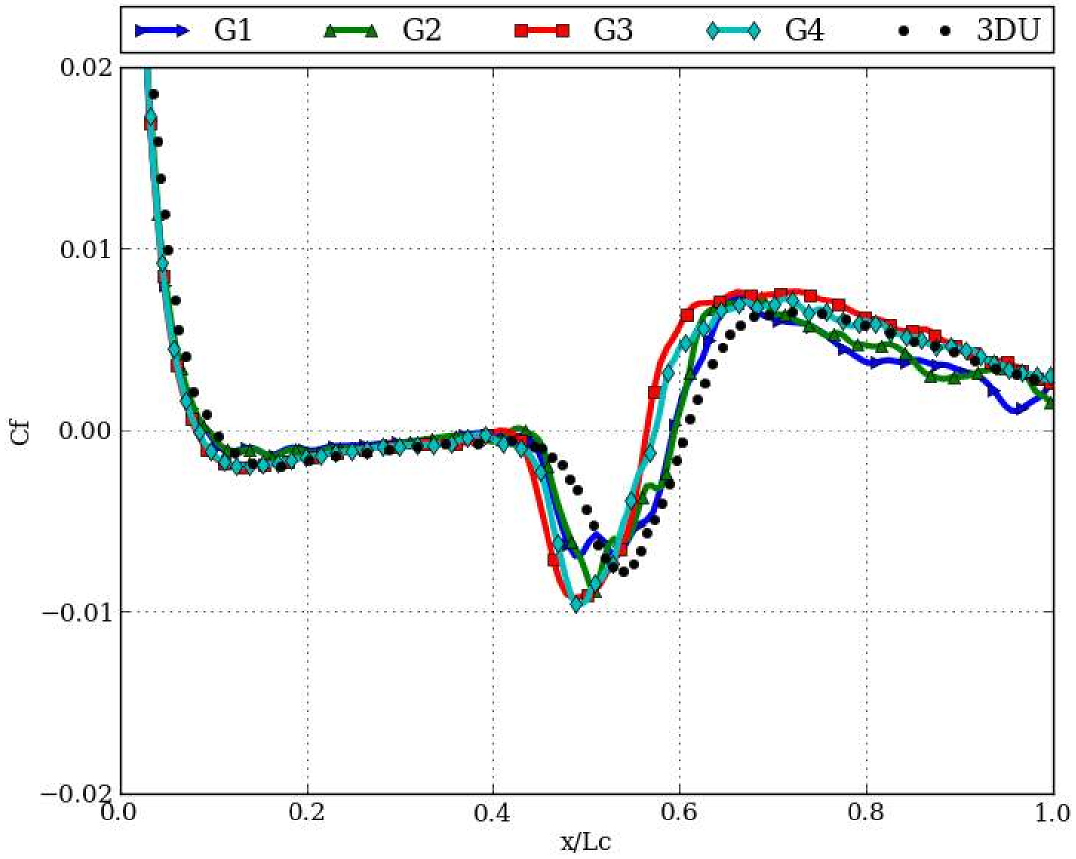

Figure 4.17: Comparison of C_f for different grids

In Table 4.7 the correspondent lift and force coefficients are presented for each grid case showing that G4 and G3 are the closest to the DNS case in terms of C_l. However there is a big disagreement in terms of C_d despite the fact that curves in Figure 4.17 seem to be quite close to the DNS curve.

Table 4.7: Force coefficient for each Grid case

Grid:	C_l	C_d
G1	0.585	0.0226
G2	0.585	0.0209
G3	0.616	0.0191
G4	0.608	0.0199
3DU [19]	0.621	0.0358

4.3.4 Spectral Analysis

In order to investigate the resolution capabilities of the LES code the Power spectra of turbulent kinetic energy $K = \frac{1}{2}(< u'u' > + < v'v' > + < w'w' >)$, is computed and then compared to the DNS [19]. Data acquisition took place over 50 non-dimensional units (non-dimensinalised using the free stream velocity and the chord length). Eight windows with the shape of a squared sinusoidal were used with a 50% overlap to improve spectra quality at the expense of reducing the range at the low frequency end. The data was measured at $x = 0.3961$ and $y^+ = 13.2$.

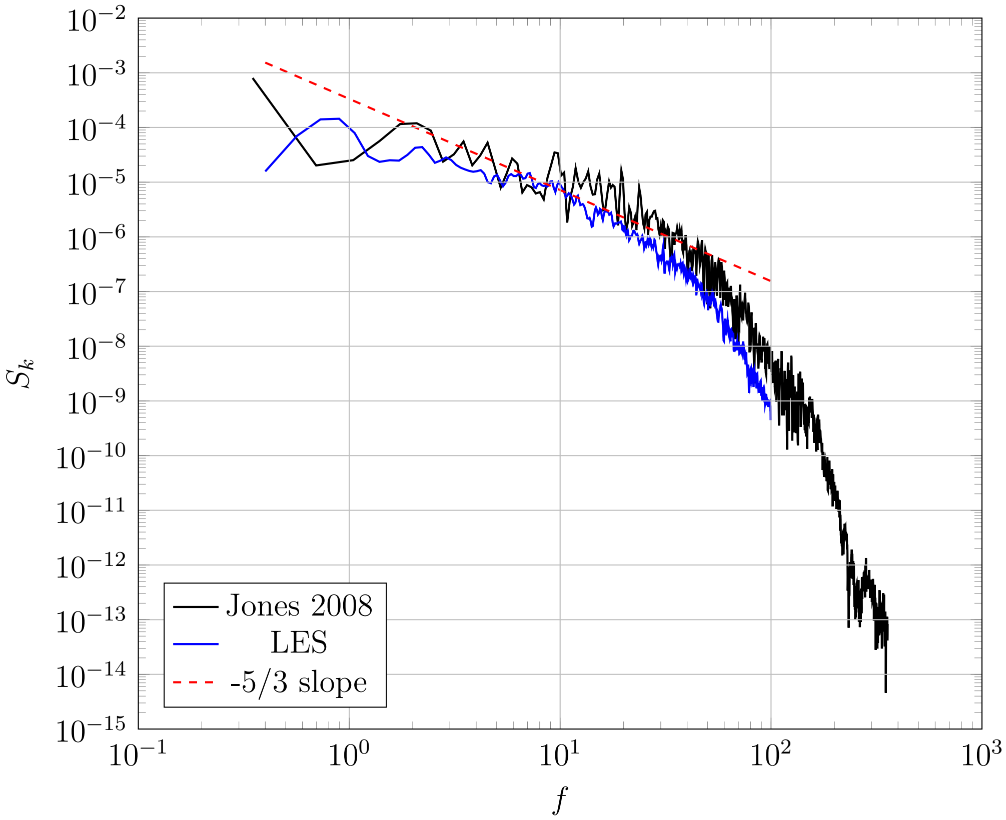

Figure 4.18: Temporal Power Spectra of K taken at the mid-span compared with DNS [19] and the $-5/3$ slope of the Inertial Subrange. Frequencies non-dimensilasied by the free stream velocity and the chord length

Figure 4.18 shows how the data from LES approaches quite well with both DNS and the theoretical slop up until $f \approx 25$. At higher frequencies both DNS and LES diverge from the $-5/3$ slope of the turbulence's inertial subrange. Then at the high frequency end due to the coarser resolution used in the LES case the energy contained at those scales shows to be lesser than the DNS results.

Chapter 5

Results: Single Aerofoil

5.1 Introduction

In the previous chapter (Chapter 4), the validation of the code has been divided in two stages: inviscid and viscous. Both cases tested share similar aspects with the main focus of the project, a WLE aerofoil. The inviscid case tested a similar geometry and the viscous tested a similar flow condition, i.e. aerofoil in a viscous flow at incidence. The time has hence come to look at problems that can give us some answers to the questions that this project focuses on.

The first problem that the student has focused on is the single NACA0021 aerofoil with WLE at different AoAs. The WLE parameters were chosen to be the same as in Skillen [49], that is $\lambda_{LE} = 0.11\bar{L}_c$ and $h_{LE} = 0.015\bar{L}_c$, which was also tested by Hansen et al. [11] (model $A2\lambda7.5$) in the University of Adelaide water tunnel. Both numerical and experimental investigations were performed at at $Re = 1.2 \times 10^5$, and so is this one.

Since the results reported by Skillen showed almost no difference between simulations performed with aerofoil span of $L_b = 2\lambda_{LE}$ and $L_b = 4\lambda_{LE}$ a span of $L_b = 2\lambda_{LE}$ was used in order to keep computational cost at its minimum.

It was suspected that the results of Skillen did not match those of Hansen (the C_l coefficient reported by Skillen was more than 40% more than the experiment) because no boundary layer tripping technique was used. Therefore it was decided that the SIT technique [24] used in 4.3.2 would be useful here to trigger the transition of the boundary layer at a chord location closer to the experiment. In addition to the case of $\alpha = 20°$ tested by Skillen, two extra cases at $\alpha = 6°$ and $\alpha = 10°$ were also aimed. The three AoAs tested will offer different pictures of the same problem at pre-stall, close to stall, and post-stall regimes. However using such a high AoA ($\alpha = 20°$) increased the skewness of some grid elements close to the leading edge of the aerofoil which ultimately made the solution very unstable. Consequently the desired AoA was achieved by increasing the flow incidence angle rather than rotating the aerofoil itself, i.e. the same technique that was used in 4.2.3. This technique could be used since only one aerofoil was used, however using this inflow incidence angle from the very beginning of the simulation would cause the inflow turbulence go over the aerofoil instead of impinging on it.

Finally the following process was chosen so the inflow incidence could be used in combination with the SIT.

1. The aerofoil is accelerated until the desired Mach number for $5t^*$, with $t^* = tL_c/a$ where t is time, L_c is the mean chord length and a is the speed of sound.
2. The SIT is used at $\alpha = 0°$ for $25t^*$.
3. The SIT is progressively switched off during $10t^*$.
4. The incidence angle α is ramped up to the desired value for another $10t^*$.

In total $50t^*$ were needed to reach to the desired flow state, and then wait until the solution was converged. Because the grid did not change between different incidence angles steps 1 to 3 were performed just once and saved. From that stage all simulations were ramped up to the desired α hence saving $40t^*$ per simulation.

In the following sections many flow variables are plotted, unless stated differently all of them have been non-dimensinalised using the free stream speed of sound a and the mean chord length L_c. Furthermore, the notation used for time averaged quantities is the following: for example the time averaged velocity magnitude is represented by $< |u| >$. The centre of coordinates is located in the intersection of the spanwise symmetry plane, the thickness symmetry plane and a chord normal plane passing by the middle chord.

5.2 Turbulent Inflow Condition

In Table 5.1 a comparison between the force coefficients obtained are compared to the experiment of Hansen. Although the case for $\alpha = 10°$ is really close to the experiment, the cases for $\alpha = 20°$ and specially for $\alpha = 6°$ did not match the experimental data as well. The discrepancy for the $\alpha = 6°$ case may be explained because during the course of the four step process mentioned above some errors were made during the last step. The AoA ramping was hence not the same followed by the other two cases causing some history effects that would in the end delay the convergence of the final result. The SIT was set to produce turbulent inflow of 0.5% turbulence intensity with an integral lengthscale of 0.4 Leaving the $\alpha = 6°$ aside for future revision the focus of the study shifted towards the other two cases, particularly to the highest AoA since it could be compared to the results of Skillen. If the $\alpha = 20°$ case is compared with the results obtained by Skillen [49] it can be seen that the agreement with experimental data was improved in terms of the lift coefficient (see Figure 5.1). In terms of the drag coefficient, the value is in the same order of magnitude that the lift coefficient.Surprisingly the agreement with Skillen's results is hight too.

Table 5.1: Mean Lift and Drag

α	C_l [11]	$< C_l >$	relative error	C_d [11]	$< C_d >$	relative error
6	0.555	0.751	35%	0.042	0.033	21%
10	0.895	0.892	0%	0.059	0.056	5%
20	0.729	0.641	12%	0.286	0.320	12%

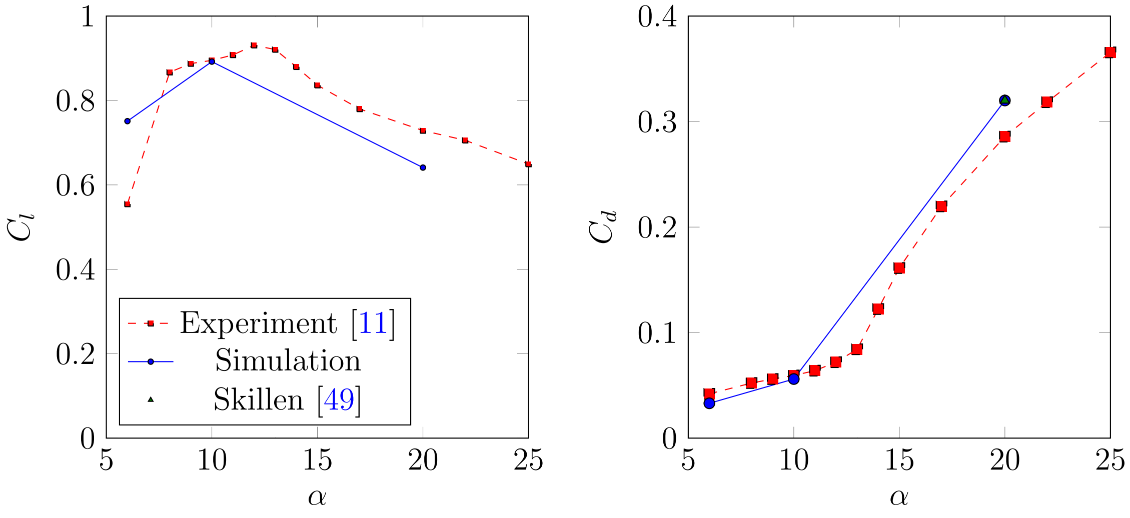

(a) Lift comparison

(b) Drag comparison

Figure 5.1: Force coefficient comparison between present simulation, Hansen [11],and Skillen [49]

In Figures 5.2 and 5.3 the time history of the force coefficients is shown. The $\alpha = 10°$ case converged quickly to a stable solution with a little variance. On the other hand the $\alpha = 20°$ case took much longer. Even after more than $200t^*$ the coefficients had very low frequency variations that made difficult to asses whether the solution was still evolving or not. On top of that there seemed to be a higher frequency content in the signal, that will be considered in detail in following sections.

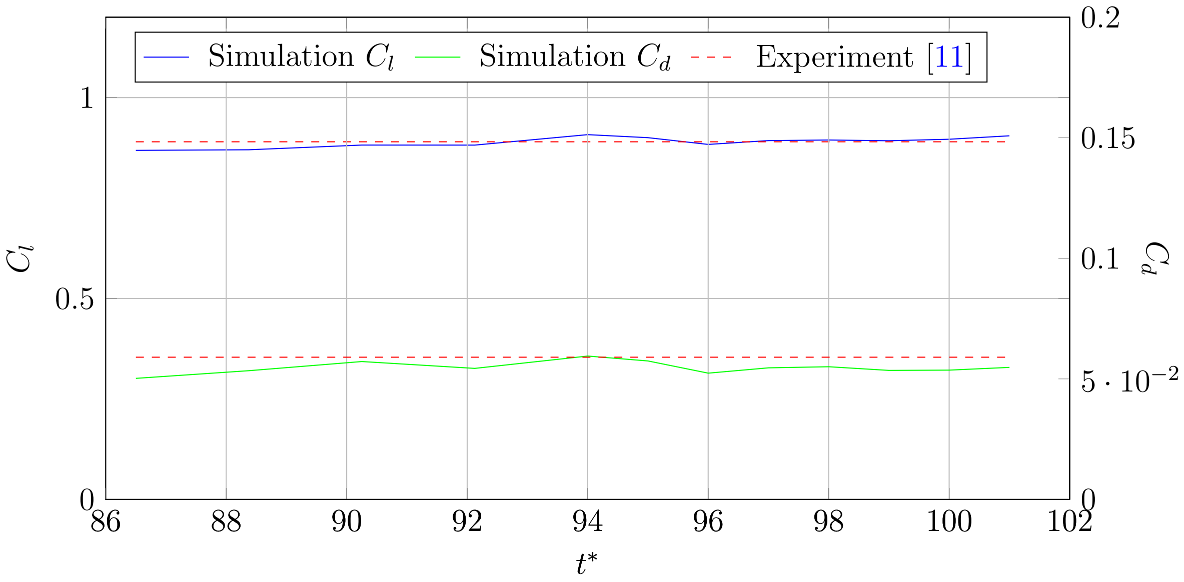

Figure 5.2: Time History Force Coefficients comparison between Simulation and Experimental data at $\alpha = 10°$

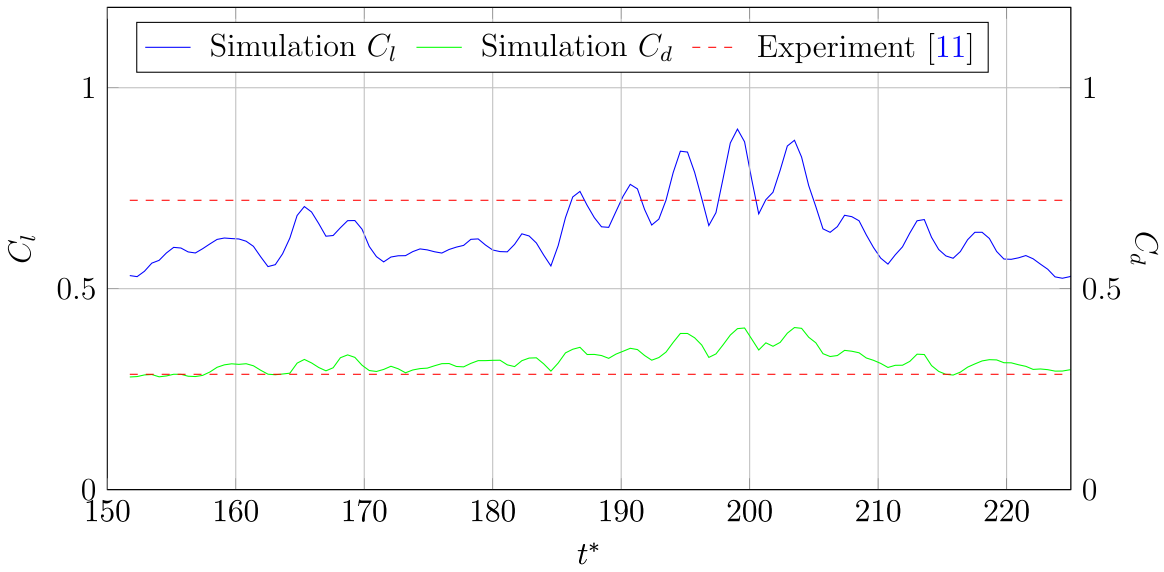

Figure 5.3: Time History Force Coefficients comparison between Simulation and Experimental data at $\alpha = 20°$

In Figure 5.4 the contours of the pressure coefficient show how in the case of $\alpha = 10°$ the undulations promote a periodic pattern in the first quarter of the aerofoil chord, where the lowest pressure is located at every trough section. This can be easily appreciated in Figure 5.6 where the pressure coefficient at the surface is measured across the span. The probe line is produced by the intersection of a computational plane of constant $\xi = 50$ and the aerofoil surface, which is also a computational plane of constant $\eta = 0$. The constant pressure in the span direction present at the trough sections indicates the presence of a Laminar Separation Bubble [10, 45] in the troughs. These LSBs are more likely to happen at the trough sections where the flow suffers from the highest adverse pressure gradients [17]. In the case of $\alpha = 20°$, Figure 5.4a, the LSB has significantly reduced its length, and more important it is only present in one trough. This asymmetry in the flow was also present in some RANS results from Rostamzadeh [44] at AoAs higher than the baseline stall angle. However in comparison to the Skillen's results [49] this is a completely different behaviour.

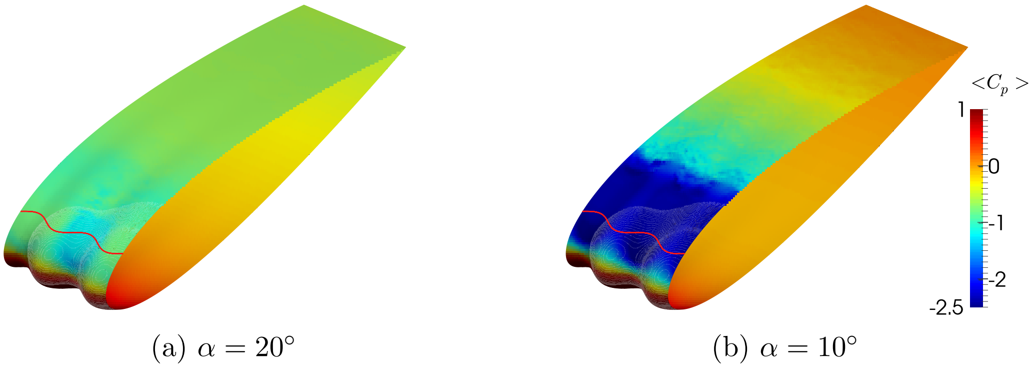

(a) $\alpha = 20°$ (b) $\alpha = 10°$

Figure 5.4: Time Averaged Pressure Coeficient. Red line shows probe line used in Figure 5.6

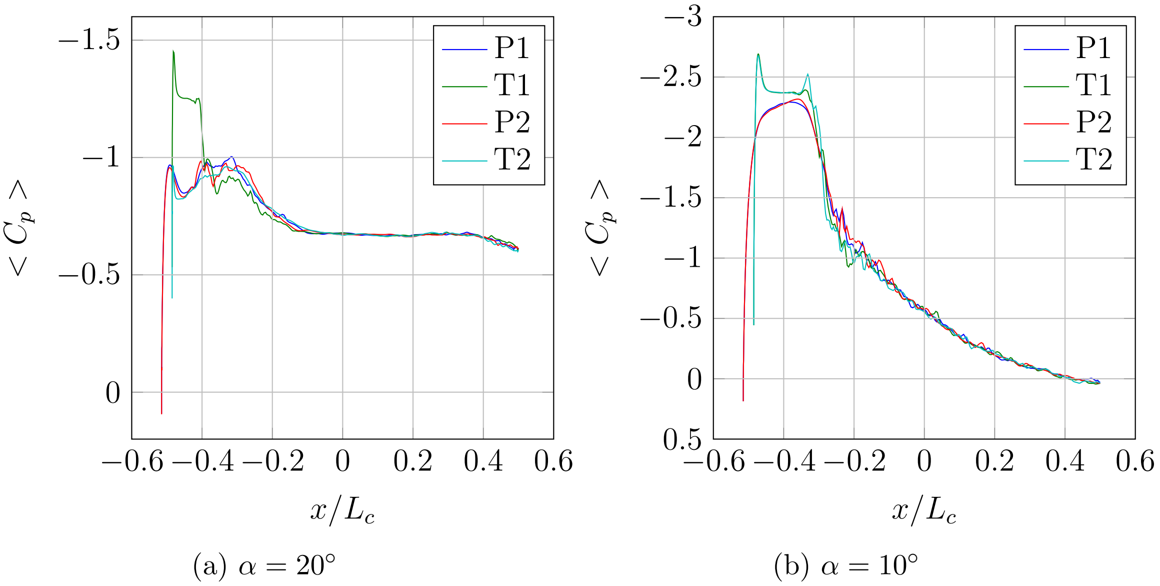

(a) $\alpha = 20°$ (b) $\alpha = 10°$

Figure 5.5: Pressure Coefficient distributions at different sections for $\alpha = 10°$ and $\alpha = 20°$

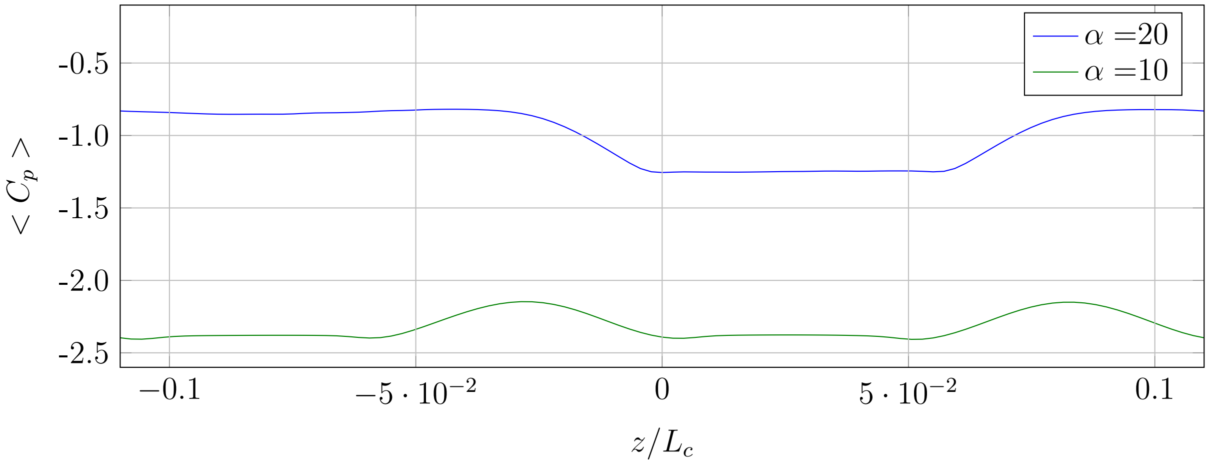

Figure 5.6: Time Averaged Pressure Coefficient across the span at $\xi = 50$ for $\alpha = 10°$ and $\alpha = 20°$

In Figure 5.5b the pressure distributions along the chord for $\alpha = 10°$ show that the flow is very alike between sections of the same kind, i.e. peak to peak or trough to trough. Even between different sections the difference only exists in the first third of the chord. In contrast, for $\alpha = 20°$ only the Trough 1 (T1) sections differs from the rest. In both cases the LSB can be identified by the plateaus in the pressure coefficient distributions.

The differences in the flow pattern between the two cases is more significant in Figures 5.7 and 5.10 where the technique developed by [2] has been used to depict the surface flow patterns. The range of the scale used to colour the surface has been deliberately reduced so the regions of recirculating flow can be easily identified by blue regions on the figure. In Figure 5.7 it can be seen how the flow is almost identical at the two leading edge wavelengths. In each of them the flow between peaks rapidly encounters the LSB and climbs over it hence increasing its velocity. This increased velocity creates a lower pressure that is transmitted in the wall normal direction towards the wall, as a consequence the pressure inside the bubble is determined by the pressure of the flow just above it. An estimation of what the pressure should be inside the bubble given the velocity of the flow just above it can be done using the following formula:

$$\frac{\gamma}{\gamma - 1}\frac{p}{\rho} + \frac{|u|^2}{2} = \frac{\gamma}{\gamma - 1}\frac{p_\infty}{\rho_\infty} + \frac{|u|^2_\infty}{2}, \tag{5.1}$$

which is commonly known as the Bernoulli equation for compressible flows. From Figure 5.9 it is seen that the velocity at the edge of the LSB is $|u_{LSB}| \approx 0.755$. Using then Equation 5.1 leads to a pressure value of $p_{LSB} \approx 0.525$ which ultimately leads to a $C_{pLSB} \approx -2.37$, very close to what Figure 5.8 shows. On the other hand the flow in the peaks remains laminar for the first quarter of the chord. The flow on sections that are not exactly in the peak sections is drawn towards the trough sections due to the spanwise pressure gradient.

Figure 5.7 also show how the flow transitions to turbulence straight after the LSBs inside the troughs, and that this transition triggers transition not just on the troughs but everywhere else too.

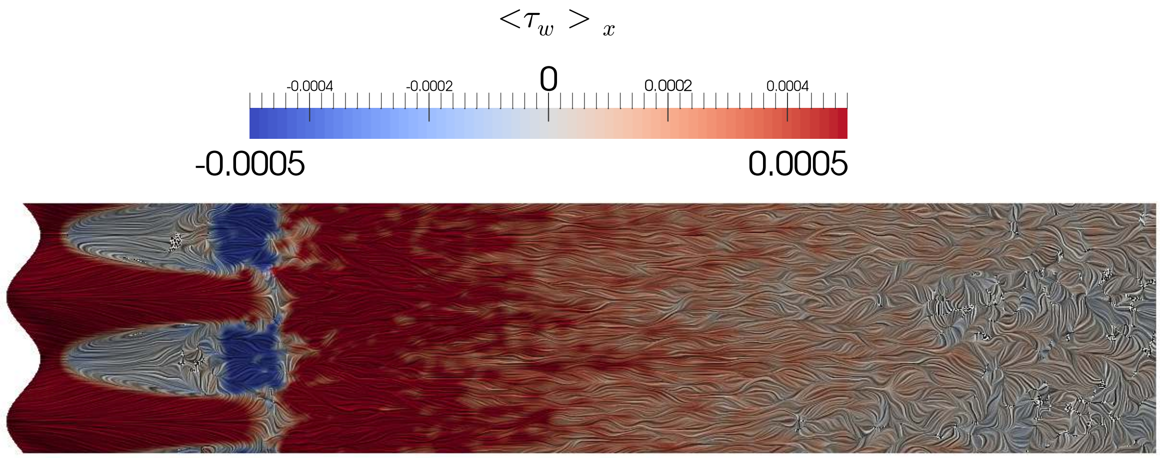

Figure 5.7: Linear Integral Convolution of $<\tau_w>$ Coloured by $<\tau_w>_x$ at $\alpha = 10°$

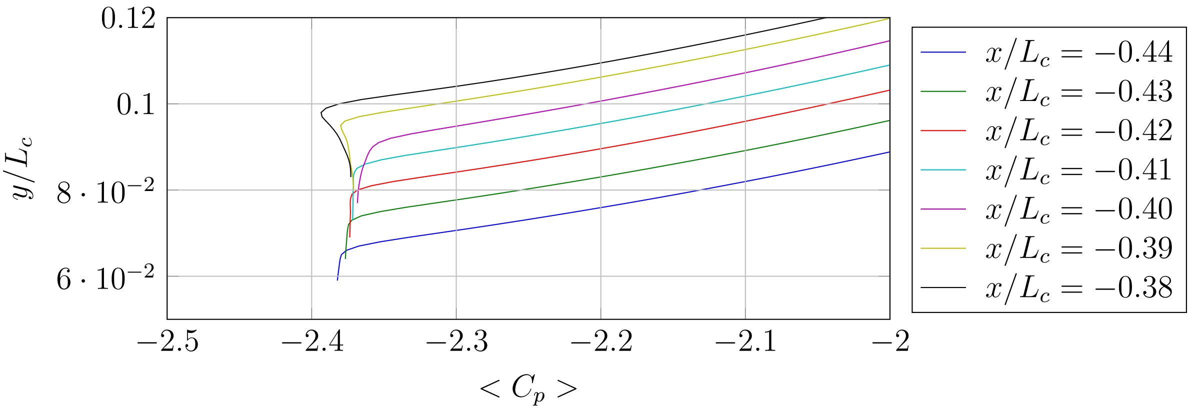

Figure 5.8: Time Averaged Pressure Coefficient profiles for different streamwise locations within the LSB for $\alpha = 10°$

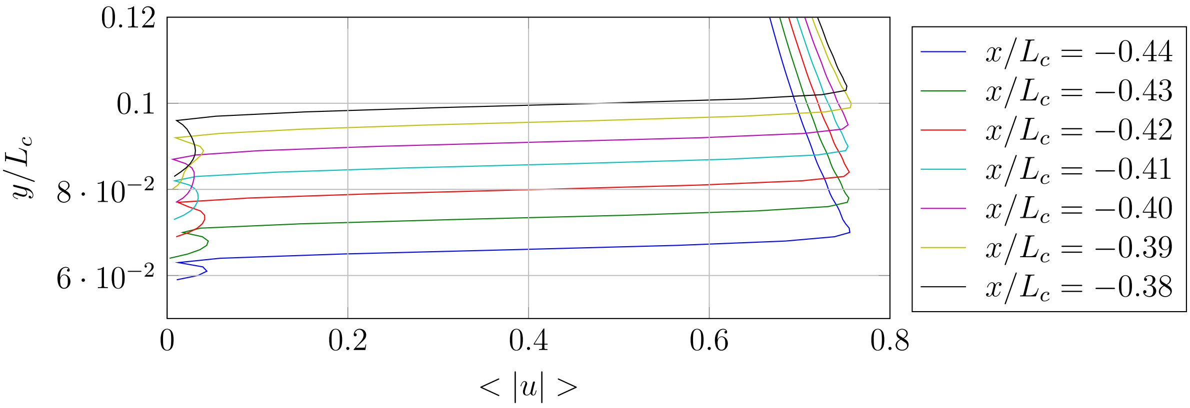

Figure 5.9: Time Averaged Velocity Magnitude profiles for different streamwise locations within the LSB for $\alpha = 10°$

Figure 5.10 shows the surface flow pattern for the $\alpha = 20°$ case. The picture here is completely different to the other case. It seems that at very high AoA the symmetry of the flow is broken and just one of the LSB manages to survive whereas the flow in the other trough undergoes laminar separation at the very leading edge. In the trough with the presence of the LSB, the flows transitions to turbulent just after the bubble, and remains attached for a short period. In Figure 5.11 it can be seen how there is a portion of the chord in the first trough (T1),between $x/L_c \approx -0.4$ and $x/L_c \approx -0.2$, where the friction coefficient becomes positive for a while. On the other trough however, separations occurs much earlier, almost at the same point where the friction coefficient becomes positive in the trough with the bubble.

Because results previous to this project did show a clear periodicity in the flow from wavelengh to wavelength [49], it was thought that probably the inconsistency with previous published reports could be attributed to the solution initialisation described at the beginning of the section, i.e. the process of impinging inflow turbulence and pitching the aerofoil. It could be that history effects still remaining were causing this asymmetric solution being triggered. Consequently, a new set of tests were performed in order to further investigate whether this behaviour was due to any simulation artifact or was indeed how the flow is supposed to be at this high AoA.

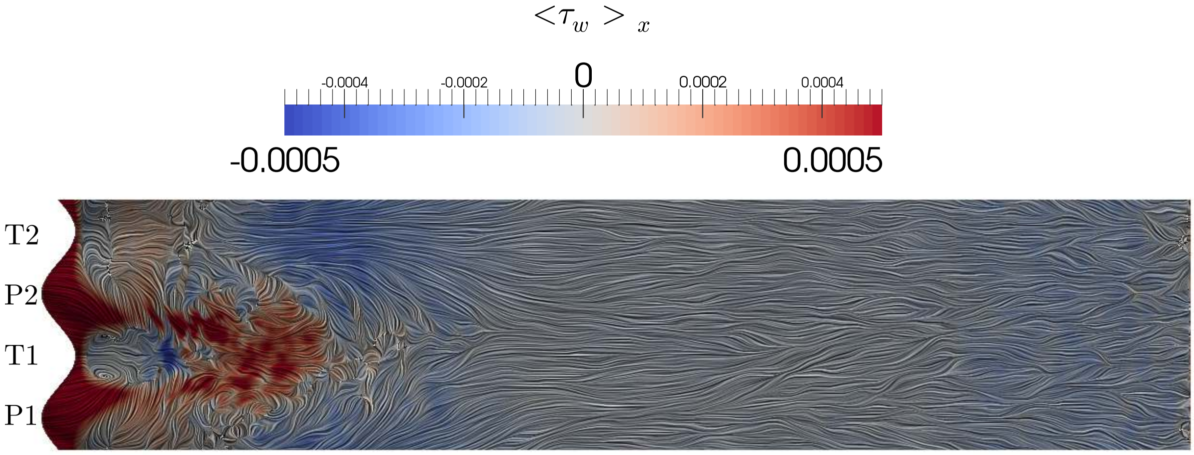

Figure 5.10: Linear Integral Convolution of $<\tau_w>$ Coloured by $<\tau_w>_x$ at $\alpha = 20°$

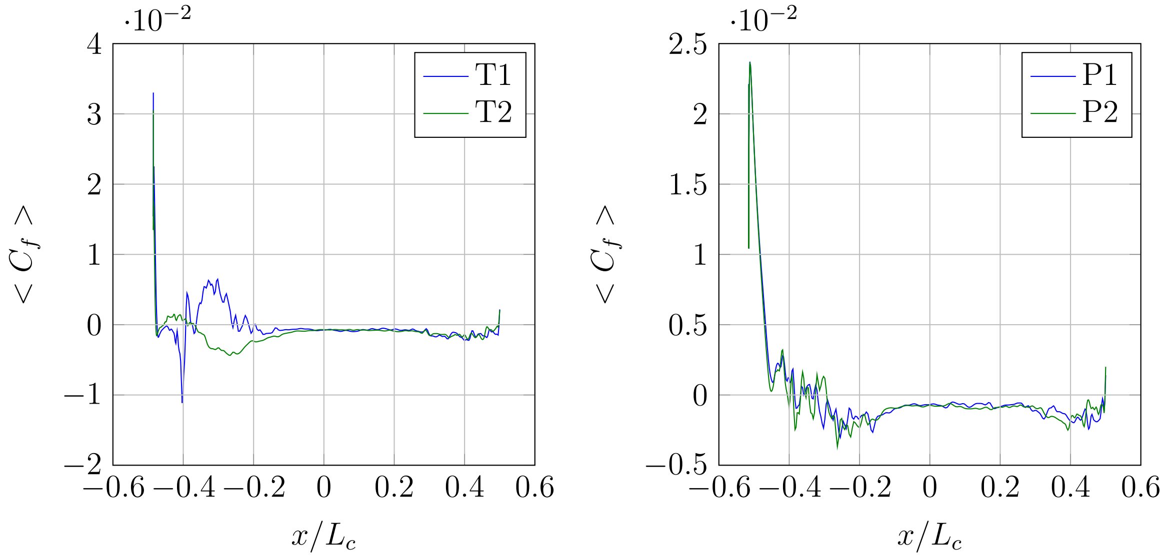

(a) Troughs

(b) Peaks

Figure 5.11: Friction Coefficient distribution along the chord for Peaks and Trough sections

5.3 Clean Inflow Condition

In this subsection the results presented were achieved setting from the very beginning the inflow incidence angle to the desired value. Additionally the inflow condition was set to be laminar with no perturbations at all. The purpose of this set of simulations was to investigate whether the asymmetry in the flow seen in the previous section (5.2) was a consequence of the simulation procedure or was indeed the natural flow behaviour.

5.3.1 Steady Analysis

Figure 5.12 and Table 5.2 show how the force coefficients did not significantly change after modifying the flow initialisation. The lift coefficient was mildly improved, however the drag coefficient increased its prediction which was already over the experimental data. Here, the results for the straight leading edge case are also shown. Differences here with respect to Hansen [11] are higher, however, using other experimental data available [16] and assuming linear variation between different Re a $C_l \approx 0.65$ is expected at $Re = 1.2 \times 10^5$.

Table 5.2: Mean Lift and Drag for Clean Inflow compared to Literature

Case	$< C_l >$	relative error	$< C_d >$	relative error
Hansen WLE [11]	∼0.729	-	∼0.286	-
Skillen [49]	1.03	∼41%	0.13	∼54%
Simulation WLE	0.678	∼7%	0.326	∼14%
Hansen Straight [11]	∼0.54	-	∼0.31	-
Skillen Straight [49]	0.64	∼18%	0.32	∼3%
Simulation Straight	0.687	∼27%	0.365	∼18%

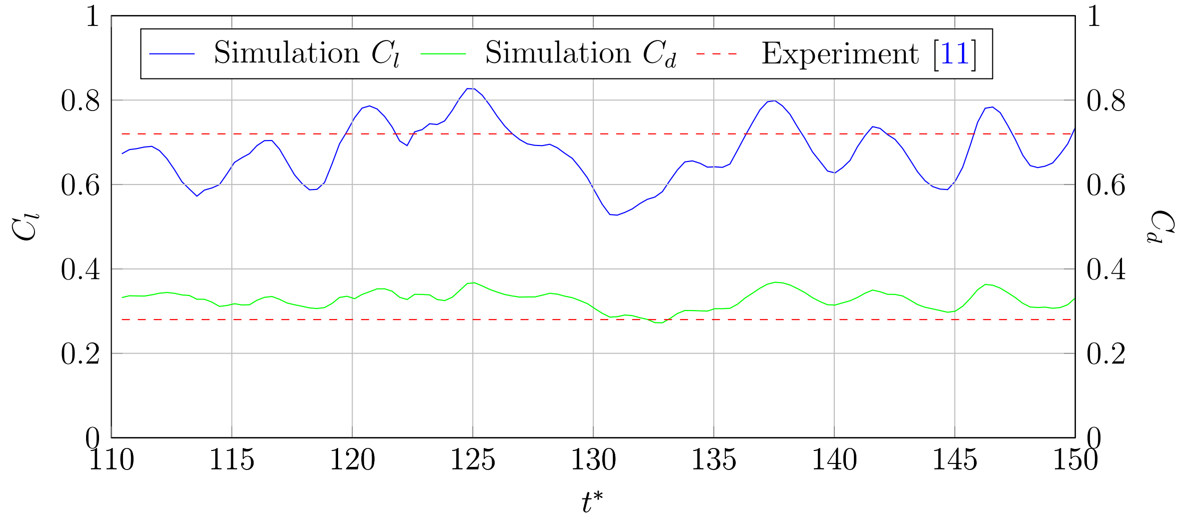

Figure 5.12: Time History Force Coefficients comparison between Simulation and Experimental data at $\alpha = 20°$ for Clean Inflow Case

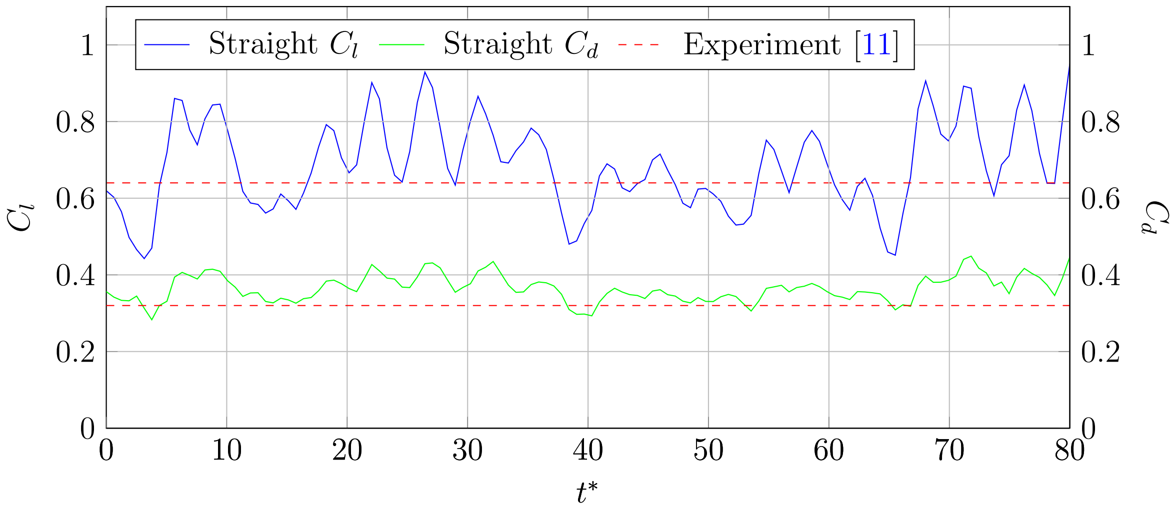

Figure 5.13: Time History Force Coefficients comparison between Simulation and Experimental data at $\alpha = 20°$ for Straight Leading Edge with Clean Inflow Case

It is seen that there is some low frequency signature in the C_l signal, as it was in the turbulent inflow case, so it can be concluded that those oscillations are unrelated to the type of flow initialisation used. Nonetheless Figure 5.14a shows how the laminar separation bubble has now moved from trough 1 (T1) to trough 2 (T2). It is also seen that the lowest pressure is still located at the trough containing the LSB. In Figure 5.15 can be seen how different are the pressure distributions along each trough and how similar are at the peaks in contrast. Most interesting the pressure distribution on the peaks seems to be very similar to that of Trough 1. Nearly after $x/L_c = -0.2$ the spanwise homogeneity is recovered where the negative C_f profile indicates flow separation. In comparison to the straight case, in the first 5% of the chord length, the only section that differs from it is the T2 section.

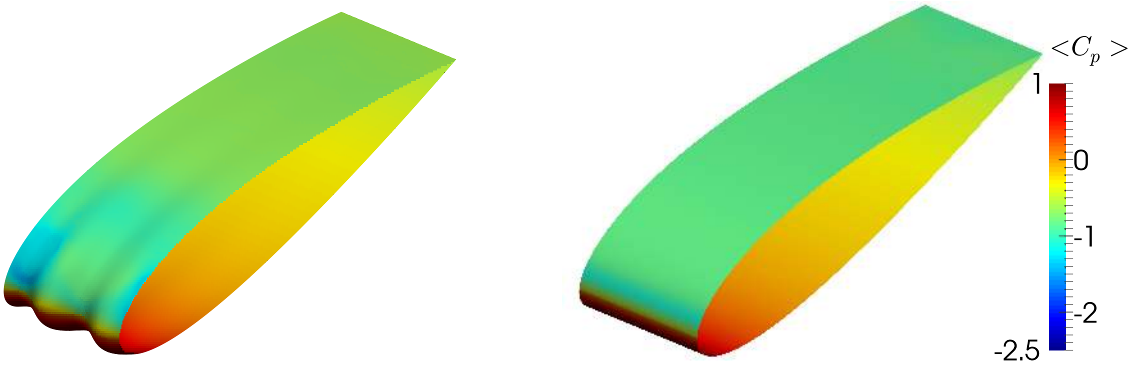

(a) WLE (b) Straight

Figure 5.14: Pressure Coefficient contours over the surface of both WLE and straight leading edge cases at $\alpha = 20°$

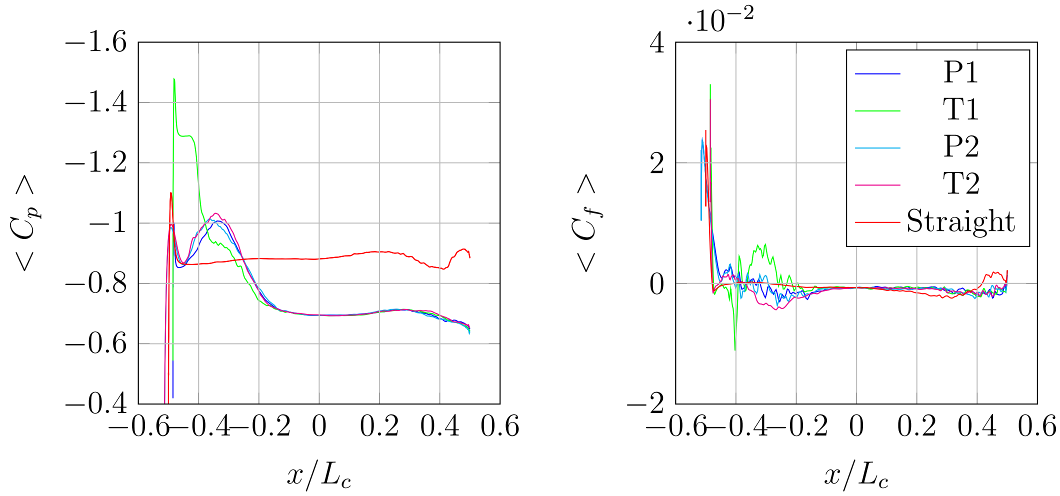

(a) Pressure Coefficient

(b) Friction Coefficient

Figure 5.15: Pressure and Friction Coefficient distributions along the chord for peak and trough sections compared to the straight case

Figure 5.16a shows the isocontours of zero streamwise velocity, which can be used to depict regions with recirculating flow, i.e. Laminar Recirculation Bubbles. It can be clearly identified the region where the LSB is sitting. It is seen how the spanwise homogeneity of the flow is broken by the presence of just one LSB. The flow partially reattaches downstream the bubble, however due to the strong adverse pressure gradient eventually separates. On the other hand the separated region seems to originate at Trough 1, and advances towards closer span sections downstream. In the straight leading edge case the separated region covers the entire span and more than 90% of the chord length.

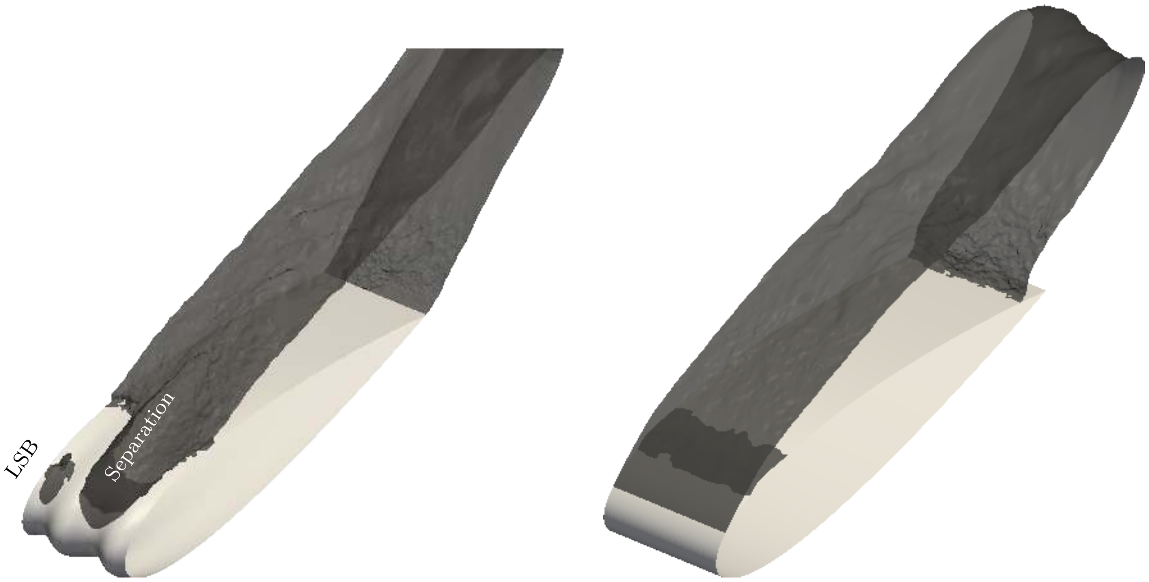

(a) WLE

(b) Straight

Figure 5.16: Iso-Contours of zero averaged streamwise velocity

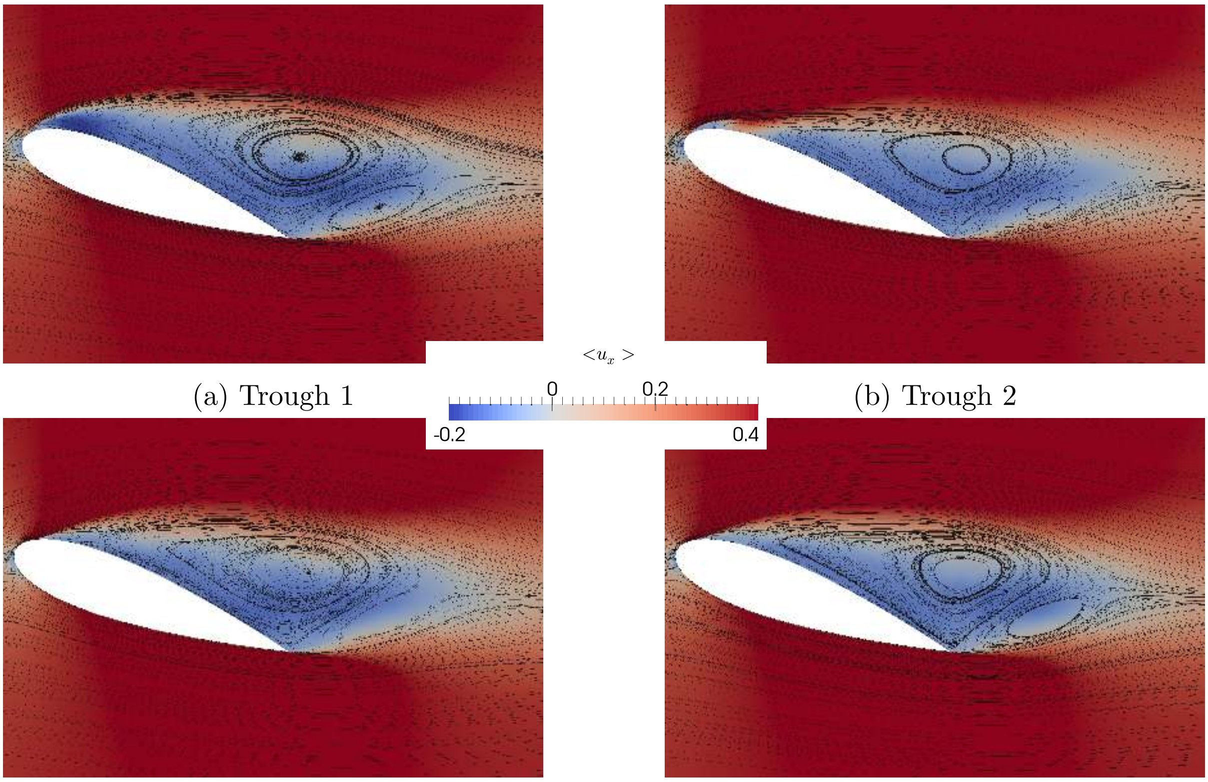

(a) Trough 1

(b) Trough 2

(c) Peak 1

(d) Peak 2

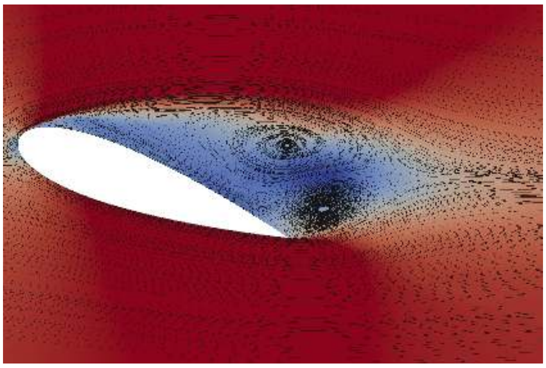

(e) Straight

Figure 5.17: Streamlines at different span sections coloured by the averaged streamwise velocity

This is more clearly seen in Figure 5.17 where a comparison between the flow at the two troughs and two peaks is showed by means of the streamlines and the streamwise velocity contours. It is seen how the streamlines come closer to the aerofoil surface at Trough 2 but almost immediately separates at Trough 1. At Trough 2, downstream the bubble the flow reattaches as depicted by the red colour in Figure 5.17b, however the streamlines suggests that the new developing turbulent boundary layer is very thick, which in the end makes it more prone to separate due to adverse pressure gradients. There seems to be a tiny recirculation zone very close to the leading edge at the Trough 1 which could be also a tiny LSB since one can also see a small plateau in the $< C_p >$ plot of Figure 5.15a. The size of this plateau region is much smaller than the one that can be seen for the other trough section on the same figure. On the peaks sections (Figures 5.17c, and 5.17d) separation happens later than in Trough 1, however when the separated region originated at Trough 1 reaches their spanwise section the flow there separates too as it is seen in Figure 5.18. In comparison with the straight case, the only section that is clearly different from it is the Trough 2 section because of the presence of a reattachment region downstream the LSB, although in general it seems that the wake developed by the WLE case seems to be slightly smaller, with the two recirculation zones looking somewhat weaker than in the straight case. Particularly, the shape of the clockwise recirculation zone seems to cover the entire aerofoil section for the WLE case whereas in the straight case the anti-clockwise vortex sits on top of the trailing edge. The shape of the close wake is hence different for both geometries, with a slender shape associated with the WLE case. For the straight case the two big vortices are sitting one on top of the other almost in a vertical line, and consequently the wake shape seen in the streamwise direction is thicker. On the other hand, for the WLE, because the clockwise vortex covers the whole aerofoil chord length, the other vortex is displaced a little downstream, which ultimately leads to the two vortices being aligned rather horizontally, and consequently elongating the shape of the wake and reducing its projection to the normal streamwise direction.

By means of Figure 5.18 the surface flow patterns can be investigated. The LSB can also be spotted here close to the leading edge in Trough 2 (T2). It is worth noting that the high momentum flow from the peaks is drawn towards the lower pressure zone in T2. Even some air from inside the separated region in T1 is attracted to the other trough creating a secondary flow that eventually create two foci (F1 and F2) of vertical vorticity. For the straight case, Figure 5.19, the surface flow is much simpler. In this case the Linear Integral Convolution technique could now be used since the values of the $<\tau_w>$ were almost zero in most of the aerofoil surface, and this cause to show spots where just the white noise convoluted shows up. Because of this the WSS lines were used instead, which show clearly how the separation happens at the very leading edge.

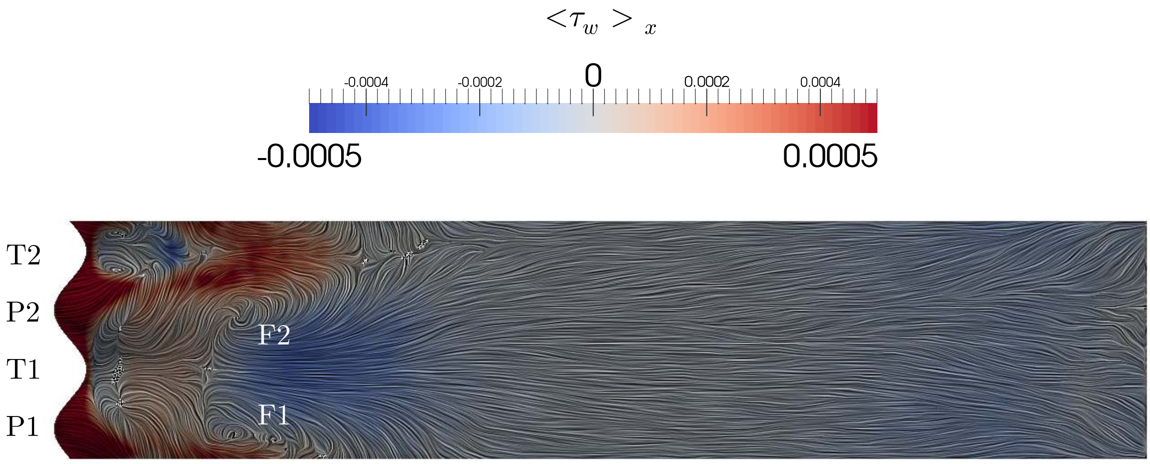

Figure 5.18: Linear Integral Convolution of $<\tau_w>$ Coloured by $<\tau_w>_x$ for undulated case

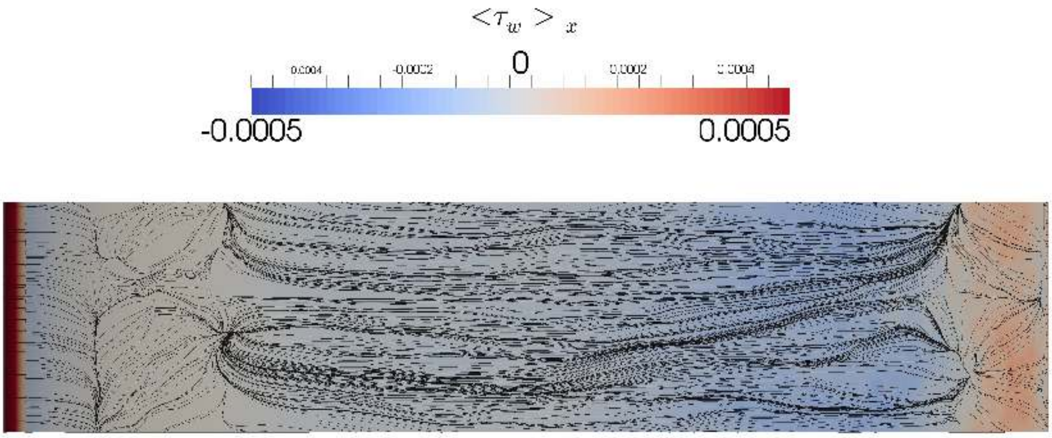

Figure 5.19: WSS lines at surface Coloured by $<\tau_w>_x$ for straight leading edge case

An explanation can be found for the reason why the flow only reattaches in the second trough but not the first by observation of Figure 5.20. In this figure it is seen how most of the turbulent kinetic energy at Trough 1 is located away from the wall. In contrast, at Trough 2, there is a small portion of the chord that is in contact with the turbulent flow that is originated at the rear end of the LSB. This induces a higher momentum in that region which ultimately helps the flow to redevelop a turbulent boundary layer for a short portion of the chord. Despite this, as afore mentioned, the adverse pressure gradient at this high AoA is too severe and the flow ends up separating. In Figure 5.20 one can also identify the larger pressure fluctuations at the reattachment regions, particularly at the rear corners of the LSB. It is seen that on the straight leading edge case the pressure fluctuations only happen at the trailing edge rather than in the leading edge area. Regards the turbulent kinetic energy, the straight leading edge case is much similar to the T1 section rather than T2.

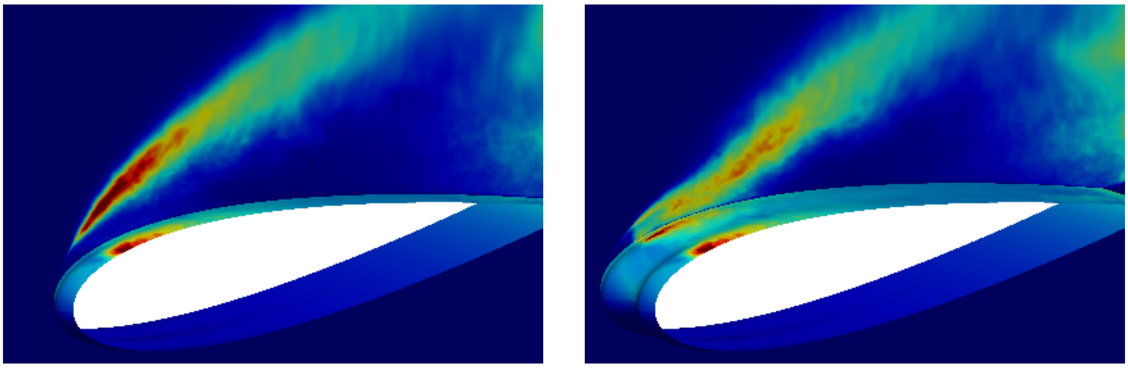

(a) Trough 1 (b) Trough 2

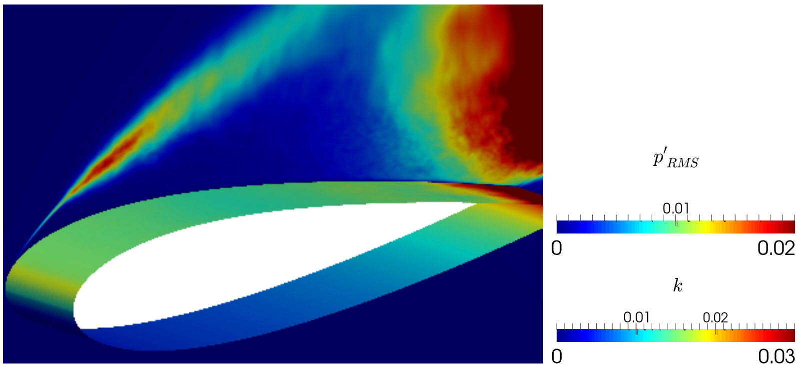

(c) Straight

Figure 5.20: Turbulent Kinetic Energy contours plotted on spanwise planes at Trough 1 and Trough 2 sections and straight case with contours of the pressure fluctuations RMS plotted at the suction surface.

The vortical structures can be identified by “a connected fluid region with a positive second invariant of ∇u” [15], i.e. $Q > 0$ where Q is the second invariant of the velocity gradient tensor. Figure 5.21 shows a snapshot of the flow using this technique for vortex identification. A pair of counter rotating vortices can be clearly identified at the rear of the LSB. The flow recirculates from the bubble’s walls towards its interior hence forming the vortex pair. These pair of counter rotating vortices may well be those mentioned in previous literature [7, 11, 18, 41, 44, 49, 54, 57]. It is worth noticing that the areas where both streamwise and spanwise vortical structures are closer to the wall correspond to the areas where the pressure fluctuations are stronger, which suggest that the two pair of counter-rotating vortices induce the highest fluctuations over the surface.

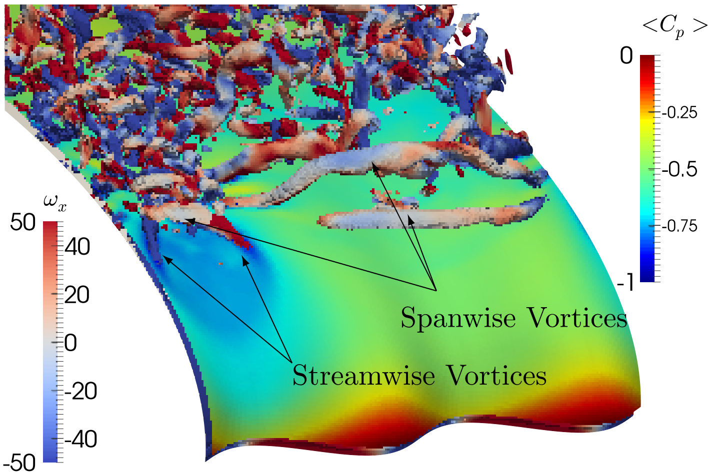

Figure 5.21: Iso-Contours of $Q = 2000$ coloured by streamwise vorticity with contours of averaged Pressure Coefficient plotted over an Iso-Surface of $\eta = 30$

Another feature that is identified is the periodic shedding of spanwise vortical structures from both shear layers formed by the separation region and the LSB region. This structures are much alike to the ones developed in the straight leading edge case as seen in Figure 5.22. The shedding from LSB was already seen in some two-dimensional simulations earlier published [40], and its relation with the oscillations of the force coefficients is studied in the following subsection.

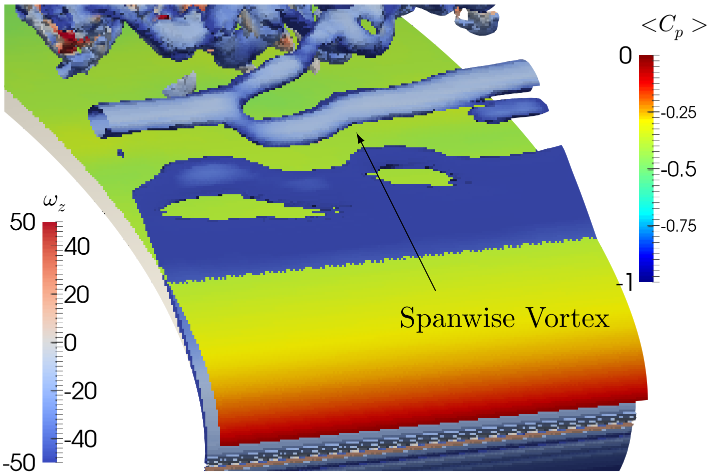

Figure 5.22: Iso-Contours of $Q = 100$ coloured by streamwise vorticity with contours of averaged Pressure Coefficient plotted over an Iso-Surface of $\eta = 30$

5.3.2 Force Coefficient Comparison per Leading Edge Wavelength

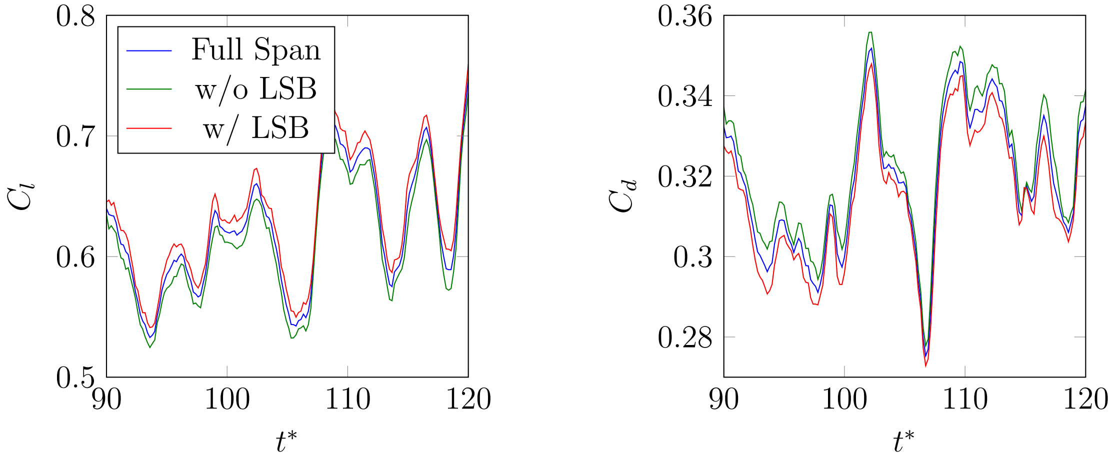

(a) Lift Coefficient (b) Drag Coefficient

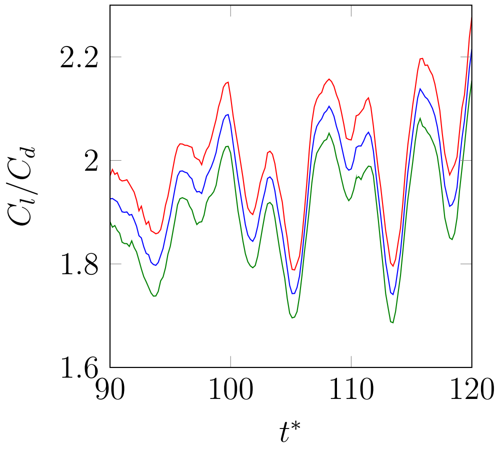

(c) Aerodynamic Efficiency

Figure 5.23: Time History of force coefficients and efficiency from each half of the aerofoil surface, one with LSB and the other without LSB

Table 5.3: Mean Lift and Drag for each half for the period of time showed in Figure 5.23 compared to the full span.

Side	$< C_l >$	$\frac{C_{lside} - C_{lfull}}{C_{lfull}}$	$< C_d >$	$\frac{C_{dside} - C_{dfull}}{C_{dfull}}$	$E =< C_l/C_d >$	$\frac{E_{side} - E_{full}}{E_{full}}$
Full Span	0.622	-	0.319	-	1.952	-
w/o LSB	0.612	-1.6%	0.322	$+0.9\%$	1.897	-2.8%
w/ LSB	0.633	$+1.8\%$	0.315	-1.3%	2.009	$+2.9\%$

Because there was a clear difference between the flow on each side of the aerofoil, it was decided that it would be interesting to investigate how would the aerofoil perform if there was a periodic pattern on the leading edge area, i.e. if all troughs had a LSB, or on the contrary, none had LSB.

In Figure 5.23 one can observe that the side that contains the LSB has always more lift and less drag than the other side. Consequently there is an increase of aerodynamic efficiency when the bubble is present. It seems also that both halves follow the same trends of the full span. This suggests that the aerofoil as a whole is not greatly influenced by the modifications done in the leading edge despite the WLE does indeed alter the flow on the first quarter of the chord. Table 5.3 shows the comparison of the time average values over the period shown in Figure 5.23. It is worth noticing that, despite the differences being small compared to the full span, the differences are roughly doubled when compared between each side. An aerofoil section with all the troughs having a LSB, is hence much more desirable since it could potentially increase its efficiency by 6% compared to some other aerofoil with no bubbles at all.

5.3.3 Unsteady Analysis

So far the focus has been put on average quantities, in this subsection however, the unsteady quantities are the main interest. As aforementioned, the force coefficients measured revealed the presence of some unsteady phenomena (see Figure 5.12). Most likely ,for aerofoils at high AoA, the unsteadiness of the flow is given by the periodic shedding of a pair of counter-rotating spanwise vortices. Figure **??** shows the contours of spanwise vorticity component, where the shedding of these vortex pair is easily identified. Periodic shedding of spanwise vortical structures was also observed on both the separated region and the LSB regions (see Figure 5.16a and 5.21). Additionally, it is worth recalling that in Figure 5.21 a pair of counter-rotating streamwise vortices was identified too at the rear end of the laminar separation bubble.

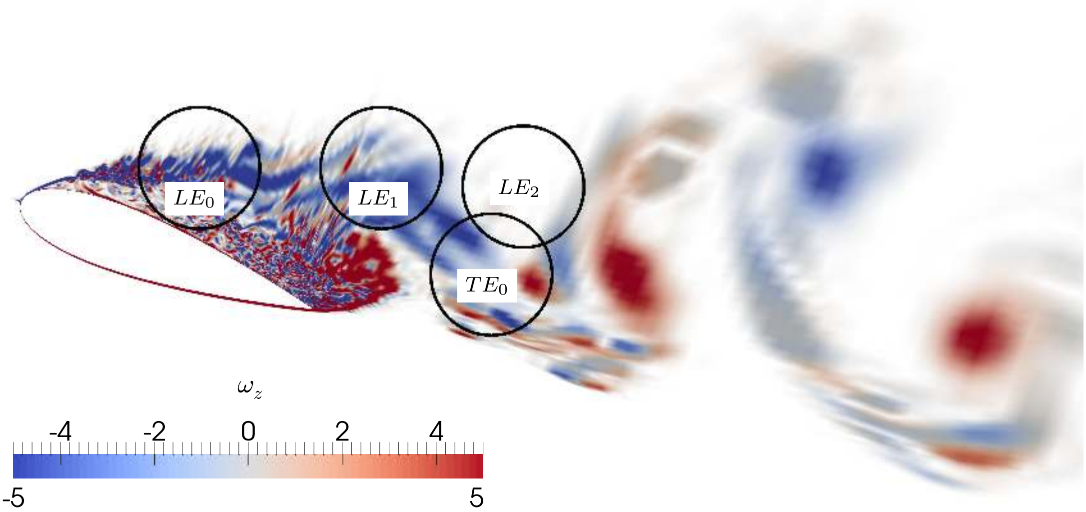

Figure 5.24: Spanwise vorticity for the Straight case at the symmetry plane. Figure also shows the cylinders used to measure the circulation signal at different locations in the wake

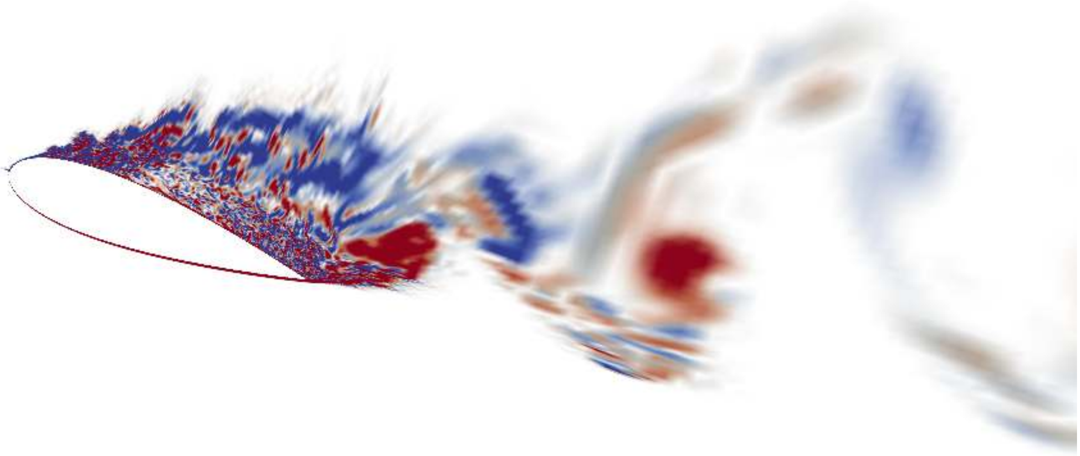

(a) Peak 1

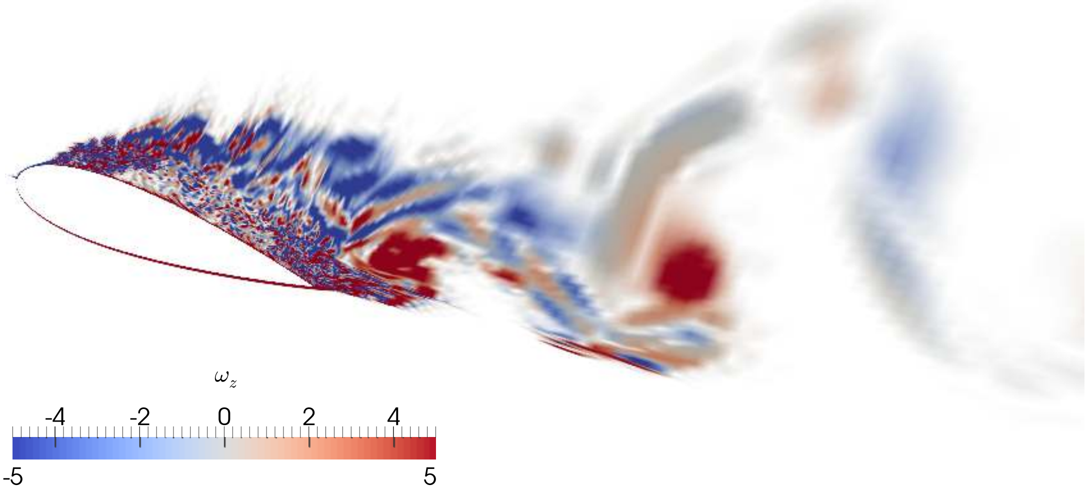

(b) Peak 2

Figure 5.25: Spanwise vorticity for the WLE case at the Peak sections

(a) Trough 1

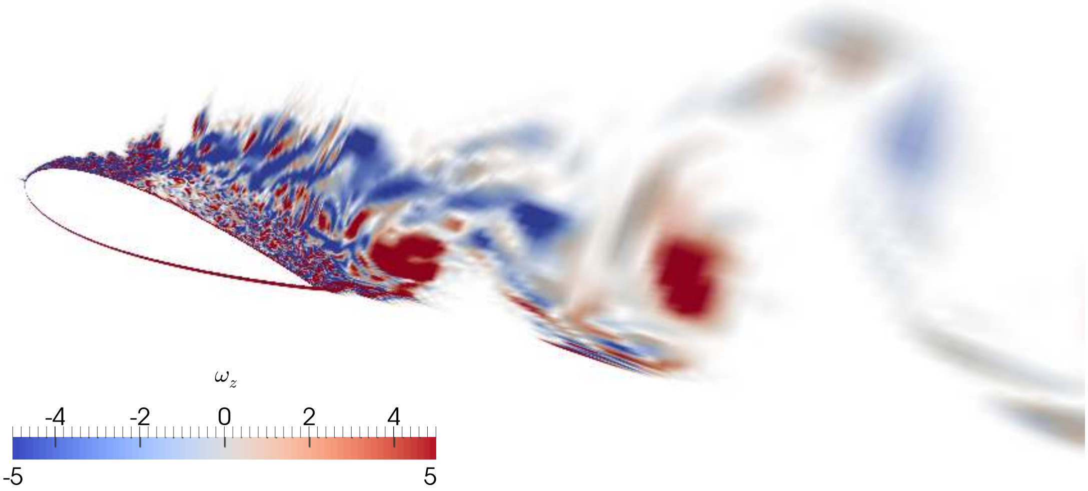

(b) Trough 2

Figure 5.26: Spanwise vorticity for the WLE case at the Trough sections

Analysing in detail Figures 5.24, 5.25, and 5.26, it can be seen that the biggest vortical structures are located close to the trailing edge of the aerofoil. Within the leading edge shear layer, where Figure 5.20 shows turbulence is more energetic, there is a fine grain mixture of both positive and negative spanwise vorticity features. As the flow travels downstream the positive vorticity features die off, and a big clockwise recirculation zone remains. Its counter part, i.e. counter-clockwise circulation, is located beneath it, closer to the trailing edge, but it seems to be much more concentrated. For the straight leading edge case the origin of the big vortical structures lays on top of the trailing edge area. This explains the high pressure oscillations seen in Figure 5.20c in the same area. In the WLE, for all section, because of the slender wake shape, the big spanwise vortices are located a little downstream the trailing edge. Furthermore, for the WLE case, regardless of the span section, the mentioned fine grain scales region is larger than in the straight case. In order to investigate what the relation was between the shedding of this structures and the oscillations observed in the force coefficients, the average circulation per plane in span (see Equation 5.2) was computed inside the areas shown in Figure 5.24. The three cylinders on top, i.e. LE_0, LE_1 and, LE_2, were aimed to investigate how the flow evolved from the leading edge area to the trailing edge area. Just one cylinder located at the close wake influenced by trailing edge was used.

$$\begin{aligned} \Gamma^* &= \frac{1}{N_\zeta}\sum_{0}^{N_\zeta}\Gamma(\zeta) \\ \text{where} \qquad \Gamma &= \int_S \omega_z(\zeta)\,dS \\ \text{and} \qquad N_\zeta &= \text{Number of planes in Span} \end{aligned} \tag{5.2}$$

The power spectral density (PSD) of the signals measured for the straight leading edge case and the undulated case in the cylinders sketched in Figure **??** are plotted in Figure 5.27 in combination with the PSD of the C_l signal. On the *x-axis* the frequency has been non-dimensionalised by the mean chord length L_c and the speed of sound a. There exist a frequency peak in the C_l signal for both straight and undulated cases at $f^* \approx 0.25$. If the frequency is divided by the Mach number and multiplied by the projection of the chord on the normal direction of the flow the Strouhal number is obtained, i.e. $St = L_c \sin(\alpha) f^*/M$. This gives a Strouhal number $St \approx 0.21$, typical of bluff body vortex shedding. It is clearly seen that for the undulated case, the circulation signal at the trailing edge $\Gamma^*_{TE_0}$ matches the peak frequency. On the other hand, the circulation signals measured on the upper side of the wake the frequency peak is not present for the measurements taken closer to the leading edge area, $\Gamma^*_{LE_0}$ and $\Gamma^*_{LE_1}$. Only the most downstream measurement, $\Gamma^*_{LE_2}$, peaks up the C_l frequency peak.

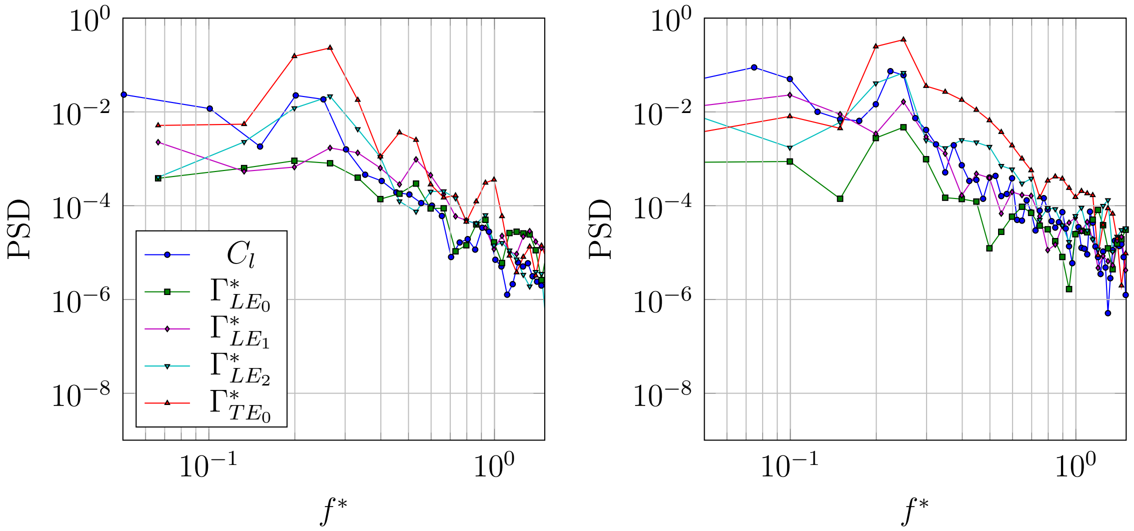

(a) WLE

(b) Straight

Figure 5.27: Power Spectral Density of C_l and circulation signals

In contrast, for the straight leading edge case the C_l frequency peak can clearly be identified in all signals. This is an indication that the wavy case manages to uncover the shedding frequency in the proximity of the leading edge for a while, nonetheless short after, when the flow homogeneity in the span is recovered, the shedding frequency finally stands up. It is also worth mentioning that the power contained in the shedding frequency seems to be lesser in the WLE case, suggesting that the strength of the vortices shed is also lesser.

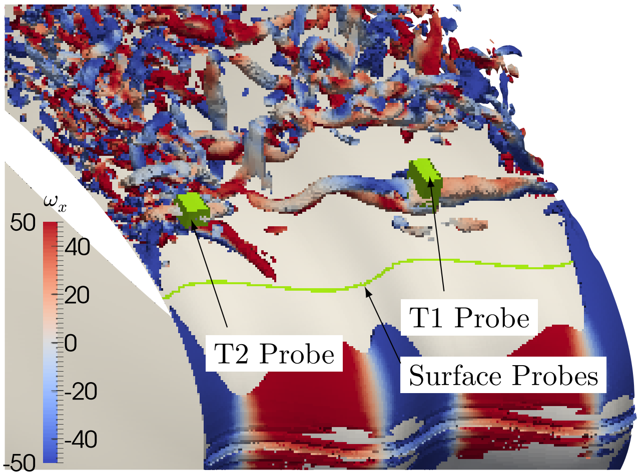

Figure 5.28: Probe locations for pressure signals

Although it seems that it is the low frequency shedding of big vortices in the trailing edge area that dominate the aerodynamic performance of the whole aerofoil, in order to investigate the flow in the leading edge area the probes shown in Figure 5.28 where used to measure pressure signals in this area over time. A line of probes was located in the surface of the aerofoil, and two cubes were located across the shear layers of both the LSB and the separated region. On the cubes the signal is given by the average pressure in the cube.

Figure 5.29 shows the PSD of the signals measured in T1 and T2 probes. It is seen that for the T1 signal the most prominent frequency peak happens at a frequency of $f^* \approx 4$ and its second harmonic at $f^* \approx 8$. For the T2 signal, the frequency peaks show up at $f^* \approx 8$ and $f^* \approx 12$. Additionally, for signal T2, there seems to be a signature of a lower frequency, at $f^* \approx 0.3$, closer to the shedding frequency. The reason why there is not a frequency peak at $f^* = 4$ in the signal taken in T2 might be attributable to the fact that it is in much more proximity of other turbulent structures that are developed immediately downstream of it. In addition, the two pair of counter rotating streamwise vortices are also in close proximity to it. This could in a manner mask the first peak of the frequency, that eventually shows up in it higher harmonics.

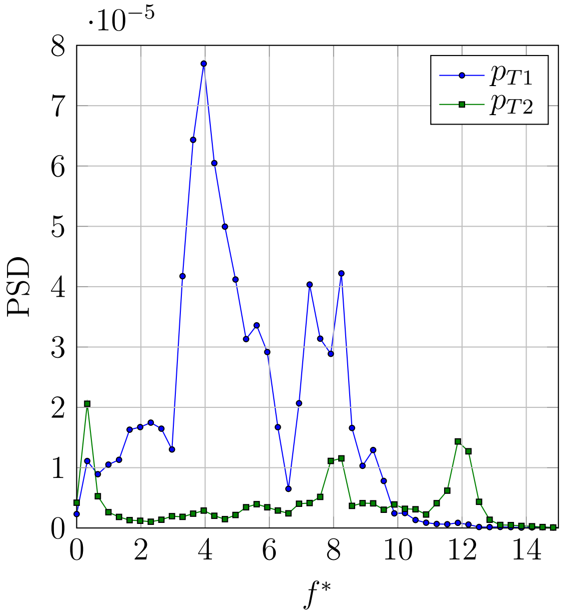

Figure 5.29: Power Spectral Density for pressure signals T1 and T2

The Magnitude Squared Coherence (MSC) between two signals as defined in Equation 5.3, where $G_{s_i s_j}$ is the cross spectral density between signals s_i and s_j, and $G_{s_i s_i}$ is the auto spectral density of signal s_i, is usually used to investigate the relation between two different signals. The MSC takes values between 0 and 1, where a value of $MSC = 1$ indicates a strong relationship between the signals, and a value of $MSC = 0$ indicates the contrary. It can be understood as the analogy of the correlation coefficient in the frequency space. Figure 5.30 shows the coherence between the signals taken at the surface across the span with respect to signal T2 (Figure 5.30b) and signal T1 (Figure 5.30a). When T2 is taken as a base for the coherence computation, the MSC seems to be higher at the first two frequency peaks ($f^* \approx 0.3$ and $f^* \approx 8$). In addition to this two frequencies, when T1 is taken as a base for the computation, a frequency of $f^* \approx 4$ corresponding to the most prominent peak of the T1 signal, shows up. It is worth noting that there is a discontinuity in span for the magnitude of the coherence.

$$MSC_{s_i s_j} = \frac{|G_{s_i s_j}|^2}{G_{s_i s_i} G_{s_j s_j}} \tag{5.3}$$

The discontinuity is more clearly seen in Figure 5.31 where the MSC has been computed taking different spanwise locations in the surface probe of Figure 5.28 as base signals. It is seen that frequency $f^* = 4$ is present in the middle sections and the trough sections but not on the peak sections. It is also seen that the widths of high coherence are greatest at the peak, middle sections, and the first trough (T1) sections, whilst at the second trough (T2) it is much thinner. This indicates that the flow on the trough with a LSB, i.e. T2, leads to a smaller span length scales in this section. Additionally, the discontinuity in the span direction proves that because of the sinusoidal shape of the WLE, the impact of the key flow frequencies is no homogeneous across the span.

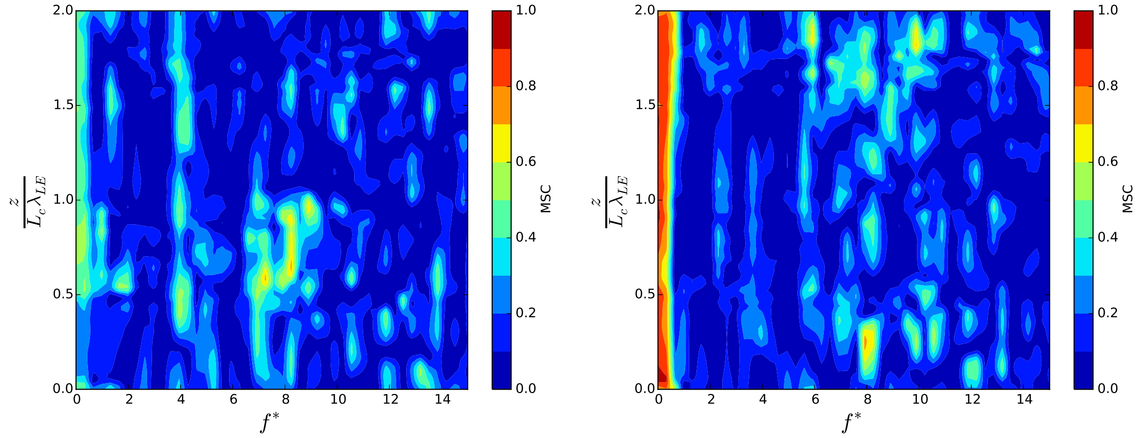

(a) T1

(b) T2

Figure 5.30: Magnitude Squared Coherence for T1 and T2 signals Compared to Surface Signal along the span

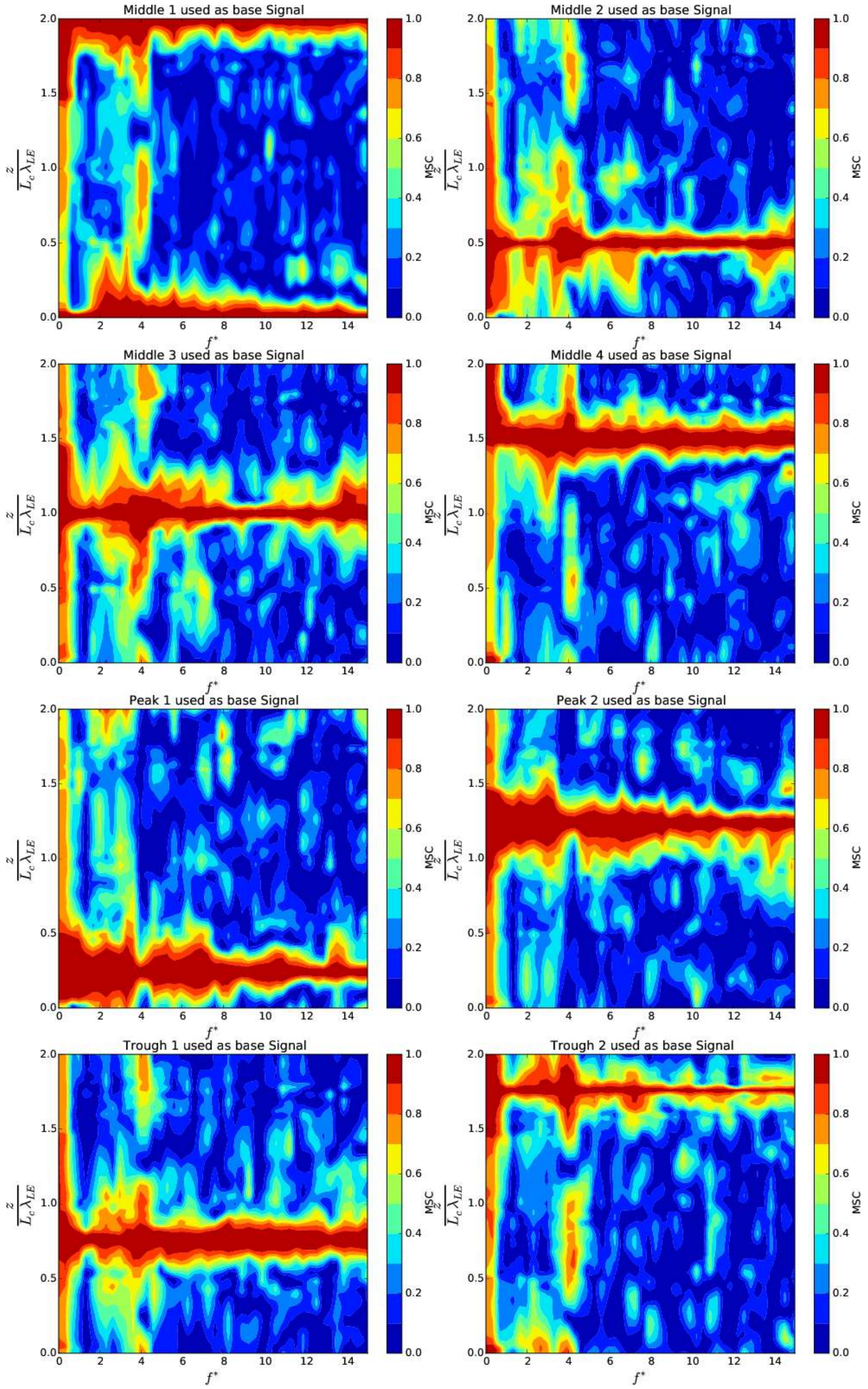
Middle 1 used as base Signal

Middle 2 used as base Signal

Middle 3 used as base Signal

Middle 4 used as base Signal

Peak 1 used as base Signal

Peak 2 used as base Signal

Trough 1 used as base Signal

Trough 2 used as base Signal

Figure 5.31: Magnitude Squared Coherence for each Medium, Peak, and Trough sections compared with the rest of the span

5.4 Discussion

In the previous sections it was found out that if a WLE geometry is exposed to a flow at a high angle of attack, the resulting flow field turns out to be periodic every two WLE wavelengths for the particular WLE parameters used. If the angle of attack is reduced the expected periodicity is recovered. When the flow is periodic in every wavelengh, at $Re = 1.2 \times 10^5$ a set of individual Laminar Separation Bubbles (LSB) is formed inside each trough. As opposed to what happens in a straight leading edge configuration where the LSB is present across the whole span, for the undulated configuration the LSBs are isolated and contained in each trough. At some point in the streamwise direction the pressure gradient causes “a highly unstable detached shear layer forms and transition to turbulence takes place in the detached shear layer. The enhanced momentum transport in the turbulent flow enables reattachment and a newly turbulent boundary layer develops downstream” [45]. When this transition happens, it triggers transition to turbulence in the rest of the span sections, and the flow becomes mostly homogeneous along the entire span (see Figure 5.7).

At high angles of attack, as aforementioned, the periodicity every wavelength is broken, and only one out of every two troughs is able to retain a LSB in it. As the AoA increases the LSB grows in size at the expense of becoming more unstable. At some point the LSBs from each trough would grow big enough to completely climb over its adjoin peak sections. As a consequence the laminar shear layers of each bubble intersect. Now, at this point, i.e. at this AoA, only two scenarios are possible: either both regions undergo laminar separation as in Trough 1 in Figure 5.18 and hence have the entire span separated similarly to the straight case, or, as it actually happened in the results presented in this section, just one of the troughs separates whilst the other retains a smaller LSB in the leading edge area. The question is hence, why one trough survives? One possible explanation could be that the upstream flow that encounters the separation region at the very leading edge turns either left or right in order to avoid entering in a higher pressure zone. This flow escaping from the separation zone ends up entering the next trough section increasing the momentum of the flow and finally avoiding the laminar separation. Hoever, for this to happen, it is needed that the size and shape of the bubbles to be slightly different in order to encourage the flow asymmetry.

This asymmetry in the flow causes the pressure distribution, and the circulation of each region to be slightly different, which in the end means that the aerodynamic performance of each region ends up being different. As it could be expected, the region with the LSB turns out to perform better than the other as seen in Subsection 5.3.2, with almost a 6% difference in the aerodynamic efficiency. Having these bubbles in the troughs is then a desirable feature to promote.

It seems that the presence of the LSB in the trough plays a crucial role in the flow over a undulated wing at $Re = 1.2 \times 10^5$. The question that follows this statement is: What would happen at a higher Re where the LSBs are less likely to appear? Would the mechanism that triggers separation only in one trough remain the same?

In any case, it is clear that the WLE break the homogeneity of the flow in the span direction. This heterogeneity in span is less prone to develop big vortical structures like the ones that appear in aerofoils at high AoA, i.e. vortex shedding. In fact, as shown in Subsection 5.3.3 the WLE geometry develops weaker trailing edge vortices in comparison to the straight leading edge case. Despite this, the vortex shedding was not completely removed by using a WLE aerofoil, and a similar Strouhal number of $St \approx 0.2$ was obtained in both WLE and straight cases. Nonetheless, in the close wake, in the leading edge area, where the influence of the modified geometry is stronger, the peak in spectra is not such a peak. Unfortunately, the strength of the shedding at $\alpha = 20°$ is too strong and the big vortices finally develop in the trailing edge zone. It is speculated that a combined modification of both leading and trailing edge could be much effective in removing the unsteadiness of the flow for aerofoils at high angles of attack.

Noneheless, although the WLE results show a weaker vortex in the uper side of the wake, this same vortex seems to be also weaker than the one on the trailing edge in the straight leading edge case. This could be because only arround 40 points were used in that region of the wake compared to the much denser grid in the trailing edge area. Hence a resolution study needs also to be done in order to confirm the results shown in the previous sections.

Chapter 6

Conclusions and Further Work

6.1 Recapitulation

To conclude, a brief recapitulation of what is included in this report is given here. In first term, the motivations driving this project were outlined, which can be summarised into:

1. To produce high quality simulations that allow to understand the mechanisms of wavy leading edges and the influence of its main parameters (Figure 3.9) in combination with the tandem parameters (Figure 3.10).
2. To develop a dual wing configuration that could be more beneficial than the ones used nowadays. The idea is to implement the sinusoidal leading edges in the second element of a tandem configuration to minimise the effect that both disturbances, from free-stream flow, and from the upstream element, have on the aft element.

From this motives the following objectives were fixed:

1. To investigate the effect of upstream trailing vortices on a tandem configuration with WLEs on the second element.
2. To explain where the aerodynamic benefits of WLEs come from and shed some light on the controversy between the "vortex generator effect" and the "delta wing effect".
3. To investigate different combinations of WLEs parameters for different aerofoils' relative positions.
4. To be able to adapt a prior High-Order accuracy single element "in-house" CFD Fortran code to a tandem aerofoil arrangement.

By accomplishing objective 4 solutions of high quality will be obtained which then followed by objectives 1, 2, and 3 will address the second part of the motive 1. The aerofoil shape chosen to investigate the tandem aerofoil with WLEs in the aft element is a NACA0021 aerofoil because of it is the aerofoil shape used by prior researches when dealing with WLEs.

Up to here the writer has reviewed the publications which relate the most to the topic in question. Papers regarding sinusoidal leading edges were reviewed in Section 2.1 which will inspire further studies during the course of this project. Same could be said about tandem aerofoils configurations, reviewed in Section 2.2. And finally, in terms of literature review, because the Optimised High Order Compact Finite Difference schemes are the numerical base of the "in-house" code used to solve the flow equations, a walk through its development from its first steps to the actual version used in this project was done in Section 2.3.

Following from there, Chapter 3 focuses on the numerical and modelling techniques used to obtain the final results. Chapter 4 includes all the test carried out up to date. These test include both inviscid and viscous tests for a NACA0012 benchmark case. Both cases served as validation as well as training for the student, who became much familiar with the tools used to investigate how the WLE geometry alters the flow around it.

In Chapter 5 the WLE problem was tackled. Initially an approach was used where turbulent motions where introduced at the initialisation stage in order to trigger turbulent boundary layers on the aerofoil. However the results obtained where quite surprising. Previous researchers [49] found that the NACA021 with WLE parameters $\lambda_{LE} = 0.11L_c$ and $h_{LE} = 0.03L_c$ resulted in a much higher increase in the aerofoil performance. This was because due to the undulations in the leading edge the peak sections delayed separation due to the presence of streamwise vortices originated at the trough sections that enhanced the momentum transfer and ultimately delayed separation. This results also showed a periodicity of the flow in per each WLE wavelength. In this study however, it was found that the flow was not periodic in every wavelength, but only every two wavelengths. Nonetheless the agreement with experimental data was much higher than previous publications. It was suspected that this non-periodicity could have been promoted by the flow initialisation, hence, it was decided to change the initialisation strategy and a clean laminar inflow condition was used instead. The results did however remained the same despite changing the flow initialisation method. In the next section the conclusions obtained are detailed.

6.2 Conclusions

In Chapter 5 it has been shown that while at low angles of attack the flow is periodic in every WLE wavelength, with a LSB contained in every trough, at higher angles of attack the symmetry of the flow is lost and only one out of every two troughs is capable of retaining a LSB whereas the other trough undergoes laminar separation. It is speculated that such behaviour is governed by the shape, size and growth of the LSBs inside trough sections, however, more tests need to be performed in order to confirm such belief.

This asymmetry just mentioned discourages the appearance of big span structures such as does developed on aerofoils that suffer from vortex shedding. Unfortunately if the AoA is too high, the strength of the shedding mechanism is too strong, and the heterogeneity of the flow in span promoted by the undulations in the leading edge is not enough, at least with the parameters used in this study, and shedding cannot be avoided.

Nevertheless the strength of the shedding is at the very least weakened. Additionally, the troughs that retain the LSB offer a better aerodynamic performance than the ones that do not retain it. An increase of nearly 6% in the lift to drag ratio can be achieved.

Results also suggest that the flow over a WLE wing is highly dependent on the upstream conditions since:

1. Small disturbances can promote small asymmetries that get amplified at high angles of attack leading to different flow structures at different trough sections
2. The LSB seems to play an eminent role in the flow structure. Imposing a higher turbulence intensity upstream the aerofoil section can suppress such bubble which will consequently lead to a different flow picture than the one shown in this report so far.

6.3 Further Work

The following paragraphs describe what the student considers that needs to be done by the end of this project.

1. In first place, the results obtained need to be further investigated in order to prove that the flow patterns observed are the true nature of the flow or are on the contrary an artifact of the numerical methods used. Simulations using 3 and 4 wavelengths will shed some light in this matter since the flow periodicity in span will be forced at 3 and 4 wavelengths respectively.
2. All simulation were run using a free stream Mach number of $M_\infty = 0.4$. As it is shown in Appendix A this induce a maximum local Mach number of $M \approx 0.6$, which is, although not too high, could be causing the results to disagree with the experimental data since this was performed in incompressible flow conditions. An study of different free stream Mach numbers seems a good idea in order to increase the reliability of the simulations.
3. It is possible that the simulations lack of resolution in the near-middle wake area, where the trailing edge vortices are developed, with just around 40 points used in the upper area of this part of the wake. Hence a grid resolution study needs to be performed in order to improve the reliability of the results obtained.
4. It is necessary to obtain results for different angles of attack in order to further understand the mechanisms induced by the WLE geometry. In particular it is thought that a simulation of an aerofoil increasing its AoA in time would particularly be very useful to investigate the mechanism that triggers separation just in one trough but not the other.
5. The presence of Laminar Separation Bubbles in the troughs turned out to be a crucial feature. It would be of high interest to investigate a case where these bubbles are not present at all. This could be achieved by continuously impinging a stream of turbulent flow on the leading edge area. Two options arise here to achieve this: 1)

A tandem configuration such as that described in Figure 2.1 would create genuine turbulent wake from the fore element that would impinge on the leading edge of the aft element. 2) The SIT method used in Section 4.3.2 could be used continuously during the whole simulation time instead of just used for the flow initialisation. The former option is the one that was originally contemplated, as it can be deduced from the title of this report. However the simulations performed so far turned out to be more computationally demanding than what originally was thought, and hence the inclusion of a former aerofoil would dramatically increase the cost of the simulations.

Appendix A

Compressibility Effects

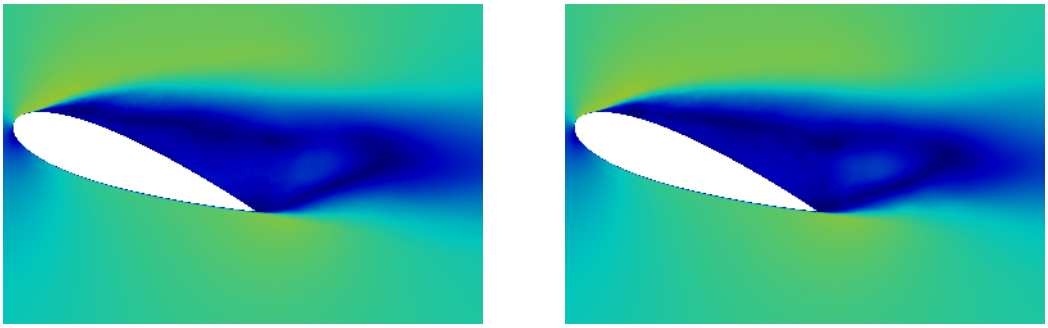

(a) Peak 1

(b) Peak 2

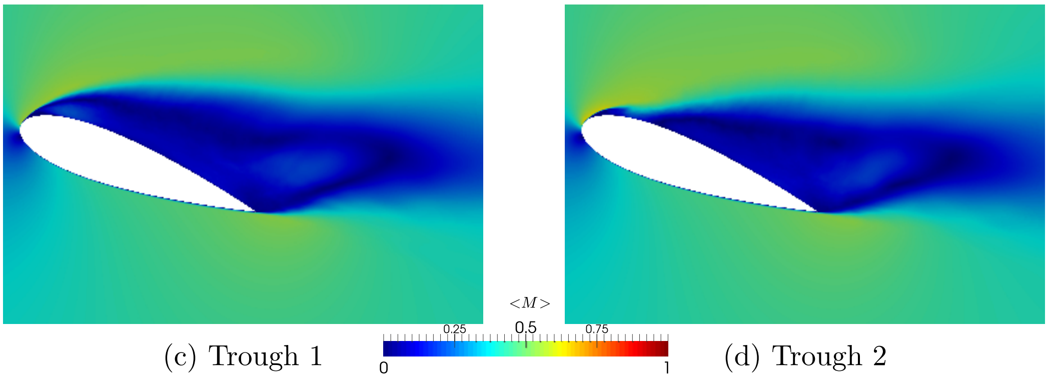

(c) Trough 1

(d) Trough 2

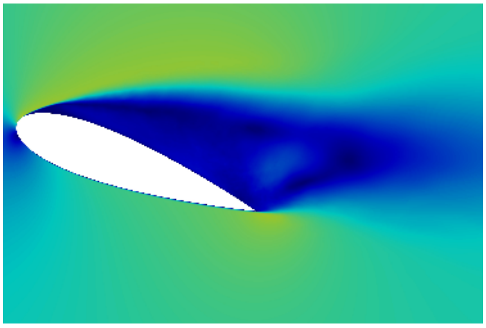

(e) Straight

Figure A.1: Local Mach Number at different span sections for the WLE and at symmetry section for the straight case

Figure A.1 shows that the maximum local Mach number happens at the trough containing the LSB, i.e. Trough 2 in Figure A.1, with a value of $< M >\approx 0.6$. Although the freestream Mach number used was $M_\infty = 0.4$ the values in the leading edge area of the aerofoil sections approach the region where compressibility effects may affect the solution, being this one cause for the mismatch with the experimental data of Hansen [11], that was taken in an incompressible water tunnel.

Simulations will be hence repeated for a lower M_∞ in order to be 100% sure that the solutions obtained so far offer a good comparison with available experimental data. So far $M_\infty = 0.4$ was used because offered a good trade off between simulation time and compressibility effects, i.e. a lower freestream Mach number means that the flow takes more time units to travel from one side of the domain to the other, increasing the convergence time consequently.

Appendix B

Periodic Boundary Conditions Check

In order to check whether the periodic boundary conditions imposed every two WLE wavelengths in the span direction were promoting the appearance of LSB every two wavelengths, a set of tests where performed.

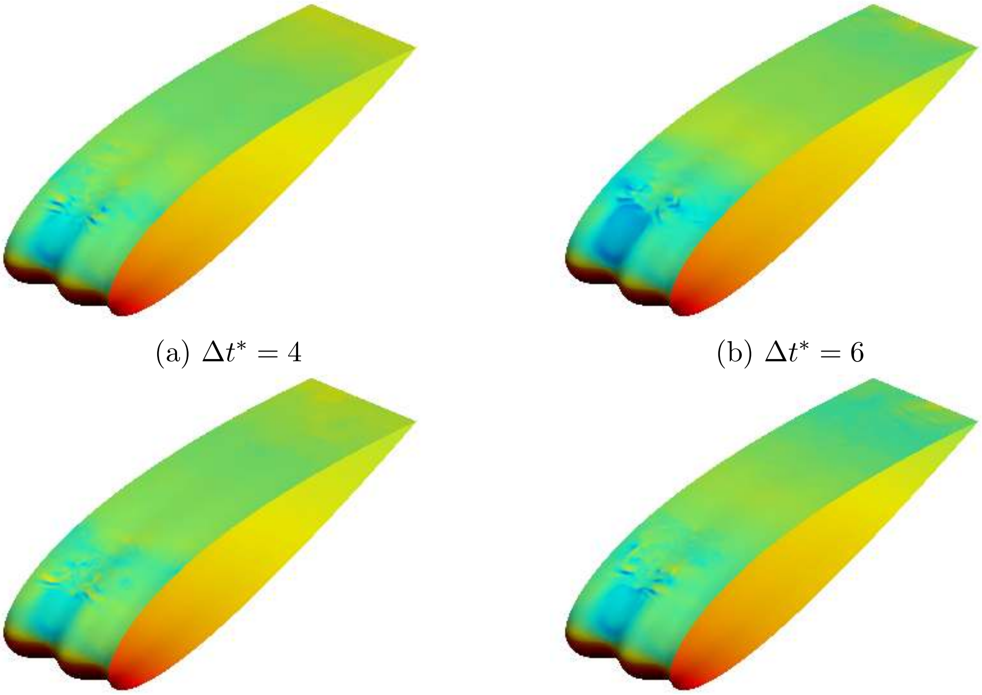

(a) $\Delta t^* = 4$ (b) $\Delta t^* = 6$

(c) $\Delta t^* = 8$ (d) $\Delta t^* = 10$

Figure B.1: Surface pressure coefficient time evolution of $\Phi = \lambda_{LE}/2$ shifted geometry

The first test performed consisted in a shift of the solution in span, i.e. the geometry was shifted with a phase angle $\Phi = \lambda_{LE}/2$ from left to right. This means that peaks turned into troughs and viceversa. Then the solution was mapped into the new geometry and the simulation was run for a period of $10t^*$. Time history of the surface pressure is shown in Figure B.1. It is seen that the LSB was moved to the right but it remained there the whole time, indicating that the LSB is present in just one trough independently of the phase angle Φ.

Additionally two more simulations using a span of $L_b = 3\lambda_{LE}$ and $L_b = \lambda_{LE}$ were aimed. However it is worth noting that each of them supposed an increase of 50% and 100% in the total number of points used, and hence becoming much more expensive computationally speaking. Nonetheless, so far at this point in time a non-fully converged solution for the case of $L_b = 3\lambda_{LE}$ is available and it is shown in Figure B.2. It is seen that even using this span, the LSB does not show in every single trough. Instead as expected, the troughs neighbouring a separated region are the ones containing the bubbles since they are the ones receiving the secondary flow that tries to avoid the separated trough.

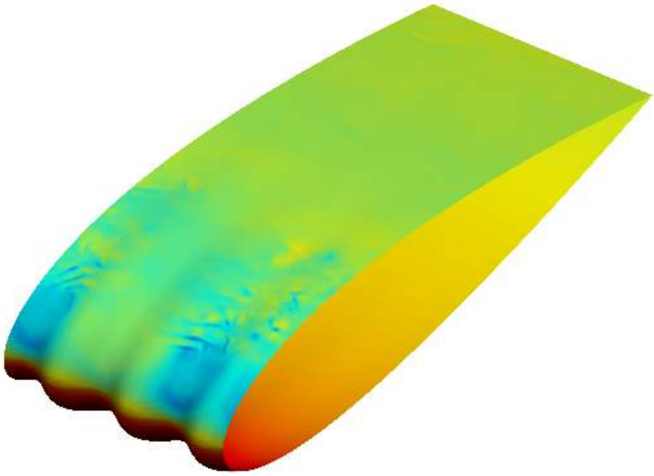

Figure B.2: Surface Pressure Coefficient for $L_b = 3\lambda_{LE}$

Bibliography

[1] AIAA. Guide for the verification and validation of computational fluid dynamics simulations., 1998.

[2] Brian Cabral and Leith Casey Leedom. Imaging vector fields using line integral convolution. *Proc. SIGGRAPH*, pages 263–270, 1993. ISSN 0097-8930. doi: 10.1145/166117.166151. URL http://dx.doi.org/10.1145/166117.166151.

[3] Diogo Matos Chaves. *Implementation of a 2D Panel Method for Potential Flow Past Multi-Element Airfoil Configurations*. Master's thesis, Technical University of Lisbon, 2012.

[4] J. L. E. Guerreiro and J. M. M. Sousa. Low-Reynolds-Number Effects in Passive Stall Control Using Sinusoidal Leading Edges. *AIAA Journal*, 50(2):461–469, February 2012. ISSN 0001-1452. doi: 10.2514/1.J051235. URL http://arc.aiaa.org/doi/abs/10.2514/1.J051235.

[5] FAA. Aeronautical Information Manual: Official Guide to Basic Flight Information and ATC Procedures, 2013.

[6] DW Fanjoy and DJ Dorney. Numerical Simulations of Tandem-Airfoil Aerodynamics. In *Aerospace Atlantic Conference*, Dayton, Ohio, 1996. SAE. URL http://papers.sae.org/961295/.

[7] Julien Favier, Alfredo Pinelli, and Ugo Piomelli. Control of the separated flow around an airfoil using a wavy leading edge inspired by humpback whale flippers. *Comptes Rendus Mécanique*, 340(1-2):107–114, January 2012. ISSN 16310721. doi: 10.1016/j.crme.2011.11.004. URL http://linkinghub.elsevier.com/retrieve/pii/S1631072111001902.

[8] FE Fish and JM Battle. Hydrodynamic design of the humpback whale flipper. *Journal of Morphology*, 1(225):51–60, 1995. URL http://onlinelibrary.wiley.com/doi/10.1002/jmor.1052250105/abstract.

[9] C. A. J. Fletcher. Computational techniques for fluid dynamics 2, 1988.

[10] M. Gaster. The Structure and Behaviour of Laminar Separation Bubbles. *Aeronautical Research Council Reports and Memoranda*, (3595):1–31, 1967.

[11] Kristy L. Hansen, Richard M. Kelso, and Bassam B. Dally. Performance Variations of Leading-Edge Tubercles for Distinct Airfoil Profiles. *AIAA Journal*, 49(1):185–194, January 2011. ISSN 0001-1452. doi: 10.2514/1.J050631. URL `http://arc.aiaa.org/doi/abs/10.2514/1.J050631`.

[12] J.L. Hess and a.M.O. Smith. Calculation of potential flow about arbitrary bodies. *Progress in Aerospace Sciences*, 8:1–138, January 1967. ISSN 03760421. doi: 10.1016/0376-0421(67)90003-6. URL `http://linkinghub.elsevier.com/retrieve/pii/0376042167900036`.

[13] Charles Hirsch. *Numerical Computation of Internal and External Flows, Vol. 2*. John Wiley & Sons Ltd., Chichester, 1990. ISBN 047 923516.

[14] Richard S. Hirsh. Higher Order Accurate Difference Solutions of Fluid Mechanic Problems by a Compact Differencing Technique. *Journal of Computational Physics*, 19:90–109, 1975.

[15] J.C.R Hunt, a.a. Wray, and P. Moin. Eddie, Strams, and Convergence Zones in Turbulent Flows. *Proc. of the Summer Program (CTR)*, (1970), 1988.

[16] Eastman N Jacobs. The aerodynamic characteristics of eight very thick airfoils from tests in the variable density wind tunnel, 1932. URL `http://hdl.handle.net/2060/19930091465`.

[17] Mohsen Jahanmiri. Laminar Separation Bubble : Its Structure , Dynamics and Control. *Chalmers University of Technology Research Report*, pages 1–24, 2011.

[18] Hamid Johari, Charles W. Henoch, Derrick Custodio, and Alexandra Levshin. Effects of Leading-Edge Protuberances on Airfoil Performance. *AIAA Journal*, 45(11):2634–2642, November 2007. ISSN 0001-1452. doi: 10.2514/1.28497. URL `http://arc.aiaa.org/doi/abs/10.2514/1.28497`.

[19] L. E. Jones, R. D. Sandberg, and N. D. Sandham. Direct numerical simulations of forced and unforced separation bubbles on an airfoil at incidence. *Journal of Fluid Mechanics*, 602:175–207, April 2008. ISSN 0022-1120. doi: 10.1017/S0022112008000864. URL `http://www.journals.cambridge.org/abstract_S0022112008000864`.

[20] FA Khan and TJ Mueller. Tip vortex/airfoil interaction for a low Reynolds number canard/wingconfiguration. *Journal of Aircraft*, 28(3):181–186, 1991. URL `http://arc.aiaa.org/doi/pdf/10.2514/3.46010`.

[21] Jae Wook Kim. Optimised boundary compact finite difference schemes for computational aeroacoustics. *Journal of Computational Physics*, 225(1):995–1019, July 2007. ISSN 00219991. doi: 10.1016/j.jcp.2007.01.008. URL `http://linkinghub.elsevier.com/retrieve/pii/S0021999107000149`.

[22] Jae Wook Kim. High-order compact filters with variable cut-off wavenumber and stable boundary treatment. *Computers & Fluids*, 39(7):1168–1182, August 2010. ISSN 00457930. doi: 10.1016/j.compfluid.2010.02.007. URL `http://linkinghub.elsevier.com/retrieve/pii/S0045793010000502`.

[23] Jae Wook Kim. Quasi-disjoint pentadiagonal matrix systems for the parallelization of compact finite-difference schemes and filters. *Journal of Computational Physics*, 241:168–194, May 2013. ISSN 00219991. doi: 10.1016/j.jcp.2013.01.046. URL `http://linkinghub.elsevier.com/retrieve/pii/S0021999113000995`.

[24] Jae Wook Kim and Sina Haeri. An advanced synthetic eddy method for the computation of aerofoilturbulence interaction noise. *Journal of Computational Physics*, 287:1–17, 2015. ISSN 00219991. doi: 10.1016/j.jcp.2015.01.039. URL `http://linkinghub.elsevier.com/retrieve/pii/S0021999115000534`.

[25] Jae Wook Kim and D Joo. Generalized characteristic boundary conditions for computational aeroacoustics, part 2. *AIAA journal*, 42(1), 2004. URL `http://arc.aiaa.org/doi/pdf/10.2514/1.9029`.

[26] Jae Wook Kim and DJ Lee. Implementation of boundary conditions for optimized high-order compact schemes. *Journal of Computational Acoustics*, 5(2), 1997. URL `http://www.worldscientific.com/doi/abs/10.1142/S0218396X97000113`.

[27] Jae Wook Kim and Duck J. Lee. Optimized compact finite difference schemes with maximum resolution. *AIAA Journal*, 34(5):887–893, May 1996. ISSN 0001-1452. doi: 10.2514/3.13164. URL `http://arc.aiaa.org/doi/abs/10.2514/3.13164`.

[28] Jae Wook Kim and Duck Joo Lee. Generalized Characteristic Boundary Conditions for Computational Aeroacoustics. *AIAA Journal*, 38(11), 2000.

[29] Jae Wook Kim and Duck Joo Lee. Characteristic Interface Conditions for Multiblock High-Order Computation on Singular Structured Grid. *AIAA Journal*, 41(12):2341–2348, December 2003. ISSN 0001-1452. doi: 10.2514/2.6858. URL `http://arc.aiaa.org/doi/abs/10.2514/2.6858`.

[30] Jae Wook Kim and Richard D. Sandberg. Efficient parallel computing with a compact finite difference scheme. *Computers & Fluids*, 58:70–87, April 2012. ISSN 00457930. doi: 10.1016/j.compfluid.2012.01.004. URL `http://linkinghub.elsevier.com/retrieve/pii/S0045793012000138`.

[31] Jae Wook Kim, Alex S. H. Lau, and Neil D. Sandham. Proposed Boundary Conditions for Gust-Airfoil Interaction Noise. *AIAA Journal*, 48(11):2705–2710, November 2010. ISSN 0001-1452. doi: 10.2514/1.J050428. URL `http://arc.aiaa.org/doi/abs/10.2514/1.J050428`.

[32] Alex S.H. Lau, Sina Haeri, and Jae Wook Kim. The effect of wavy leading edges on aerofoilgust interaction noise. *Journal of Sound and Vibration*, 332(24):6234–6253, November 2013. ISSN 0022460X. doi: 10.1016/j.jsv.2013.06.031. URL `http://linkinghub.elsevier.com/retrieve/pii/S0022460X13005713`.

[33] Sanjiva K. Lele. Compact finite difference schemes with spectral-like resolution. *Journal of Computational Physics*, 103(1):16–42, November 1992. ISSN 00219991. doi: 10.1016/0021-9991(92)90324-R.

[34] D. S. Miklosovic, M. M. Murray, L. E. Howle, and F. E. Fish. Leading-edge tubercles delay stall on humpback whale (Megaptera novaeangliae) flippers. *Physics of Fluids*, 16(5):L39, 2004. ISSN 10706631. doi: 10.1063/1.1688341. URL `http://scitation.aip.org/content/aip/journal/pof2/16/5/10.1063/1.1688341`.

[35] David S. Miklosovic, Mark M. Murray, and Laurens E. Howle. Experimental Evaluation of Sinusoidal Leading Edges. *Journal of Aircraft*, 44(4):1404–1408, July 2007. ISSN 0021-8669. doi: 10.2514/1.30303. URL `http://arc.aiaa.org/doi/abs/10.2514/1.30303`.

[36] William L. Oberkampf and Timothy G. Trucano. Verification and validation in computational fluid dynamics. *Progress in Aerospace Sciences*, 38(3):209–272, April 2002. ISSN 03760421. doi: 10.1016/S0376-0421(02)00005-2. URL `http://linkinghub.elsevier.com/retrieve/pii/S0376042102000052`.

[37] SA Orszag and M Israeli. Numerical simulation of viscous incompressible flows. *Annual Review of Fluid Mechanics*, 1974.

[38] C. a. Ozen and D. Rockwell. Control of vortical structures on a flapping wing via a sinusoidal leading-edge. *Physics of Fluids*, 22(2):021701, 2010. ISSN 10706631. doi: 10.1063/1.3304539. URL `http://scitation.aip.org/content/aip/journal/pof2/22/2/10.1063/1.3304539`.

[39] Total Terminal Passengers. PASSENGERS (000s) - 10 YEAR RECORD CALENDAR YEAR 2003-2012. Technical report, Heathrow Airport, 2012.

[40] Laura L. Pauley, Parviz Moin, and William C. Reynolds. The structure of two-dimensional separation. *Journal of Fluid Mechanics*, 220:397, 1990. ISSN 0022-1120. doi: 10.1017/S0022112090003317.

[41] Hugo T C Pedro and Marcelo H Kobayashi. Numerical Study of stall delay on humpback whale flippers. In *46th AIAA Aerospace Sciences Meeting and Exhibit*, Reno, Nevada, 2008. American Institute of Aeronautics and Astronautics. doi: 10.2514/6.2008-584. URL `http://dx.doi.org/10.2514/6.2008-584`.

[42] T.J Poinsot and S.K Lele. Boundary conditions for direct simulations of compressible viscous flows. *Journal of Computational Physics*, 101(1):104–129, July 1992. ISSN 00219991. doi: 10.1016/0021-9991(92)90046-2. URL `http://www.sciencedirect.com/science/article/pii/0021999192900462`.

[43] MD Rhodes and BP Selberg. Benefits of dual wings over single wings for high-performance business airplanes. *Journal of Aircraft*, 21(2), 1984. URL `http://arc.aiaa.org/doi/pdf/10.2514/3.48234`.

[44] N. Rostamzadeh, K. L. Hansen, R. M. Kelso, and B. B. Dally. The formation mechanism and impact of streamwise vortices on NACA 0021 airfoil's performance with undulating leading edge modification. *Physics of Fluids*, 26(10):107101, October 2014. ISSN 1070-6631. doi: 10.1063/1.4896748. URL `http://scitation.aip.org/content/aip/journal/pof2/26/10/10.1063/1.4896748`.

[45] N. D. Sandham. Transitional separation bubbles and unsteady aspects of aerofoil stall. *Aeronautical Journal*, 112(3258):395–404, 2008. ISSN 00019240.

[46] DF Scharpf and TJ MUELLER. Experimental study of a low Reynolds number tandem airfoil configuration. *Journal of aircraft*, 29(2):1–6, 1992. URL `http://arc.aiaa.org/doi/pdf/10.2514/3.46149`.

[47] T.K. Sengupta, a. Dipankar, and a. Kameswara Rao. A new compact scheme for parallel computing using domain decomposition. *Journal of Computational Physics*, 220(2):654–677, January 2007. ISSN 00219991. doi: 10.1016/j.jcp.2006.05.018. URL `http://linkinghub.elsevier.com/retrieve/pii/S0021999106002543`.

[48] Ravindra A Shirsath and Rinku Mukherjee. Unsteady Aerodynamics of Tandem Airfoils Pitching in Phase. In *2nd International Conference on Mechanical, Production and Automobile Engineering*, pages 203–208, Singapore, 2012.

[49] A. Skillen, A. Revell, A. Pinelli, U. Piomelli, and J. Favier. Flow over a Wing with Leading-Edge Undulations. *AIAA Journal*, pages 1–9, September 2014. ISSN 0001-1452. doi: 10.2514/1.J053142. URL `http://arc.aiaa.org/doi/abs/10.2514/1.J053142`.

[50] AM O. Smith. High-lift aerodynamics. *Journal of Aircraft*, 12(6), 1975. URL `http://arc.aiaa.org/doi/abs/10.2514/3.59830`.

[51] CKW Tam and JC Webb. Dispersion-relation-preserving finite difference schemes for computational acoustics. *Journal of computational physics*, 107, 1993. URL `http://www.sciencedirect.com/science/article/pii/S0021999183711423`.

[52] Kevin W Thompson. Time dependent boundary conditions for hyperbolic systems. *Journal of Computational Physics*, 68(1):1–24, January 1987. ISSN 00219991. doi: 10.1016/0021-9991(87)90041-6. URL `http://linkinghub.elsevier.com/retrieve/pii/0021999187900416`.

[53] KW Thompson. Time-dependent boundary conditions for hyperbolic systems, II. *Journal of Computational Physics*, 439461:439–461, 1990. URL `http://www.sciencedirect.com/science/article/pii/002199919090152Q`.

[54] Paul W. Weber, Laurens E. Howle, Mark M. Murray, and David S. Miklosovic. Computational Evaluation of the Performance of Lifting Surfaces with Leading-Edge Protuberances. *Journal of Aircraft*, 48(2):591–600, March 2011. ISSN 0021-8669. doi: 10.2514/1.C031163. URL `http://arc.aiaa.org/doi/abs/10.2514/1.C031163`.

[55] F A Woodward. NASA Contractor Report 3227: USSAERO Computer Program Versions B and C Development, Versions B and C. Technical Report April, NASA, 1980.

[56] Zhang Xingwei, Zhou Chaoying, Zhang Tao, and Ji Wenying. Numerical study on effect of leading-edge tubercles. *Aircraft Engineering and Aerospace Technology*, 85(4):247–257, 2013. ISSN 0002-2667. doi: 10.1108/AEAT-Feb-2012-0027. URL `http://www.emeraldinsight.com/10.1108/AEAT-Feb-2012-0027`.

[57] H.S. Yoon, P.a. Hung, J.H. Jung, and M.C. Kim. Effect of the wavy leading edge on hydrodynamic characteristics for flow around low aspect ratio wing. *Computers & Fluids*, 49(1):276–289, October 2011. ISSN 00457930. doi: 10.1016/j.compfluid.2011.06.010. URL `http://linkinghub.elsevier.com/retrieve/pii/S0045793011001988`.

[58] G ZHANG and S YANG. Experimental investigation of the aerodynamic characteristics of tandem-airfoil based on low Reynolds number. *Chinese Journal of Computational Mechanics*, 27(4), 2010. URL `http://en.cnki.com.cn/Article_en/CJFDTotal-JSJG201004029.htm`.

[59] M. M. Zhang, G. F. Wang, and J. Z. Xu. Experimental study of flow separation control on a low-Re airfoil using leading-edge protuberance method. *Experiments in Fluids*, 55(4):1710, April 2014. ISSN 0723-4864. doi: 10.1007/s00348-014-1710-z. URL `http://link.springer.com/10.1007/s00348-014-1710-z`.